Volume 137
2010

EDITORS
F. Kremer
W. Richtering

Progress in Colloid and Polymer Science

Trends in Colloid and Interface Science XXIII

VOLUME EDITOR
Seyda Bucak

Springer

Progress in Colloid and Polymer Science
Volume 137

Series Editors
F. Kremer, Leipzig
W. Richtering, Aachen

Progress in Colloid and Polymer Science

Recently published and Forthcoming Volume

Trends in Colloid and Interface Science XXIII
Volume Editor: Seyda Bucak
Vol. 137, 2010

Gels: Structures, Properties, and Functions
Volume Editors: Masayuki Tokita, Katsuyoshi Nishinari
Vol. 136, 2009

Colloids for Nano- and Biotechnology
Volume Editors: Hórvölgyi, Z.D., Kiss, É.
Vol. 135, 2008

Surface and Interfacial Forces From Fnndamentals to Applications
Volume Editors: Auernhammer, G.K., Butt, H.-J , Vollmer, D.
Vol. 134, 2008

Smart Colloidal Materials
Volume Editor: Richtering, W.
Vol. 133, 2006

Characterization of Polymer Surfaces and Thin Films
Volume Editors: Grundke, K., Stanun, M., Adler, H.-J.
Vol. 132, 2006

Analytical Ultracentrifugation VIII
Volume Editors: Wandrey, C., Cölfen, H.
Vol. 131, 2006

Scattering Methods and the Properties ofPolymer Materials
Volume Editors: Stribeck, N., Smarsly, B.
Vol. 130, 2005

Mesophases, Polymers, and Particles
Volume Editors: Lagaly, G., Richtering, W.
Vol. 129, 2004

Surface and Colloid Science
Volume Editor: Galembeck, F.
Vol. 128, 2004

Analytical Ultracentrifugation VII
Volume Editors: Lechner, M.D., Börger, L.
Vol. 127, 2004

Trends in Colloid and Interface Science XVII
Volume Editors: Cabuil, V., Levitz, P., Treiner, C.
Vol. 126, 2004

From Colloids to Nanotechnology
Volume Editors: Zrinyi, M., Horvolgyi, Z.D.
Vol. 125, 2004

Aqueous Polymer Dispersions
Volume Editor: Tauer, K.
Vol. 124, 2004

Trends in Colloid and Interface Science XVI
Volume Editors: Miguel, M., Burrows, H.D.
Vol. 123, 2004

Aqueous Polymer – Cosolute Systems
Volume Editor: Anghel, D.F.
Vol. 122, 2002

Molecular Organisation on Interfaces
Volume Editor: Lagaly, G.
Vol. 121, 2002

Lipid and Polymer–Lipid Systems
Volume Editor: Nylander, T.
Vol. 120, 2002

Seyda Bucak
Editor

Trends in Colloid and Interface Science XXIII

Springer

Editor
Dr. Seyda Bucak
Yeditepe University
Department of Chemical Engineering
26 Agustos Yerleskesi
34755 Istanbul
Kayisdagi
Turkey
seyda@yeditepe.edu.tr

ISSN 0340-255X e-ISSN 1437-8027
ISBN 978-3-642-13460-9 e-ISBN 978-3-642-13461-6
DOI 10.1007/978-3-642-13461-6
Springer Heidelberg Dordrecht London New York

Library of Congress Control Number: 2010933956

© Springer-Verlag Berlin Heidelberg 2010
This work is subject to copyright. All rights are reserved, whether the whole or part of the material is concerned, specifically the rights of translation, reprinting, reuse of illustrations, recitation, broadcasting, reproduction on microfilm or in any other way, and storage in data banks. Duplication of this publication or parts thereof is permitted only under the provisions of the German Copyright Law of September 9, 1965, in its current version, and permission for use must always be obtained from Springer. Violations are liable to prosecution under the German Copyright Law.
The use of general descriptive names, registered names, trademarks, etc. in this publication does not imply, even in the absence of a specific statement, that such names are exempt from the relevant protective laws and regulations and therefore free for general use.

Cover design: eStudio Calamar S.L.

Printed on acid-free paper

Springer is part of Springer Science+Business Media (www.springer.com)

Preface

European Colloid and Interface Society (ECIS) Conference takes place every year at different places in Europe. Since the initiation in 1986 these meetings have developed to be an inherent part of the scientific community concerning colloid and interface science. Since 2006, the European Chemistry at Interfaces Conference (ECIC) and the European Colloid and Interface Society Conference have merged, allowing for the participation of scientists from more diverse backgrounds and nationalities.

Widening the boarders of Europe, the 23rd ECIS meeting was held in Antalya, Turkey from September 6 to September 11, including the 3rd COST D43 Action Workshop. The meeting was joined by almost 400 participants from groups from different countries not only from Europe but also from all over the world. 83 oral and 314 poster presentations were contributed. The interesting discussions as well as establishing new contacts between scientists were essential parts of the meeting. The presentations, posters and discussions were in the frame:

- Self Assembly
- Interfacial Phenomena
- Colloidal Dispersions and Colloidal Stability
- Polymer Solution, Gels and Phase Behaviour
- Nanostructured Materials
- Biomaterials and Medical Aspects

11 contributions were selected for publication in this special volume of "Progress in Colloid and Polymer Science". B. Siek and Dr. M. Hertel from Springer-DE are gratefully acknowledged.

The Volume editors as well as most contributors are already looking forward to the 24th meeting that will take place in September 2010 in Prague, Czeck Republic.

The 23rd ECIS Conference was kindly sponsored by Atomika, Anton Paar, BiolinScientific, Springer, RSC and Yeditepe University, and was organized by the Chemical Engineering Department of Yeditepe University, Istanbul, Turkey.

Yeditepe University, Turkey — S. Bucak
Lund University, Sweden — U. Olsson

Contents

COST D43 Action

Progr Colloid Polym Sci (2010) 137:1–4
DOI: 10.1007/978-3-642-13461-6_1

Confinement Effects on the Microphase Separation and Swelling of Block Copolymer Films

Larisa Tsarkova

Abstract Confinement significantly affects the main physical properties of soft materials, in particular solvent – polymer interactions. Microphase separation in block copolymer films is known to be sensitive to the changes in the system parameters and experimental conditions. Here we present recent studies on the solvent-assisted self-assembly of block copolymers, and their swelling behavior under controlled variation of the the film thickness, interfacial interactions, and of the solvent vapor concentration.

Keywords Confinement • soft matter • block copolymers • swelling • morphological behavior

Introduction

The current trends towards miniaturization of functional systems and devises have driven the studies of confinement effects (finite film thickness and the nature of the binding interfaces) on the fundamental physical properties of soft materials. Rapid development of novel sensor and lab-on-chip technologies, and of polymer-based stimuli-responsive materials, raises the question of changes in solvent – polymer interactions under confinement.

Both, organo- and water-soluble polymers have been subjected to the studies of swelling dynamics, of the distribution of the solvent within thin films and of the diffusivity of the solvent molecules using different experimental techniques including spectroscopic ellipsometry (SE) [1], optical reflectometry, X-ray or neutron reflectivity [2, 3], grazing incidence small angle X-ray scattering [4], quartz crystal microbalance [5], and other complementary techniques.

L. Tsarkova
Physikalische Chemie II, Universität Bayreuth, 95440, Bayreuth, Germany
e-mail: larisa.tsarkova@uniayreuth.de

Up to now published results contain non-consistent or even contradicting information concerning the influence of the confinement on the solvent absorption and distribution in a swollen film. In particular, the correlation between the absolute solvent up-take and the film thickness, as well as the effect of the substrate interactions on the solvent concentration profile through the film remain unclear.

Block copolymers attract enormous interest due to their intrinsic ability to self-assembly into a variety of well-defined nanostructures (see recent reviews [6–9]). Here we address solvent-assisted self-assembly of block copolymers, and present recent studies on the response of the microphase separated patterns toward solvent uptake under the controlled variation of the the film thickness, interfacial interactions, and of the solvent concentration in the atmosphere. This research brings new insights into the degrees of freedom which govern self-assembly of soft matter in confined geometry and allows to discover novel approaches toward fabrication and functioning of nano-structured functional materials.

Methods and Materials

Two types of diblock copolymer materials have been studied. Cylinder-forming polystyrene-*b*-polybutadiene copolymers with total molecular weights of $M_w = 47.3$ kg/mol (denoted as SB^{47}), and $M_w = 70.0$ kg/mol (SB^{70}) were purchased from (Polymer Source Inc). For detailed characterisation of thin film behavior of SB polymers see [10–12]. Lamella-forming polystyrene-*b*-poly(2-vinyl pyridine) diblock copolymer with a total molecular weights of $M_n =$ 99 kg/mol (denoted as SV^{99}) was synthesized by sequential living anionic polymerization [13].

After additional drying to remove the residual solvent, the spin-coated films were exposed to a controlled atmosphere of selective (toluene) or non-selective (chloroform) solvent. The

© Springer-Verlag Berlin Heidelberg 2010

swollen thickness h_{sw} in the presence of a given vapor pressure was measured by *in-situ* spectroscopic ellipsometry (Sentech SE 850) in a home-made set-up which allowed ellipsometric measurements under full control over the solvent vapor atmosphere p/p_0 where p_0 is the solvent vapor pressure at saturation and p is the actual pressure adjusted by a combination of the saturated vapor flow and of dry nitrogen flow [14, 13], or by a difference in the temperature of the solvent vapor and of the film [15, 16]. Before and when possible after swelling in a solvent vapor, the thickness h_{dry} of the samples was measured which gave direct access to the polymer volume fraction ϕ in a swollen film ($\phi = h_{dr}/h_{sw}$). The structure at the surface and in the interior of the films was characterized by scanning force microscopy (SFM).

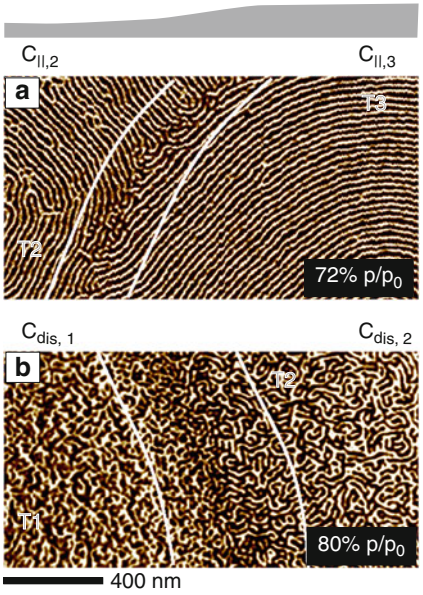

Fig. 1 SFM phase images (scale 10°) of SB^{47} films swollen at (a) $p/p_0 = 72\%$ showing lying cylinders with a high degree of a long-range order, and (b) at $p/p_0 = 80\%$ showing a phase-separated pattern with a low long-range order (a disordered cylinder phase) [15]. White lines are guides to the eye; they mark the borders of the areas with a constant film thickness. Upper schematic introduces the mesoscale surface topography at respective imaged parts of the film

Results and Discussion

Microphase separation in swollen block copolymer films

A non-selective solvent in a swollen film acts as a plasticizer and effectively lowers the glass-transition temperature of the glassy components. As a result, the chain mobility is considerably enhanced without a significant increase in the processing temperature.

In our experiments, the quench to the glassy state of the polystyrene block has been achieved within tens of seconds, and has been shown not to alter the phase separation in a swollen state[16]. Figure 1a presents the surface structures in SB^{47} films which have been exposed to a relative vapor pressure of $p/p_0 = 72\%$. Through the entire sample, the cylinders (white stripes) are aligned parallel to the film plane [12]. Shown in 1b are the typical surface pattern in SB^{47} films after exposure to the vapor pressure p/p_0 heigher than 80%. The in-plane order of the microdomains is dramatically reduced which indicates the vicinity of the system to the oder disorder transition (ODT), meaning that the interface between two blocks in the swollen film is subjected to strong composition fluctuations.

The increase of solvent concentration in SB^{47} films upon raising the partial pressure of chloroform vapor and the related loss of the long-range order can be explained in terms of so called "dilution approximation" for the bulk block copolymer phases [17, 18]. The above results clearly demonstrate high sensitivity of the solvent-polymer interactions towards solvent content. Therefore, the microphase separated structures in swollen films can be used as a qualitative measure of the degree of swelling in block copolymer films [16, 10].

Surface energetics-mediated swelling of block copolymers

Current strategies to control and optimise block copolymer patterns successfully exploit variation of the chemistry of the substrates [19]. This approach is often referred to as "'bottom-up"' to emphacise the decisive role of the surface interactions in the structure formation. Earlier has been shown that phase behavior in SB^{47} melts exhibits strong dependence on the type of the substrates, i.e on the preferential adsorption of block copolymer components to the film interfaces [11]. On nearly neutral substrate (carbon-coated silicon) cylinders are aligned parallel to the surface (C). Under the strong surface field on silicon substrates, a transitions to non-bulk perforated lamella (PL) phase occurs in up to four-layers-thick films.

Figure 2 shows microphase separated patterns in quenched SB^{70} films which have been solvent-annealed under identical conditions however on different substrates: on silicon substrate (a), and on carbon coating (b). Both films exhibit a coexistence of a dot-like pattern (up-standing polystyrene cylinders $C_\perp$) with worm-like features which can be assigned to lying cylinders $C_\parallel$. The detailed morphological analysis is beyond the scope of this paper. Important for the present discussion is that strong surface interactions support hexagonally ordered pattern of white dots (a), while on low-energy weakly interacting carbon coating a dot-like pattern maintains a poor ordering. SFM height images of the surface topography clearly indicate greater film roughness of

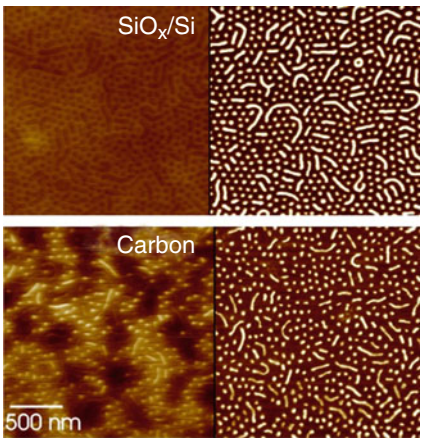

Fig. 2 SFM height (left, scale 10 nm) and phase (scale 10°) images of microphase-separated patterns in 50 nm thick SB^{70} films on attractive $Si/Si0_x$-covered surface (a) and on neutral carbon coating (b) both annealed at 80% of the saturated chloroform vapor pressure

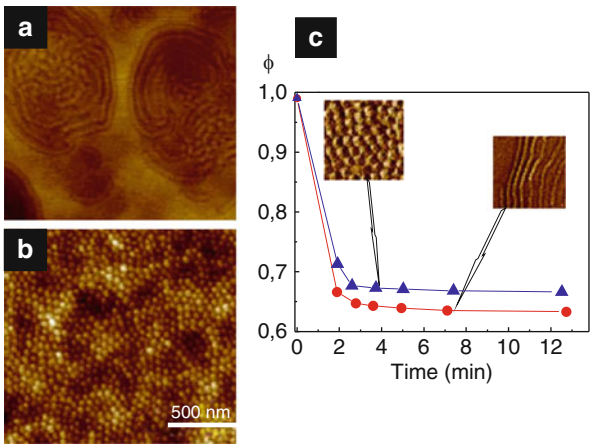

Fig. 3 SFM height images (scale 20 nm) of representative surface structures in SV^{99} films after spin-coating from chloroform solution (a), and from toluene solution (b). (c) Swelling kinetics of ≈ 400 nm thick SV^{99} films with the starting micelle (triangles) and lamella (circles) morphology

quenched carbon-supported films. Both above observations suggest stronger fluctuations in swollen carbon-supported films. Using similar line of arguments as in case of SB^{47} films (Figure 1) we conclude that under identical swelling conditions carbon-supported films up-take more solvent as compared to the films on the silicon substrates.

Recent research established a decisive contribution of the affinity of the solvent molecules toward the substrate on the swelling of hydrophilic polymers with water vapor. Vogt et al have demonstrated that the concentration of water near an interface is influenced by the chemistry of the substrate. A hydrophilic substrate accumulates water at the substrate/polymer interface which leads to a gradient in water concentration along the depth of the film [2]. In contrast, depletion of water from a hydrophobic substrate creates a gradient in water concentration through the film, and leads to a strong reduction in the equilibrium uptake with decreasing the film thickness [5].

Presented here results indicate that the distribution of the solvent in the depth of the film and the accumulation/depletion of a solvent at the polymer/substrate interface should be considered not only in terms of the solvent-substrate interactions, but rather in terms of "surface fields", i.e. of the difference between the solvent-substrate and solvent-polymer interactions, with the latter being quite sensitive to the particular swelling conditions and to the sample preparation [20–22].

Microstructure response to the swelling of block copolymer films

Along with the surface interactions, the swelling behavior of polymer films is affected by the chain conformation which is imposed by the confined geometry and by the film preparation [20–22, 13].

Figure 3a, b displays SFM images of SV^{99} films which have been prepared from chloroform and from toluene solutions, correspondingly. The mixed pattern of featureless areas and round-shaped stripes in Figure 3a can be identified with the in-plane lamella and perpendicular-oriented lamellae, respectively. The microstructure prepared from toluene solutions (Figure 3b) is attributed to poly(2-vinylpyridine) micelles surrounded by the polystyrene shell. The micelle morphology is a result of the SV^{99} self-assembly in a selective solvent [13]. We make use of this morphological difference to study the microstructure response toward solvent up-take by block copolymer films.

Figure 3c displays swelling kinetics of two SV^{99} films with the same initial thickness h_{dr} but different microphase separated structures. The curves show fast swelling behavior when up to 97% of the maximal degree of swelling is achieved within the first several minutes, and does not change significantly after a long term annealing for ≈ 40 hours. Another important result is up to 10% larger swelling (smaller ϕ) of SV^{99} films with the initial bulk lamella morphology as compared to the films with the non-bulk micelle phase [13].

This difference is likely associated with the chain expansion/contraction relative to the interface between the blocks within the particular morphology. In analogy to solid inorganic materials whose solubility increases under external pressure and to colloid systems where the capillary pressure leads to the increase of the solubility (Ostwald ripening effect), one would intuitively expect larger swelling of the polymer chains which form non-bulk structure due to their stronger perturbation. However, we observed an opposite effect, which has to be considered in computer simulations and analytical theories on molecular conformations of block polymer chains in microdomain space.

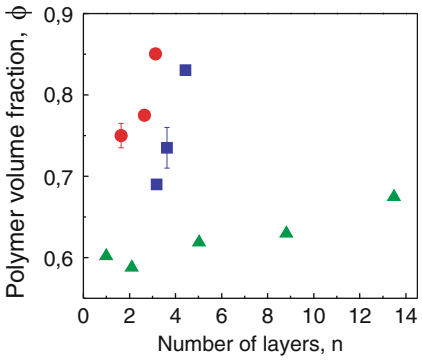

Fig. 4 Polymer volume fraction $\phi = h_{dry}/h_{sw}$ in swollen films of two polystyrene-*b*-polybutadiene diblock copolymers (SB^{47} (circles) and SB^{70} (squares)) which have been equilibrated at $p/p_0 = 50\%$ of the partial chloroform (non-selective solvent) vapor pressure [15], and of SV^{99} films (triangles) equilibrated under $p/p_0 = 80\%$ of toluene (selective solvent) [13] versus the number of layers (film thickness normalized by the respective a_0 in bulk)

Macroscopic swelling of block copolymer films

Using SE measurements under precise control of the solvent atmosphere we quantified the equilibrium ϕ which is inversely proportional to the degree of swelling (Figure 4). Despite the differences in the molecular weight and composition of the studied block copolymers, in the solvent quality and in the experimental conditions which control the solvent atmosphere (see Methods section), Figure 4 summarizes that at a constant vapor pressure the equilibrium ϕ for each polymer becomes smaller as the film thickness h_{dr} decreases. The decrease of the solvent uptake by relatively thick SV^{99} film excludes a substantial contribution of an excess solvent layer at the polymer-substrate interface to an enhanced swelling of ultrathin films.

Conclusions

The swelling and the corresponding morphological behavior of cylinder- and lamella-forming diblock copolymers in thin films have been studied by combined *in-situ* spectroscopic ellipsometry and SFM measurements. The confinement of the film and the presence of the interfaces leads to a more than 10% increase of the solvent up-take with decreasing film thickness. Micro-confinement to a non-bulk structures declines the absolute swelling compared to the films with a bulk microstructure. The sensitivity of the microphase separated patterns toward solvent concentration and the interaction at the substrate has been used additionally to ellipsometry measurements to quantify the swelling behavior. We believe that our results reveal novel fundamental insights to the relationship between the molecular confinement on a microscale and the macro response of soft materials towards external stimuli.

Acknowledgements The author thanks J. Gensel and U. Zettl who contributed to parts of the reported results. This work was carried out in the framework of the "Sonderforschungsbereich 481" (TP B7) funded by the German Science Foundation (DFG).

References

1. Y. Tang, J.R. Lu, A.L. Lewis, T.A. Vick, P.W. Stratford, Macromolecules **35**(10), 3955 (2002)
2. B.D. Vogt, C.L. Soles, R.L. Jones, C.Y. Wang, E.K. Lin, W.I. Wu, S.K. Satija, D.L. Goldfarb, M. Angelopoulos, Langmuir **20**(13), 5285 (2004)
3. M. Mukherjee, A. Singh, J. Daillant, A. Menelle, F. Cousin, Macromolecules **40**(4), 1073 (2007)
4. W. Wang, K. Troll, G. Kaune, E. Metwalli, M. Ruderer, K. Skrabania, A. Laschewsky, S.V. Roth, C.M. Papadakis, P. Mueller-Buschbaum, Macromolecules **41**(9), 3209 (2008)
5. B.D. Vogt, C.L. Soles, H.J. Lee, E.K. Lin, W. Wu, Polymer **46**(5), 1635 (2005)
6. C. Park, J. Yoon, E.L. Thomas, Polymer **44**(25), 6725 (2003)
7. Z. Nie, E. Kumacheva, Nature Materials **7**(4), 277 (2008)
8. W. van Zoelen, G. ten Brinke, Soft Matter **5**(8), 1568 (2009)
9. H.C. Kim, S.M. Park, W.D. Hinsberg, Chemical Reviews **110**(1), 146 (2010)
10. L. Tsarkova, G.J.A. Sevink, G. Krausch, Advances in Polymer Science 227, 33–74 (2010)
11. L. Tsarkova, A. Knoll, G. Krausch, R. Magerle, Macromolecules **39**, 3608 (2006)
12. A. Knoll, L. Tsarkova, G. Krausch, Nano Letters **7**(3), 843 (2007)
13. J. Gensel, C. Liedel, H.G. Schoberth, L. Tsarkova, Soft Matter **5** (13), 2534 (2009)
14. V. Olszowka, L. Tsarkova, A. Boker, Soft Matter **5**, 812 (2009)
15. U. Zettl, A. Knoll, L. Tsarkova, Langmuir **26**(9), 6610 (2010)
16. A. Knoll, R. Magerle, G. Krausch, Journal of Chemical Physics **120**(2), 1105 (2004)
17. E. Helfand, Y. Tagami, J. Chem. Phys. **56**(7), 3592 (1972)
18. G.H. Fredrickson, L. Leibler, Macromolecules **22**(3), 1238 (1989)
19. J.Y. Cheng, C.A. Ross, H.I. Smith, E.L. Thomas, Advanced Materials **18**, 2505 (2006)
20. M.H. Mondal, M. Mukherjee, K. Kawashima, K. Nishida, T. Kanaya, Macromolecules **42**(3), 732 (2009)
21. D.R. Barbero, U. Steiner, Physical Review Letters **102**(24), 248303 (2009)
22. J. Perlich, V. Koerstgens, E. Metwalli, L. Schulz, R. Georgii, P. Mueller-Buschbaum, Macromolecules **42**(1), 337 (2009)

Progr Colloid Polym Sci (2010) 137:5–8
DOI: 10.1007/978-3-642-13461-6_2

The Structure of Dodecanamide Monolayers Adsorbed on Graphite

Tej Bhinde[1], Thomas Arnold[2], and Stuart M. Clarke[1]

Abstract A combination of synchrotron X-ray and neutron diffraction have been used to characterise the sub-monolayer (low-coverage) crystalline structure of dodecanamide [CH_3-$(CH_2)_{10}$-$CONH_2$] adsorbed on graphite. The calculated structure reveals that the molecules lie flat on the graphite surface. The amide head-groups hydrogen-bond into dimers, and, significantly, adjacent dimers form further hydrogen bonds yielding extended chains in good agreement with previous STM results. This monolayer has a very high stability, as observed in its melting point which is significantly higher than the bulk melting point even at these low coverages. The characteristics of the hydrogen bonds are found to be in close agreement with those reported in the bulk crystals. The coverage dependence of the structure is discussed.

Keywords Amide • Monolayer structure • Graphite • X-ray neutron diffraction • Hydrogen bond

Introduction

The amide functional group is central to many natural and synthetic species, such as DNA, polypeptides and nylon, and is interesting particularly in its ability to form strong hydrogen bonds [1]. These species also have important commercial applications when adsorbed at surfaces for example as friction modifiers [2, 3], although these monolayer systems are difficult to study due to the inaccessible nature of their location at the solid/liquid interface.

Literature contains significant evidence for the formation of solid adsorbed monolayers at temperatures where the bulk adsorbate is liquid for a wide variety of hydrocarbon adsorbates on graphite. These have been studied using a variety of techniques such as X-ray and neutron scattering [4–6], calorimetry [7, 8], Scanning Tunnelling Microscopy (STM) [9] and Nuclear Magnetic Resonance (NMR) [10, 11]. In particular, we have recently reported the formation and behaviour of monolayers of alkyl amides adsorbed on the surface of graphite using Differential Scanning Calorimetry (DSC) [7]. Significantly, the extent of pre-solidification of the monolayer is far greater than other similar materials indicating that these amide layers are considerably more stable. Microscopy has been used to characterise adsorbed layers of alkyl amides on graphite [12, 13, 16, 17]. An STM image of stearoyl amide (C_{18} amide) adsorbed from phenyl octane solution on graphite was interpreted to indicate that the amide head groups hydrogen-bond into dimers, and adjacent dimers could possibly form more hydrogen bonds in the adsorbed layer [16]. A similar interpretation of the structure of an unsaturated amide (oleamide) on graphite was made using Atomic Force Microscopy (AFM) [13]. Other substrates such as MgO have also been utilised [14] and an overview of various systems and techniques used to study these physisorbed layers can be found in reviews published recently [15].

In this work we present synchrotron X-ray and neutron diffraction patterns for the monolayer of dodecanamide, a saturated primary alkyl amide, adsorbed on the surface of graphite. This data provides further evidence for the formation of crystalline molecular layers for this amide adsorbed at low, sub-monolayer coverages. The layers are found to form a close-packed hydrogen-bonded structure in two dimensions. We also observe that this monolayer has a melting point significantly in excess of the bulk melting point.

S.M. Clarke (✉)
[1]BP Institute and Department of Chemistry, University of Cambridge, Madingley Road, Cambridge CB3 0EZ, U.K
e-mail: stuart@bpi.cam.ac.uk
[2]Diamond Light Source Ltd, Diamond House, Chilton, Didcot, OX11 0DE, U.K

© Springer-Verlag Berlin Heidelberg 2010

Experiments and Methods

Protonated dodecanamide for synchrotron experiments was purchased from Sigma Aldrich. For the neutron experiments, deuterated dodecanamide was prepared from the corresponding deuterated acid. The purity of dodecanamide was analysed using NMR, Liquid Chromatography-Mass Spectrometry and elemental analysis and these revealed no evidence of other homologues (>98% pure). X-ray powder diffraction experiments were performed at the Materials Science beam-line X04SA at the Swiss Light Source (SLS), Switzerland at an incident beam wavelength of 0.100 nm (12.4 keV) [18]. Graphite (Papyex, having a specific surface area of 30.1 m^2/g) was dosed with appropriate amounts of amide under vacuum, annealed at 180°C, cut into disks and placed in a 3.5 mm glass capillary. The capillary was then sealed and placed in the beam while spinning (~60 rpm) to enhance powder averaging. Temperature control was achieved using a cryojet. Neutron diffraction experiments were performed on the instrument D20 at the Institut Laue-Lanegevin (ILL) in Grenoble, France at a neutron wavelength of 0.242 nm [19]. The apparatus and procedures used to obtain X-ray and neutron diffraction patterns from adsorbed layers have been described in detail elsewhere [5, 20].

The X-ray pattern is at a nominal coverage of approximately 0.5 equivalent monolayers, while the neutron pattern is at a coverage of 0.8 equivalent monolayers on graphite. These coverages were estimates based upon the area per molecule found for the equivalent fatty acid (dodecanoic acid) [5]. Using the area per molecule calculated in this work, the exact coverage was 0.57 monolayers for the X-ray sample and 0.86 monolayers for the neutron sample. A Silicon standard was used to calibrate the incident beam wavelength for synchrotron X-ray experiments, and to correct for any detector angle offset. The calibrated X-ray graphite pattern was used to correct any offset in the neutron data.

The structure of the layer was determined as described in [21], which essentially involves calculating a pattern based on the Warren/Kjems model [22, 23] for a given structure and then comparing it with the experimental pattern until agreement is obtained. This model includes the characteristic saw-tooth line shape for the 2D reflections and includes preferred orientation of the graphite [22]. The calculated pattern is convoluted with an instrument-specific resolution function, represented here by a Gaussian of appropriate width.

Results and Discussion

Low coverage structure

Figure 1 presents the experimental and calculated X-ray and neutron diffraction patterns from dodecanamide adsorbed on the surface of graphite at sub-monolayer coverage at 300 K. In preparing these patterns, the graphite background has been subtracted, and the intense small angle scattering from the external form of the graphite crystallites has been removed as described previously [5, 24]. The scattering clearly exhibits diffraction peaks with the characteristic saw-tooth line shape of crystalline two-dimensional layers [22, 23]. These patterns thus confirm that dodecanamide forms solid ordered monolayers on the surface of graphite.

Figure 2 (i) shows the schematic structure that was used to fit the experimental monolayer diffraction patterns for dodecanamide. The calculated unit cell parameters for both the X-ray and neutron patterns are shown in Table 1. The tilt of the molecules w.r.t. the a-axis is about 22–24°, in agreement with the stacking angle (23°) found in closed packed structures of alkyl species [25]. Close inspection of the peak positions in the X-ray and neutron data indicate that they are not exactly at same position even after appropriate consideration of detector offset and thermal factors. We attribute this to the difference in coverage between the two patterns: neutron at 0.8 monolayers and X-ray at 0.5 monolayers.

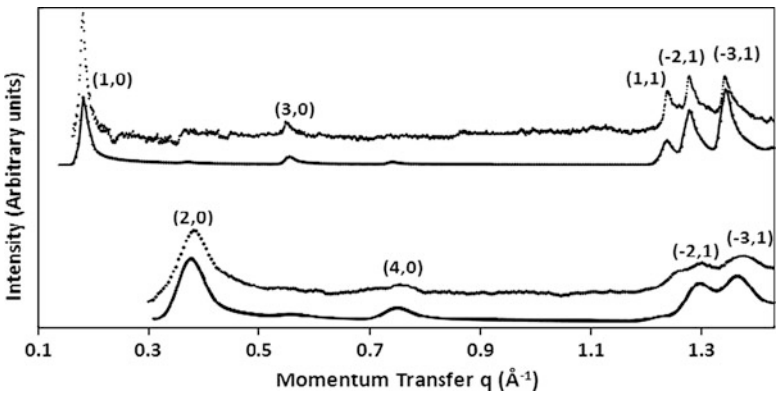

Fig. 1 X-ray (top) and neutron (bottom) diffraction patterns and their fits for the monolayer of dodecanamide on graphite. The solid lines represent the calculated patterns, and the broken points represent the experimental patterns. The indexing of the principal reflections has been indicated. The momentum transfer (scattering vector) is given by $q = (4\pi\sin\theta)/\lambda$, where θ is the scattering angle and λ is the incident beam wavelength

These differences are similar to those reported previously for other hydrocarbons where an increase in coverage has been shown to result in a slight compression in the unit cell (see [4]). Hence the X-ray and neutron data have been fitted independently to slightly different unit cells while preserving the hydrogen-bonding within and between the dimers. For such long molecules, previous experience has shown that it can be very difficult to reliably fit the intensity for the lowest momentum transfer peak due to the very intense small angle scattering from the graphite substrate. We have therefore only considered the peak position for the (1,0) peak in the X-ray pattern.

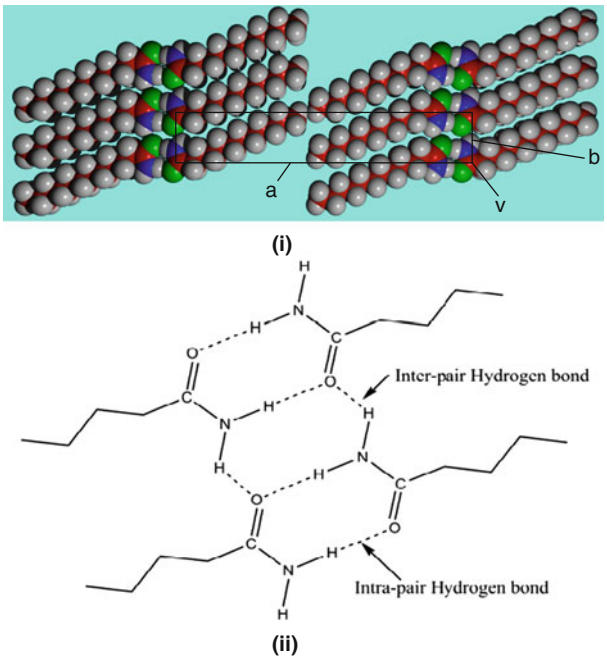

Fig. 2 **(i)** Schematic of the fitted monolayer crystal structure for dodecanamide on graphite. The unit cell is shown by the box. **(ii)** An illustration of the Hydrogen-bond geometry for dodecanamide

Table 1 Structural parameters for the adsorbed monolayer of dodecanamide

Pattern fitted	Unit cell parameters			Molecular tilt w.r.t. a-axis (°)
	a (nm)	b (nm)	ν (°)	
X-ray	3.408	0.515	90.00	22.2
Neutron	3.390	0.514	88.45	23.6

When fitting a limited number of peaks, typical in 2D diffraction patterns, it is desirable to constrain the number of fitted variables as much as possible. Hence we have constrained our modelling to maintain favourable hydrogen bond geometries similar to the bulk and a close-packed structure. With this constraint there are essentially no degrees of freedom available to the molecules as they adsorb on the substrate, as regards to the unit cell, distances between the molecules and rotation angle w.r.t the a-axis. Other models which did not have optimal hydrogen bonding were also considered but these did not fit the diffraction patterns.

It is interesting to note that the a-axis parameter of the patterns is approximately an integral multiple of $\sqrt{3}*a_g$ (8 x $\sqrt{3}*a_g$), where a_g is the lattice parameter of the graphite (0.426 nm). Thus, the monolayer appears to be uniaxially commensurate with the underlying graphite. The structure, however, does not appear to be commensurate in the 'b' direction, suggesting that intermolecular hydrogen bonding dominates the surface potential. This calculated structure is in good agreement with that proposed by STM for a similar amide homologue (stearoyl amide, C_{18}) [16], although these diffraction patterns permit structural determination at a much greater detail as discussed below.

Hydrogen bond geometry

The energies of dimerization on forming an amide hydrogen-bond in solution for various amides fall between 10–20 kJ/mol [1, 26]. Van der Waals interaction energies for molecules in the adsorbed layers, reflected in the melting heats of alkanes, are typically 7 kJ/mol [27]. Hence it is expected that the stronger hydrogen bond should dictate the molecular structure on the surface, as is observed here. The arrangement of molecules in the calculated structure suggests that two amide molecules hydrogen-bond into dimers, and adjacent dimers form additional hydrogen bonds. Table 2 lists the hydrogen-bond parameters extracted from the diffraction patterns above (illustrated in Figure 2 (ii)).

The optimal hydrogen bond for the N-H. . .O contact is achieved when the hydrogen bond is linear [28]. The N-H. . .O distance is in the range 0.285–0.300 nm for various amides in the bulk crystals [29], with the bond angles typically 160°–180° [30]. The hydrogen bond within the dimer

Table 2 Hydrogen bond parameters calculated from the fitted diffraction patterns

Pattern fitted	'Intra-dimer' Hydrogen bond values				'Inter-dimer' Hydrogen Bond values			
	Distance (N. . .O) (nm)	Distance (H. . .O) (nm)	Angle (N-H. . .O) (°)	Angle (C=O..H) (°)	Distance (N-O) (nm)	Distance (H-O) (nm)	Angle (N-H. . .O) (°)	Angle (C=O..H) (°)
X-ray	0.297	0.195	179.23	120.75	0.300	0.235	120.12	114.13
Neutron	0.296	0.193	177.37	117.36	0.296	0.224	126.08	120.09

('intra-dimer' hydrogen bond) calculated for the two-dimensional case here is linear and agrees very well with the bulk crystal (Table 2). The distances and angles reported here are estimated to be accurate up to 0.005 nm and 2° respectively. There are additional pairs of hydrogen bonds between dimers - 'inter-dimer' hydrogen bonds where the N-H. . .O bond is not linear but has an angle of approximately 120° (in accord with similar bulk systems [28]).

By observing the diffraction pattern as a function of temperature, the melting point of the monolayer can be determined with well-defined sharp peaks corresponding to the solid phase of the monolayer becoming much broader peaks corresponding to the liquid phase [31]. We have determined the 2D melting point of dodecanamide to be 428.5 K from neutron diffraction data. This is in good agreement with the value reported from calorimetric studies (429 K) [7]. Importantly this value is well above that of the pure bulk amide (375 K) [7]. We believe this is the first report of such pre-solidification at sub-monolayer coverage. No phase changes in the monolayer were observed from 12K until the melting point.

The neutron monolayer patterns at higher coverage (3 and 5 monolayers-not shown) of this amide on graphite were found to be remarkably similar to the one at 0.8 monolayers coverage, with no significant shifts in the peak positions indicating minimal compression or change in the monolayer. Alkanes show approximately 3–7% compression [32, 4], while carboxylic acids show 1–3% compression in the b-direction [5] on increasing the coverage above a monolayer.

Conclusions

A combination of synchrotron X-ray and neutron diffraction techniques have been used to determine the low-coverage structure of dodecanamide adsorbed on graphite. This molecule adopts a uniaxially commensurate p2 symmetry structure on graphite, which is in agreement with the close packing predictions of Kitaigorodskii [33]. The molecular positions are indicative of the existence of extensive hydrogen bonds which dominate the system. These impart exceptional stability to the monolayer, with higher stability than that seen before for similar species adsorbed on graphite. The hydrogen bond geometry for the different hydrogen bonds present in the system is very similar to bulk (3D) crystals and in agreement with STM studies of a related homologue [16]. Here we have enabled a detail structural analysis which has revealed the symmetry and hydrogen bonding parameters with greater detail. At higher coverage, there is minimal change in the molecular structure. The monolayer melts at a much higher temperature compared to the bulk amide even at sub-monolayer coverage, indicating that this layer is extremely stable.

Acknowledgements The authors thank the Nehru Trust for Cambridge University (TB) and Diamond Light Source for financial assistance. We thank Tamsin Philips and Julia Parker for help with the experiments and also the staff and scientists at ILL, Thomas Hansen and Jacques Torregrossa and at SLS, Antonio Cervellino and Fabia Gozzo, for beam time and technical assistance. This work is based on experiments performed at the Swiss Light Source, Paul Scherrer Institute, Villigen, Switzerland. The research leading to these results has received funding from the European Community's Seventh Framework Programme (FP7/ 2007- 2013) under grant agreement no. 226716.

References

1. Pimentel GC, McClellan AL (1960) The Hydrogen Bond, W. H. Freeman and Co., San Francisco and London
2. Dragnevski KI et al. (2009) Colloids and Surfaces A: Physicochem Engg Aspects 337:47
3. Ramirez MX et al. (2005) J Vinyl Additive Tech 11:9
4. Arnold T et al. (2001) Phys Chem Chem Phys 4:345
5. Bickerstaffe AK et al. (2006) J Phys Chem B 110:5570
6. Espeau P et al. (1997) J Chem Soc, Faraday Trans 93:3201
7. Arnold T, Clarke SM (2007) Langmuir 24:3325
8. Cheah NP et al. (2004) J Phys Chem B 108:4466
9. Giancarlo L et al. (1998) Langmuir 14:1465
10. Alba MD et al. (2009) J Phys Chem C 113:3176
11. Alba MD et al. (2003) Solid State NMR 23:174
12. Lim R et al. (2000) Langmuir 16:7023
13. Miyashita N et al. (2007) Chem Mater 19:4259
14. Arnold, T et al. (2006) Physical Review B 74:085421
15. Bruch, LW et al. (2007) Reviews of Modern Physics 79:1381
16. Takeuchi H et al. (1996) Jap J App Phys 35:3754
17. Zou B et al. (2005) Langmuir 21:1364
18. Gozzo F et al. (2004) J Alloys and Compounds 362:206
19. Hansen TC et al. (2008) Measurement Sci and Tech 19:034001
20. Clarke SM (1989) D Phil. thesis, University of Oxford, Oxford
21. Mowforth CW et al. (1986) J Chem Soc, Faraday Trans 2 82:1621
22. Kjems JK et al. (1976) Physical Review B 13:1446
23. Warren BE (1941) The Physical Review 9:693
24. Cullity BD, Stock SR (2001) Elements of X-Ray diffraction, Prentice Hall Inc., New Jersey
25. Comment by Prof S Rice (Univ of Chicago) in *Faraday Discussion Chem Soc* (1990) 89:247
26. Vinogradov SN, Linnell RH (1971) Hydrogen Bonding, Van Nostrand Reinhold Company
27. Messe L et al. (2005) Langmuir 21:5085
28. Leiserowitz L, Schmidt GMJ (1969) J Chem Soc A:2372
29. Taylor R et al. (1984) Acta Cryst B40:280
30. Gavezzotti A, Filippini G (1994) J Phys Chem 98:4831
31. Warren BE (1990) X-Ray Diffraction, Courier Dover Publications
32. Arnold T et al. (2002) Phys Chem Chem Phys 4:3430
33. Kitaigorodskii AI (1973) Phys. Chem. Vol. 29: Molecular Crystals and Molecules, Academic Press, New York

Progr Colloid Polym Sci (2010) 137:9–12
DOI: 10.1007/978-3-642-13461-6_3

The Structure of Model Membranes Studied by Vibrational Sum Frequency Spectroscopy

Jonathan F.D. Liljeblad[1], Mark W. Rutland[1], Vincent Bulone[2], and C. Magnus Johnson[1]

Abstract The structure and order of insoluble Langmuir monolayers consisting of 1,2-distearoyl-sn-glycero-3-phosphatidylcholine (DSPC or 18:0 PC) and the surrounding water molecules have been investigated by vibrational sum frequency spectroscopy (VSFS). At surface pressures of 1, 15, and 57 mN/m corresponding to molecular areas of 53, 50, and 43 $Å^2$, respectively, the DSPC molecules formed a well ordered film. Both the VSF signal from the methyl stretching vibrations of the lipid and the surrounding water increased with enhanced surface pressure, as a result of the higher surface density and increased order of the system. Water molecules hydrating the polar parts of the headgroup and in close contact to the hydrocarbon groups of the lipid were observed in all three polarization combinations of the laser beams, and distinguished by their different vibrational frequencies.

Keywords Vibrational sum frequency spectroscopy • SFG • DSPC • Langmuir film • membrane

Introduction

Membranes are vital in biological systems since they separate cells from the outside environment and delimit the different subcellular compartments, which each exhibit specific functions. [1] Phospholipids are of great importance as membrane constituents, since they are involved in the regulation of protein transport through lipid bilayers, and are responsible for the fluid characteristics of the membranes. Our main objective is to better understand the molecular mechanisms of the membrane-bound enzymes involved in plant cell wall formation and to exploit this knowledge for the design and biosynthesis of new advanced materials. Membrane lipid components contribute to the control of the activities of the cell wall synthesizing enzymes by assisting the insertion of the proteins in the membrane and stabilizing their conformation. However, the interactions between membrane proteins and the surrounding lipids are poorly understood. Since biological membranes are complex structures difficult to study in their natural state, our approach to analyze protein/lipid interactions and the surface hydration of membranes is based on the use of biomimetic model systems that consist of simple artificial monolayers and bilayers. The information gained from these systems can then be exploited to build more complex models that mimic as closely as possible the structure of natural membranes. The common phospholipid 1,2-distearoyl-sn-glycero-3-phosphatidylcholine (DSPC or 18:0 PC) has been chosen for the studies presented in this work.

An excellent technique for studying the structure, order, and hydration of lipids is vibrational sum frequency spectroscopy (VSFS) combined with a Langmuir trough, which allows the preparation of lipid monolayer films at different controlled surface pressures on a water subphase. VSFS is a second order laser spectroscopy technique with the unique property that it generates vibrational spectra exclusively of molecules residing at surfaces and interfaces. [2] This specificity is due to the fact that the SF signal under the electric dipole approximation solely can be generated in media lacking an inversion center. Thus, it is for example possible to discriminate the very few ordered water molecules at the air/water interface from the large excess of disordered water molecules in the bulk. The VSFS technique can be applied to all interfaces accessible to the laser beams, thereby enabling studies for instance at the liquid/vapor, solid/liquid, and liquid/liquid interfaces. The sum frequency process involves

C.M. Johnson (✉)
[1]Division of Surface and Corrosion Science,
Royal Institute of Technology (KTH),
SE-100 44 Stockholm, Sweden
e-mail: magnusj@kth.se
[2]Division of Glycoscience,
Royal Institute of Technology (KTH)

© Springer-Verlag Berlin Heidelberg 2010

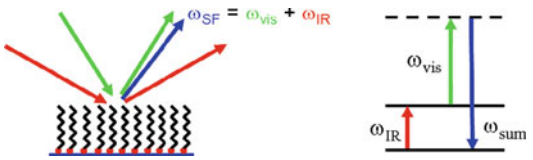

Fig. 1 Scheme of the sum frequency process, where the IR and visible beams overlap at the surface to generate the SF beam. To the right, the SF process is described as a combination of an IR absorption, and an absorption of the visible beam and the subsequent emission of the SF beam (Raman anti-Stokes process)

two pulsed laser beams incident on the sample, one at a fixed visible frequency and one tunable in the infrared region. These beams overlap spacially and temporally at the interface, inducing a Raman anti-Stokes and an infrared process, respectively, resulting in an emission of the SF beam, as shown in figure 1. The emitted beam has a frequency equal to the sum of the frequencies of the incident beams ($\omega_{SF} = \omega_{vis} + \omega_{IR}$) and carries information about the nature of the interfacial molecules and their orientation.

The intensity of the SF beam is proportional to the square of the second order susceptibility $\chi^{(2)}$, and the intensities of the incident beams. $\chi^{(2)}$ can be separated into a nonresonant ($\chi^{(2)}_{NR}$), and resonant contributions ($\chi^{(2)}_{R,n}$) summed over all vibrations contributing to the SF signal. Further, the macroscopic nonlinear susceptibility $\chi^{(2)}$ is directly related to the molecular property $\beta^{(2)}$, the second order hyperpolarizability, by equation 1.

$$\chi^{(2)}_{R,n} = \frac{N_s}{\varepsilon_0}\left\langle \beta^{(2)}_n \right\rangle \quad (1)$$

N_s is the molecular surface number density and the brackets indicate an average over all molecular orientations. The hyperpolarizability can be expressed in terms of the infrared (μ_γ) and Raman ($\alpha_{\alpha\beta}$) transition moments, as shown in equation 2.

$$\beta^{(2)}_{\alpha\beta\gamma} = \frac{\alpha_{\alpha\beta}\mu_\gamma}{\omega_n - \omega_{IR} - i\Gamma} \quad (2)$$

ω_n is a vibrational transition frequency, ω_{IR} the frequency of the IR beam, and Γ the homogeneous bandwidth.

Materials and Methods

DSPC was purchased from Avanti Polar Lipids, USA (concentration typically within ± 10 % of the stated value), and the water used was from a Millipore system, featuring a conductivity of 18.2 MΩ·cm and an organic content of < 4 ppb. To prepare the monolayers, a 1 mg/ml solution of lipid

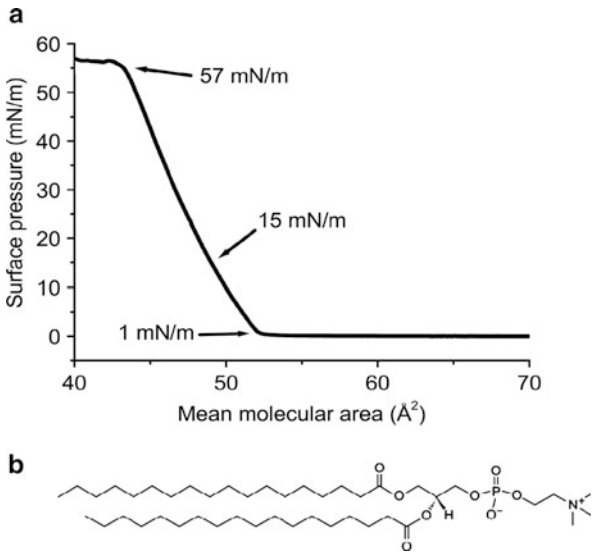

Fig. 2 LB compression isotherm of DSPC, and molecular structure of the glycerophospholipid

in $CHCl_3$ (SigmaAldrich, ≥ 99.8 %, stabilized with amylene) was spread at the water surface (20±1 °C) of a Langmuir trough[3], (Minimicro 1S, KSV Instruments). The monolayer was left for 15 minutes for the chloroform to fully evaporate before the compression to the desired surface pressure was started. The compression isotherm in figure 2 was performed at 5 mm/min and recorded using a KSV 5000 LB system equipped with a platinum Wilhelmy plate.

The VSFS system has been described previously in detail.[4] Briefly, a Nd:YAG laser (EKSPLA) generates a fundamental beam (1064 nm, 20 Hz, 30 mJ), which is directed into an optical parametric generator/optical parametric amplifier (OPG/OPA, Laservision) to generate a visible beam at 532 nm and a tunable infrared beam (1000–4000 cm^{-1}). The SF beam is detected by a monochromator, a photomultiplier tube, a boxcar integrator, and a PC. Spectra were acquired by the ssp, ppp, and sps polarization combinations, where the letters refer to the polarization of the SF, visible, and IR beams, respectively. The letters p and s denote polarizations parallel and perpendicular to the plane of incidence, respectively.

Results and Discussion

Figure 2 shows the compression isotherm of DSPC, which is in agreement with data in the literature.[5] This phospholipid displays a break point at approximately 53 $Å^2$, indicative of rapidly increased interactions, and a collapse point close to 43 $Å^2$. [5, 6] Sum frequency spectra have been acquired of pure water, and at three different surface pressures of DSPC,

1, 15, and 57 mN/m, corresponding to molecular areas of 53, 50, and 43 Å^2, respectively. The reasons for using water as the starting point for all VSF experiments were to certify that no contaminants were present and for obtaining a reference spectrum. In the water spectrum shown in figure 3, the main features are two broad bands at ~3250 and 3430 cm^{-1}, and a sharp peak at ~3700 cm^{-1}. The broad bands correspond to "ice-like" and "liquid-like" hydrogen-bonded water, respectively, referring to the dominant resonances in bulk spectra of ice and liquid water, and the sharp peak originates from non hydrogen-bonded OH bonds protruding out into the vapor phase. [7, 8] Thus, only water molecules in the first monolayer give rise to the strong peak at 3700 cm^{-1}, evidencing the surface sensitivity of VSFS.

Upon spreading of DSPC on the water surface, the VSF spectrum changes drastically. All ssp spectra acquired at different surface pressures of DSPC display prominent features around 2875 and 2942 cm^{-1}, assigned to the symmetric methyl stretch, $\nu_s(CH_3)$, and the Fermi resonance, $FR(CH_3)$, between $\nu_s(CH_3)$ and the methyl bend, respectively. [9] Additionally, the symmetric methylene stretch, $\nu_s(CH_2)$, appears as a weak peak at 2842 cm^{-1}, and the antisymmetric methylene mode, $\nu_a(CH_2)$, is observed as a shoulder at 2911 cm^{-1}. [9] As shown in the spectrum, $\nu_s(CH_2)$ exhibits a significantly weaker intensity than $\nu_s(CH_3)$, indicating well ordered lipid monolayers in a nearly all-trans configuration for all surface pressures studied. [10] Since the SF signal is zero in media with inversion symmetry, no CH_2 signal is expected for chains in an all-trans chain configuration, due to the presence of an inversion center between each successive pair of methylene groups. Had a significant number of gauche defects been present, this would have been revealed by an appreciably more intense CH_2 signal. [10] As figure 3 shows, the $\nu_s(CH_3)/\nu_s(CH_2)$ intensity ratio increases slightly at higher surface pressures, indicating an increasing order in the monolayer. Thus, the enhancement in $\nu_s(CH_3)$ signal upon increasing surface pressure is due to both an enhanced order in the monolayer and a larger number of molecules probed by the laser beams when the film is compressed.

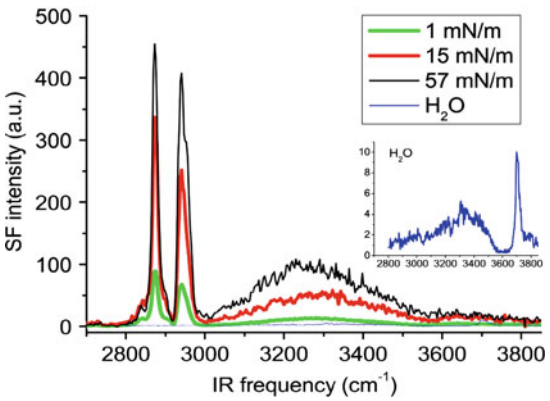

Fig. 3 VSF spectra of a DSPC monolayer at a water surface acquired with the ssp polarization, at surface pressures of 1, 15, and 57 mN/m. The weak water spectrum in the main graph has been magnified in the inset

In the spectra of DSPC monolayers, the water region extending from ~3000–3850 cm^{-1} shows two broad bands with central frequencies at around 3280 and 3640 cm^{-1}. The band at 3280 cm^{-1} corresponds to strongly hydrogen bonded water molecules hydrating the hydrophilic parts of the phospholipid headgroup, whereas the band centered at 3640 cm^{-1} originates from non hydrogen-bonded water molecules weakly interacting with the hydrocarbon groups of the lipid. [11] Since the latter band is absent in pure water, it can directly be concluded that it arises from interactions between water and the phospholipid. It is noteworthy that DSPC carries hydrocarbon groups in its headgroup, in addition to the long hydrocarbon chains of the esterified C18 fatty acids (figure 2). Thus, the water molecules giving rise to the band at 3640 cm^{-1} could be present in the proximity of both hydrocarbon parts of the molecule. As seen in figure 3, the intensity of the water bands centered at 3280 and 3640 cm^{-1} increases when enhancing the surface pressure. However, the shape of the band remains fairly constant, suggesting that the structure of the water molecules remains fairly constant over this surface pressure range. Thus, the intensity increase mainly originates from an increased number of ordered water molecules being probed. To completely confirm the exact nature of a potential rearrangement of water molecules, a detailed polarization analysis would be required, but is beyond the scope of this article.

Extended studies by the polarization combinations ppp and sps yielded additional information regarding the structure and order of DSPC and the surrounding water molecules, since some peaks only were observed at certain polarizations due to the average orientation of the functional group. Figure 4 displays ppp and sps spectra of DSPC acquired at 1 mN/m. These spectra clearly differ from the ssp spectrum in the CH stretching region at 2800–3000 cm^{-1}. The major peak in the ppp and sps spectra is assigned to the antisymmetric methyl stretch, $\nu_a(CH_3)$ at ~2958 cm^{-1}, whereas $\nu_s(CH_3)$ is considerably weaker. This results from the fact that symmetric and antisymmetric vibrations have transition moments pointing in different directions, and thus the ssp, ppp, and sps polarizations probe these vibrations differently. As in the ssp spectrum, the CH_2 peaks are very weak in the ppp and sps spectra in these nearly all-trans chains.

In addition, differences are detected between the spectra in the water region. The sps spectrum displays a very broad band centered at around 3600 cm^{-1}, and the ppp spectrum exhibits a maximum at 3545 cm^{-1}, evidently separated from the ssp maximum at 3640 cm^{-1}. The ppp maximum is actually located close to the minimum of the ssp spectrum.

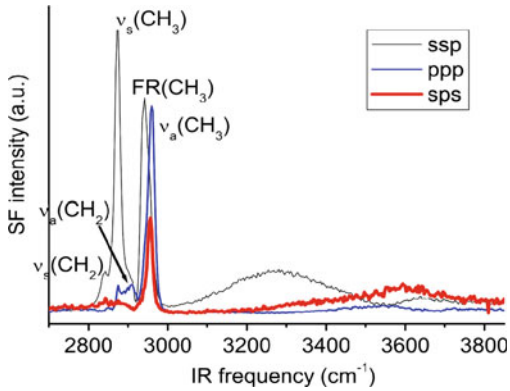

Fig. 4 Sum frequency spectra of DSPC and the surrounding water molecules under the ssp, ppp, and sps polarizations. The ssp spectrum is identical to that in figure 3.

This suggests that the water molecules giving rise to the bands in the three polarization combinations do not necessarily reside in the same environment, illustrating the value of performing VSFS experiments with several polarization combinations. Similarly to the ssp spectrum, the high frequencies of the water bands in the ppp and sps spectra suggest the occurrence of water molecules that weakly interact with the lipid molecules.

Conclusions

The structure and order of DSPC as well as the surrounding water molecules were investigated by VSFS in a LB trough at various surface pressures. The VSF spectra demonstrate that the DSPC molecules form a well ordered surface film at all surface pressures examined. At higher pressures, both the hydrocarbon and the water signals increased as a result of an even increased order and a higher surface number density of the lipid molecules and the associated water molecules. Additionally, spectra acquired with different polarization combinations revealed that several classes of water molecules in contact with the lipid exist, ranging from strongly bound water hydrating the polar parts of the headgroup, to water molecules weakly interacting with the hydrocarbon regions. The magnitude of water bands observed confirms the complex behavior of water, and further studies are in progress in our group to investigate in more detail the exact location of the water molecules in the proximity of the phospholipid.

Acknowledgements The authors thank Dr. Eric Tyrode (KTH) for valuable discussions. This project was supported by the Swedish Centre for Biomimetic Fiber Engineering (Biomime), the Swedish foundation for strategic research (SSF), and the Swedish research council (VR). Rutland is a fellow of VR and Johnson holds an Ingvar Carlsson (SSF) grant.

References

1. Berg JM, Tymoczko JL, Stryer L (2002) Biochemistry 5th ed., W.H. Freeman & Co, New York
2. Shen YR (1989) Nature 337: 519
3. Kaganer VM, Mohwald H, Dutta P (1999) Rev Mod Phys 71: 779
4. Johnson CM, Tyrode E, Baldelli S, Rutland MW, Leygraf C (2005) J Phys Chem B 109: 321
5. Mitchell ML, Dluhy RA (1988) J Am Chem Soc 110: 712
6. Phillips MC, Chapman D (1968) Biochim Biophys Acta, Biomembr 163: 301
7. Du Q, Superfine R, Freysz E, Shen YR (1993) Phys Rev Lett 70: 2313
8. Wei X, Shen YR (2001) Phys Rev Lett 86: 4799
9. Lu R, Gan W, Wu B-h, Zhang Z, Guo Y, Wang H-f., (2005) J Phys Chem B 109: 14118
10. Guyot-Sionnest P, Hunt JH, Shen YR (1987) Phys Rev Lett 59: 1597
11. Tyrode E, Johnson CM, Kumpulainen A, Rutland MW, Claesson (2005) J Am Chem Soc 127: 16848

Progr Colloid Polym Sci (2010) 137:13–18
DOI: 10.1007/978-3-642-13461-6_4

Outstanding Stability of Poorly-protected Pickering Emulsions

Mathieu Destribats[1,3], Serge Ravaine[1], Valérie Heroguez[2], Fernando Leal-Calderon[3], and Véronique Schmitt[1]

Abstract Pickering emulsions are surfactant-free emulsions, stabilized solely by colloidal particles. Most of these emulsions exhibit exceptionally high stability and bulk elasticity. In order to investigate the effect of interfacial particle interactions and structure on the emulsions properties, we synthesized particles (silica, core-shell latexes, neighborite cubes) whose interactions can be tuned by a composition variable (pH, ionic strength. . .) leading to stimulus-responsive materials. The systems could switch from kinetically stable to unstable on demand. Surprisingly, some kinetically stable emulsions were obtained at very low interfacial particle coverage. We demonstrate the generality of this phenomenology using different types of particles and we discuss the origin of the stabilization in the poorly-covered regime.

Keywords emulsions • solid stabilizers • stability • stimulus-responsive • pH and salt sensitivity • dipolar interactions

Introduction

Emulsions are metastable dispersions of at least one liquid, forming small drops, in another immiscible liquid called the continuous phase. This type of system has been and remains widely studied in academic and industrial research as it is of tremendous interest in various sectors (foods, cosmetics, pharmaceutics, painting, road surfacing, oil recovery, etc.). Usually emulsions are kinetically stabilized by surface-active species like low molecular weight surfactants, polymers or proteins. Since the pioneering studies of Ramsden and Pickering about 100 years ago [1, 2], it is known that colloidal particles can also stabilize emulsions: these systems are referred to as particle-stabilized emulsions or Pickering emulsions. A wide variety of particles with variable sizes (from the nanometer to several micrometers) can be used as stabilizers: mineral powders, solid organic particles, microgels, or even naturally occurring organic particles like spores [3]. Particle-stabilized emulsions may exhibit unusual features compared to conventional surfactant-stabilized ones [4–6]: large droplet-size range (from 1μm to more than 1 cm), rigid interfaces due to strong attractive interactions between particles, non-spherical shapes of the droplets, long-term kinetic stability against coalescence and ripening .... Using particles, the concentration of conventional emulsifying agents can be reduced and hazardous surfactants may be replaced by less harmful materials. In some cases, organic surfactants can even be completely avoided. In addition, particle-stabilized emulsions can be used as precursors to elaborate complex materials [4, 7–17]. For these reasons, the field of particle-stabilized emulsions is of growing interest.

One can summarize some general rules concerning particle-stabilized emulsions arising from the recent literature as follows [18–20]: i) the particles have to be partially wetted by both water and oil phases for emulsion stabilization to be efficient, ii) a similar rule as the Bancroft rule for surfactant-stabilized emulsions holds [21]: the continuous phase of the preferred emulsion is usually the one in which the particles are preferentially dispersed. The particle hydrophobicity is related to the contact angle θ (measured through the water phase) defined as the angle between the particle tangent in the water phase and the liquid-liquid interface. A particle that is preferentially wetted by water ($\theta < 90°$) will more likely stabilize a direct emulsion (o/w) whereas a reverse emulsion (w/o) will more likely be stabilized by

V. Schmitt (✉)
[1]Centre de Recherche Paul Pascal, Université Bordeaux 1, UPR 8641-CNRS, 115 Avenue du Dr Albert Schweitzer, 33600 Pessac, France
e-mail: schmitt@crpp-bordeaux.cnrs.fr
[2]Laboratoire de Chimie des Polymères Organiques, Université Bordeaux 1, CNRS, ENSCBP UMR 5629, 16 Avenue Pey-Berland, 33607 PESSAC, France
[3]TREFLE, Université Bordeaux 1, CNRS UMR 8508, Avenue des Facultés, 33405 Talence, France

©Springer-Verlag Berlin Heidelberg 2010

a more hydrophobic particle ($\theta > 90°$), iii) once the particles are at the interface, their anchoring may be considered as irreversible due to the large energy needed to remove them from the interface compared to thermal energy, iv) the irreversible anchoring is responsible for the so-called "limited coalescence" process [22] that allows an easy control of the final drop size by an appropriate choice of the stabilizer amount. During emulsification the energy input enables creating more oil-water interface than the particles can actually stabilize. Hence when stirring is stopped, the partially unprotected droplets coalesce, reducing the total amount of interface. This phenomenon is arrested when the drops are protected enough against coalescence. Therefore, the initial particle amount in the system and the particles arrangement at the interface determine the final drop size. Assuming that all the particles are adsorbed at the oil-water interface, the final drop diameter D is given by:

$$\frac{1}{D} = \frac{m_p}{4C\rho_p d_p V_d} \quad (1)$$

where m_p is the mass of particles, ρ_p is the particle density, V_d is the volume of the dispersed phase and C is the surface coverage *i.e.* the fraction of the droplet interfacial area covered by the particles. This parameter characterizes the packing density of the particles at the interface. For example, for hexagonally-closed packed monodisperse particles C is equal to 0.9. Limited coalescence only occurs for sufficiently small amounts of solid particles and equation 1 is only valid if there is no excess of particles in the continuous phase.

The design of emulsions which can evolve under the effect of an external stimulus is a real challenge. Generally, the purpose is to destabilize an emulsion "on demand", by simply modifying a variable in the system. Recently, several publications were devoted to particle-stabilized emulsions whose behavior was sensitive to various stimuli: pH, salt concentration, temperature or magnetic field [23–32]. The variation of one variable induces a sharp transition between the initially dispersed state and partial or total macroscopic phase separation. Destabilization is due to either particle desorption or modification of the interfacial behavior at the interface. In the present study, we aim at using the pH and the salt concentration as means to trigger the emulsion characteristics: drop size, interface coverage and kinetic stability. We produce pH-sensitive particles and we use them as emulsion stabilizers. We identify two stability regimes: for a given composition (same amount of oil, water and particles), it is possible to stabilize either large drops densely covered by the particles (low pH or high salt content) or more surprisingly small droplets weakly covered (high pH). At even higher pH values, phase separation occurs. We compare the relative emulsion stability in the two limiting regimes of dense or poor particle coverage.

Stimuli-responsive particles

Three types of hydrophilic particles were synthesized: organic, hybrid and mineral. When required the particles were modified in order to make them "amphiphilic" and hence to promote their adsorption at the oil-water interface.

Latex particles

Micron-sized monodisperse polymer particles with a core-shell structure were prepared through a two-step polymerization process [29, 33, 34]. First, highly cross-linked core particles were prepared through precipitation polymerization of a mixture of monomers (divinylbenzene, ethyleneglycol dimethacrylate and chloromethylstyrene). The second step consisted of the shell synthesis through an atom transfer radical polymerization of *tert*-butylacrylate. Finally, deprotection of the *tert*-butyl groups through acidolysis leaded to polymer particles with a hairy and hydrophilic polyacrylic acid (PAA) shell structure that enabled easy dispersion of the particles in water. Once fabricated, particles were filtered, washed several times with dichloromethane, ethanol and water, and then dried under vacuum. The particles were remarkably uniform in size and they were characterized by a mean diameter of 3.5μm. Because of their large size, the particles were not Brownian and tended to rapidly sediment in the water phase. The mass of the shell was estimated to represent 11% of the total particle weight. Because of the PAA functions, the particles were sensitive to pH (pKa of PAA=4.5) [35].

Silica particles

Silica particles were synthesized following the procedure described elsewhere [36–38] and then functionalized by grafting aminopropyltriethoxysilane molecules in order to make the surface pH-sensitive. The obtained particles were characterized by a statistical analysis from TEM images. Their mean diameter was estimated to be 790 ± 10 nm and their density was 2.1g.cm^{-3}. The particles were purified by centrifugation-redispersion cycles; each successive supernatant was decanted and replaced with pure water.

Neighborite cubes

$NaMgF_3$ cubes were synthesized following a procedure described elsewhere [39]. The particles were washed several times by centrifugation-redispersion in water cycles.

Electron microscopy observation showed nearly monodisperse cubes with an average edge length of 1.6μm.

Method to prepare and characterize the emulsions

Latex particles were dispersed in water at the appropriate pH and sonicated when required. The pH was adjusted by addition of small amounts of either HCl or NaOH. The salinity was then fixed independently by addition of appropriate amounts of a NaCl solution. Hexadecane-in-water emulsions were prepared in batches of 10g according to the following protocol. A mixture of 10wt% of hexadecane ($\rho = 0.77 g.cm^{-3}$, purity >99%, purchased from Aldrich and used without further purification) and 90wt% of the water (Milli-Q quality, resistivity 18.2MΩ.cm) containing the particles was manually shaken. Although simple, this method produced emulsions in a reproducible way, *i.e.* with the same final average diameter and size distribution. The same emulsion characteristics were obtained whatever the agitation intensity and duration suggesting that the final state was determined by the composition and not by the agitation.

The emulsions were characterized by their surface average diameter D and by the polydispersity P defined as:

$$D = \frac{\sum_i N_i D_i^3}{\sum_i N_i D_i^2} \quad \text{and} \quad P = \frac{1}{\overline{D}} \frac{\sum_i N_i D_i^3 \left|\overline{D} - D_i\right|}{\sum_i N_i D_i^3} \qquad (2)$$

where N_i is the total number of droplets with diameter D_i. $\overline{D}$ is the median diameter, *i.e.* the diameter for which the cumulative undersized volume fraction is equal to 50%.

These two parameters were obtained by the analysis of images taken by an inverted optical microscope (Zeiss Axiovert X100) equipped with a camera. The dimensions of at least 50 droplets were measured before calculating D and P following equations (2).

Obtained emulsions

In order to probe the sensitivity of the emulsions, different stimuli based on variations of the pH and of the, salt concentration, were investigated.

Influence of pH

The emulsions stabilized with our latexes were all of the o/w type. Emulsions were prepared with 10 mg of latex particles at pH values ranging from 1 to 14. The emulsion droplets rapidly creamed and we checked that the lower continuous phase did not contain excess particles. The final average drop size and the surface coverage C (assuming that particles arrange as a monolayer at the oil-water interface) deduced from equation (1) are reported on fig.1 as a function of pH.

This figure reveals three regimes. At low pH (<pKa), the emulsions comprise large drops characterized by a C value close to 90%. The drops were well dispersed and the emulsions were remarkably monodisperse, the polydispersity index P being smaller than 20%. The obtained values for C suggest a closely-packed monolayer arrangement of the particles at the interface, as confirmed by optical microscopy (see fig. 2a and b). For pH > pKa, the drops were much smaller, weakly covered (C around 10%) and their distribution was rather large P > 20%). Optical microscopy observations revealed a non-uniform particle distribution at the interface with large clusters and uncovered areas. Despite the low surface coverage, the emulsions were stable over months even in the creamed state where the volume fraction of oil reached approximately 64%. Interestingly, the emulsions were strongly flocculated (see fig. 2c and d). For pH>8, coalescence and macroscopic phase separation occurred quite rapidly; in this pH range, particles did not anchor anymore at the interface and remained preferentially dispersed in the continuous phase. This change of particle interfacial behavior may be linked to a conformation change of the PAA brushes from weakly swollen at low pH to fully

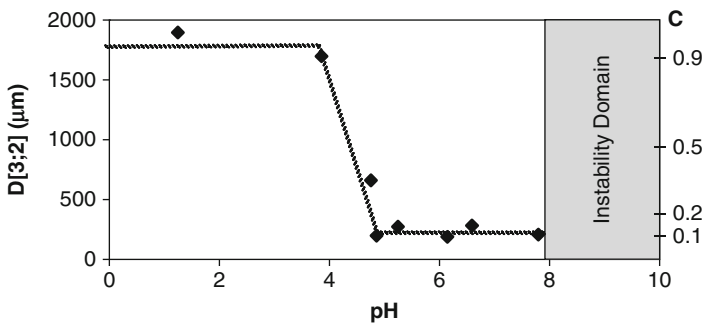

Fig. 1 Influence of pH on emulsion drop size for emulsions stabilized by latex particles. Three main domains can be observed: two stability domains (below and above pH 4.5) and an instability domain above pH 8 where rapid destabilization is observed. (adapted from Gautier *et al.* [29]).

stretched at high pH due to the increasing amount of charged groups [35].

Influence of the stabilizers amount

We explored the influence of the particle content on the final drops size for pH<8. In fig. 3, we report the evolution of 1/D as a function of particle amount in the two stability domains, at pH = 1 and 7. The inverse drop size varies linearly with the mass of particles, all the other parameters being constant, in agreement with equation (1). The surface coverage C is deduced from the slope and the obtained value is in agreement with a closely-packed arrangement of the particles ($C \approx 0.98$) in the first domain. At pH = 7, the linear dependence of 1/D *vs*. m_p suggests that a limited coalescence process is again at the origin of the final droplet size. However, coalescence has been interrupted at a very low level of particle coverage ($C \approx 0.05$).

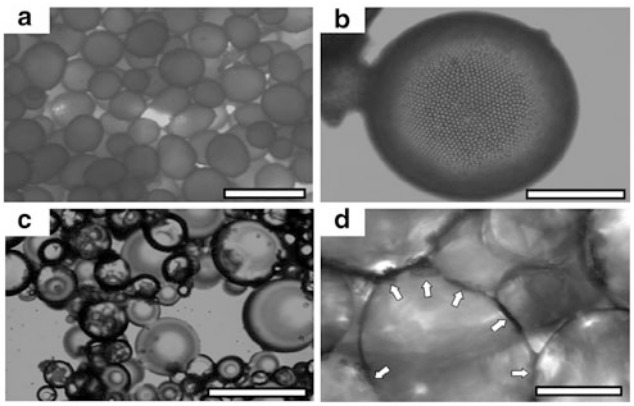

Fig. 2 a) and b) Examples of highly covered emulsions stabilized by latex particles in the first domain of pH, pH = 1, scale bars are 400 and 100 µm respectively c) Example of a poorly covered emulsion stabilized by latex particles at pH = 7, scale bar = 200µm d) Preferential location of the latex particles at the contact zones between drops, pH = 7; the white arrows show the particles location at the contact zones between drops, scale bar is 100µm. These pictures are not extracted from the experiment shown in fig. 1 but are representative of the general behavior.

Influence of salt, pH/salt cycling

In order to determine the origin of the stabilizing mechanism in the poorly covered regime, we added salt in the continuous phase. Coalescence started again and the same final droplet size and particle coverage as in acidic conditions were achieved. Thus it is likely that for pKa<pH<8 the stability has an electrostatic origin.

We checked the reversibility of the two stability regimes by cyclically modifying the aqueous phase composition (fig. 4a and b). In the case of pH cycling, we started with an emulsion at pH = 3. The lower phase after emulsion creaming was replaced by an aqueous solution at pH = 6. The system had to be re-emulsified with an energy input as the drop size decrease required new interface creation. The obtained final droplet size was the same as for the emulsion initially prepared at pH = 6 (fig. 1). The same procedure was applied to vary the pH from 6 to 3. This time no energy supply was needed for the drop size evolution. The emulsion was mildly homogenized by gentle manual inclination of the vessel many times to avoid droplet fragmentation and the drop size spontaneously increased within a few seconds.

The same kind of procedure was applied with a 0.1M NaCl brine at pH = 6, starting with an emulsion without salt (fig. 4b). The replacement of the lower phase by a salted solution was carried out several times to ensure a precise control of the salt concentration. As for pH cycling, the transition from small to larger drops occurred without external energy supply whereas the transition from large to smaller drops required intense manual shaking.

For both stimuli (pH and salt concentration), the resulting sizes were perfectly reproducible at each cycle showing that the emulsion can adopt two kinetically stable states, characterized by two different degrees of surface coverage. Such bi-stability as a function of pH and brine was also observed with different particle types such as pH-sensitive silica particles [29] or $NaMgF_3$ cubes as illustrated in fig. 5a and b.

Preferential location of particles

Stability in the low pH domain obviously results from the steric hindrance due to the dense particle monolayer.

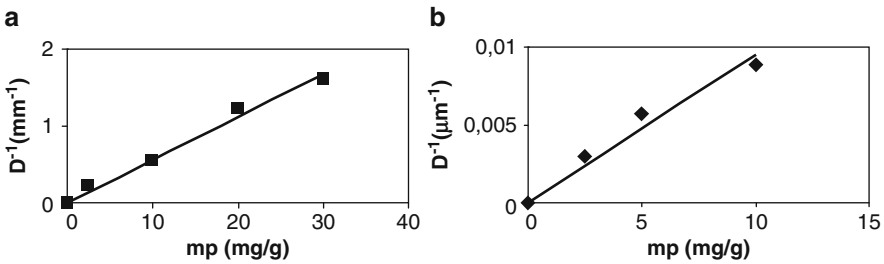

Fig. 3 Influence of the mass of latex particles (with respect to the oil mass) on the inverse drop size for emulsions stabilised at a) pH = 1 (adapted from Gautier *et al*. [29]) and b) pH = 7.

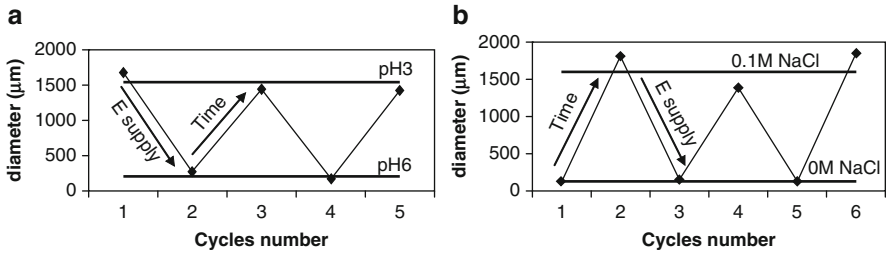

Fig. 4 Influence of a) pH and b) salt cycling on the emulsion drop size for hexadecane/water emulsions stabilized by latex particles. When the pH (salt concentration) was decreased (increased), the emulsion was quiescently stored and the size evolved spontaneously. When the pH (salt concentration) was increased (decreased) the system was re-emulsified.

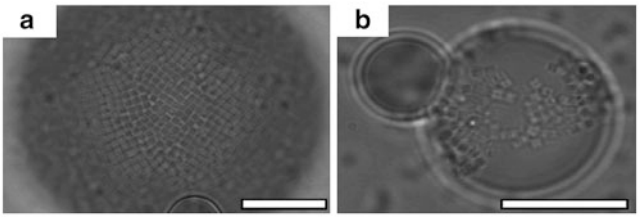

Fig. 5 Hexadecane/water emulsions stabilized by $NaMgF_3$ cubes. As it is the case for emulsions stabilized by latex or silica particles, we can also observed two kinetically stable states characterized by two different surface coverages as a function of the pH a) pH = 3 and b) pH = 6. Scale bars are 20µm.

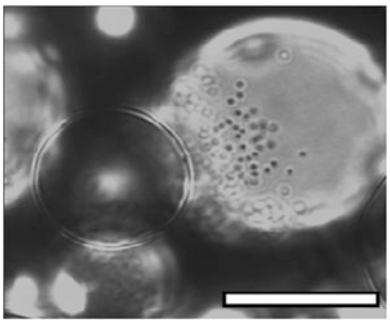

Fig. 6 Optical microscopy observation of contact regions between drops of a hexadecane/water emulsion stabilized by silica particles: all the particles are located in the drop hemisphere comprizing the contact zone, while the other hemisphere remains uncovered. Scale bar is 20µm.

However, stability of emulsions in the poorly-covered regime is intriguing. Kinetically stable Pickering emulsions with low surface coverage have already been reported by several authors. [29, 32, 40–42] In order to get insight into the stabilization mechanisms, direct observation of contact regions between emulsion droplets [40] or between model interfaces brought into contact in a controlled manner [43–47] have been performed. It was reported that the particles of both interfaces formed a dense monolayer that resisted further coalescence. In our case, the contact zones in between drops could be easily visualized by optical microscopy because of the large particle and droplet dimensions. Figure 2d reveals a preferential location of latex particles at the contact zone. The same particle arrangement was obtained in the presence of pH-sensitive silica particles (see fig. 6). In this latter case, the particles were small enough to be submitted to an intense Brownian motion at the interface. The particles tended to concentrate in the contacting hemisphere, the other one remaining completely uncovered. Such preferential location of particles was also reported by Vignati *et al.* [42] who presented evidence of "reallocation effect" of particles associated with drops closeness.

Discussion on the possible stabilizing mechanism

In a recent publication (Gautier *et al.* [29]), we proposed a mechanism based on dipole-dipole interactions between the particles adsorbed onto two neighboring interfaces, in order to explain the possible accumulation of particles at the droplet contact. The contact zone is considered as being formed by two parallel flat interfaces. A charged particle anchored at one interface between polar and non polar media produces an effective dipole because of the surface charge difference in the two different media. The interaction energy between anti-parallel dipoles anchored on two opposite interfaces depends on the angle, α, between the dipoles direction and the particles centre-to-centre line. This interaction is attractive for α larger than 54.7° with a growing intensity as α increases. So the system tends to adopt a configuration where α takes the largest accessible value (see fig. 7). This situation occurs when the particles anchored at one interface are in contact with the opposing interface and when the particle contact angle θ at the oil-water interface (defined in the introduction) is smaller than 90° which means for preferentially water-wetted particles. Such attractive interaction could explain the preferential location of the particules in the contact zones. It could thus be at the origin of the flocculated state and of the stunning kinetic stability of the emulsions in the weakly-covered regime.

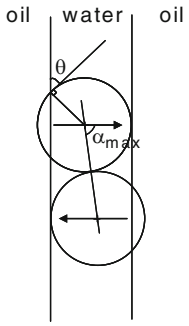

Fig. 7 Proposed stabilizing mechanism for low-covered interfaces: particles adsorbed onto neighboring interfaces behave as anti-parallel dipoles and the system tends to adopt an optimal configuration. Adapted from [29].

Conclusion

In this paper, we aimed to show general behaviors of solid-stabilized emulsions by using various types of particles as stabilizers: organic latexes, inorganic silica and mineral neighborite cubes. In the three cases, emulsions exhibited sensitivity to external stimuli: pH and salinity. Depending on the aqueous phase composition, two kinetically stable states could be observed. These latter are most probably linked to the existence of specific interparticle interactions at the interfaces whose exact nature requires further investigations. The kinetic bi-stability of such emulsions is likely linked to inter particle interactions at the interfaces that are still a field of research.

References

1. Pickering, SU (1907) J Chem Soc, Trans 91:2001-2021
2. Ramsden, W (1903) Proc. R. Soc. London 72:156
3. Binks, BP, Clint, JH, Mackenzie, G, Simcock, C, Whitby, CP (2005) Langmuir 21:8161-8167
4. Arditty, S, Schmitt, V, Giermanska-Kahn, J, Leal-Calderon, F (2004) J Colloid Interface Sci 275:659-664
5. Arditty, S, Schmitt, V, Lequeux, F, Leal-Calderon, F (2005) Eur Phys J B 44:381-393
6. Bon, SAF, Mookhoek, SD, Colver, PJ, Fischer, HR, van der Zwaag, S (2007) Eur Polym J 43:4839-4842
7. Ao, Z, Yang, Z, Wang, J, Zhang, G, Ngai, T (2009) Langmuir 25:2572-2574
8. Cauvin, S, Colver, PJ, Bon, SAF (2005) Macromolecules 38:7887-7889
9. Chen, T, Colver, PJ, Bon, SAF (2007) Adv Mater 19:2286-2289
10. Colver, PJ, Bon, SAF (2007) Chem Mater 19:1537-1539
11. Colver, PJ, Colard, CAL, Bon, SAF (2008) J Am Chem Soc 130:16850-16851
12. Destribats, M, Schmitt, V, Backov, R (2009) Langmuir DOI:10.1021/la902828q:
13. Dinsmore, AD, Hsu, MF, Nikolaides, MG, Marquez, M, Bausch, AR, Weitz, DA (2002) Science 298:1006-1009
14. Jiang, S, Granick, S (2008) Langmuir 24:2438-2445
15. Perro, A, Meunier, F, Schmitt, V, Ravaine, S (2009) Colloids Surf A 332:57-62
16. Schmitt, V, Destribats, M, Backov, R (2009) French Patent FR0955417
17. Velev, OD, Furusawa, K, Nagayama, K (1996) Langmuir 12:2374-2384
18. Aveyard, R, Binks, BP, Clint, JH (2003) Adv Colloid Interface Sci 100–102:503-546
19. Binks, BP (2002) Curr Opin Colloid Interface Sci 7:21-41
20. Leal-Calderon, F, Schmitt, V (2008) Curr Opin Colloid Interface Sci 13:217-227
21. Finkle, P, Draper, HD, Hildebrand, JH (1923) J Am Chem Soc 45:2780-2788
22. Arditty, S, Whitby, CP, Binks, BP, Schmitt, V, Leal-Calderon, F (2003) Eur Phys J E 11:273-281
23. Binks, BP, Murakami, R, Armes, SP, Fujii, S (2005) Angew Chem Int Ed 44:4795-4798
24. Binks, BP, Rodrigues, JA (2005) Angew Chem Int Ed 44:441-444
25. Brugger, B, Richtering, W (2008) Langmuir 24:7769-7777
26. Fujii, S, Cai, Y, Weaver, JVM, Armes, SP (2005) J Am Chem Soc 127:7304-7305
27. Fujii, S, Randall, DP, Armes, SP (2004) Langmuir 20:11329-11335
28. Fujii, S, Read, ES, Binks, BP, Armes, SP (2005) Adv Mater 17:1014-1018
29. Gautier, F, Destribats, M, Perrier-Cornet, R, Dechézelles, JF, Giermanska, J, Héroguez, V, Ravaine, S, Leal-Calderon, F, Schmitt, V (2007) Phys Chem Chem Phys 9:6455-6462
30. Li, J, Stöver, HDH (2008) Langmuir 24:13237-13240
31. Melle, S, Lask, M, Fuller, GG (2005) Langmuir 21:2158-2162
32. Ngai, T, Auweter, H, Behrens, SH (2006) Macromolecules 39:8171-8177
33. Downey, JS, Frank, RS, Li, WH, Stöver, HDH (1999) Macromolecules 32:2838-2844
34. Wen-Hui, L, Kai, L, Harald, DHS (1999) J Polym Sci, Part A: Polym Chem 37:2295-2303
35. Dong, R, Lindau, M, Ober, CK (2009) Langmuir 25:4774-4779
36. Reculusa, S, Ravaine, S (2003) Chem Mater 15:598-605
37. Reculusa, S, Ravaine, S (2005) Appl Surf Sci 246:409-414
38. Stöber, W, Fink, A, Bohn, E (1968) J Colloid Interface Sci 26:62-69
39. Hsu, WP, Zhong, Q, Matijevic, E (1996) J Colloid Interface Sci 181:142-148
40. Horozov, TS, Binks, BP (2006) Angew Chem Int Ed 45:773-776
41. Tarimala, S, Dai, LL (2004) Langmuir 20:3492-3494
42. Vignati, E, Piazza, R, Lockhart, TP (2003) Langmuir 19:6650-6656
43. Ashby, NP, Binks, BP, Paunov, VN (2004) Chem Commun 10:436-437
44. Horozov, TS, Aveyard, R, Clint, JH, Neumann, B (2005) Langmuir 21:2330-2341
45. Stancik, EJ, Fuller, GG (2004) Langmuir 20:4805-4808
46. Stancik, EJ, Kouhkan, M, Fuller, GG (2004) Langmuir 20:90-94
47. Xu, H, Lask, M, Kirkwood, J, Fuller, G (2007) Langmuir 23:4837-4841

Progr Colloid Polym Sci (2010) 137:19–22
DOI: 10.1007/978-3-642-13461-6_5

pH- and Thermo-responsive Polymer Assemblies in Aqueous Solution

Elodie Siband, Yvette Tran and Dominique Hourdet

Abstract Responsive polymers were prepared by copolymerizing a small amount of ionizable monomers, acrylic acid or N,N-dimethylaminopropylmethacrylamide, with N-isopropylacrylamide (NIPA) and the solubility in aqueous solution of these PNIPA derivatives were quantitatively studied. From differential scanning calorimetry experiments, it was shown that the pH strongly influences the phase separation of these copolymers (temperature and enthalpy), which totally disappears when ionizable groups are fully charged. At pH 7, all PNIPA copolymers remain soluble in water at all temperatures but their mixtures show a phase separation above a critical temperature due to the formation of a reversible inter-polyelectrolyte complex. When the responsive stickers are grafted on a poly(acrylamide) backbone, pH and temperature are still able to drive the association process at a local scale, giving rise to a sol/gel transition of semi-dilute solutions. The structure and the viscoelastic properties of these macromolecular assemblies are investigated by small angle neutron scattering and rheology and their responsivity is discussed as a function of pH and temperature.

Keywords responsive polymers • associating polymers • pnipa

Introduction

Responsive macromolecules have attracted considerable attention during the last 20 years due to their high potentiality in tailoring smart materials and complex formulations. Among these polymers, poly(N-isopropylacrylamide) (PNIPA), which phase separates in aqueous media above its Lower Critical Solution Temperature (LCST) close to the body temperature, is certainly the most popular one with a large number of scientific papers dedicated to theoretical aspects of the phase transition (thermodynamics and kinetics) and potential applications in the field of mechanical transducers (artificial muscles), microfluidics or drug delivery systems {1-6}. While the solubility of PNIPA in water strongly depends on environmental conditions, such as pressure, salt, co-solvent, surfactants... its properties can be finely tuned by the chemical composition of the polymer chain. For instance, the solubility of PNIPA in water can be easily reduced or enhanced by introducing hydrophobic or hydrophilic (or ionic) comonomers, respectively. Moreover, the introduction of ionizable groups (acid or base) gives rise to a strong coupling between pH and temperature and highly enhances the responsiveness of these macromolecular structures {7-8}. This set of interactions, which has been mainly used to control the swelling behavior of covalent hydrogels {1,9,10}, is considered in the present study to trigger pH- and/or thermo-responsive associations at a local scale in order to drive a macroscopic sol/gel transition. Moreover, one of the main goals of this work is also to point out the possibility to design thermoresponsive inter-polyelectrolyte complex by coupling electrostatic attractions, taking place between oppositely charged monomers, with the temperature sensitivity of NIPA units. This original behavior is discussed in the framework of the relation structure/properties of macromolecular assemblies.

Material and Methods

Synthesis. Responsive copolymers were obtained by telomerization of *N*-isopropylacrylamide (NIPA) with acrylic acid (A), or N,N-dimethylaminopropylmethacrylamide (M), in the presence of cysteamine hydrochloride as telogen and potassium peroxodisulfate as initiator. The two cotelomers, PNIPA-A and PNIPA-M, were characterized by SEC,

E. Siband (✉)
Physico-chimie des Polymères et des Milieux Dispersés (UMR 7615 UPMC-CNRS-ESPCI), 10 rue Vauquelin, 75005 Paris – France
e-mail: elodie.siband@espci.fr

©Springer-Verlag Berlin Heidelberg 2010

^{1}H NMR and acid/base titration. They have the same molar content of ionizable groups (10 mol%) and a number average molecular weight of about 18 kg/mol with a dispersity of molar masses lower than 1.5. After peptide coupling between the amino-terminated PNIPA-A and acrylic acid, the resulting macromonomer was copolymerized with acrylamide in water using a redox initiator. The obtained graft copolymer, PAM-g-PNIPA-A, is characterized by a number average molar mass $M_n = 400$ kg/mol and a weight fraction of 34 wt% of PNIPA-A, as determined by SEC and ^{1}H NMR. The different steps of the synthesis have been described elsewhere {11}.

DSC. Differential scanning calorimetry experiments were performed with a microDSCIII (Setaram), using a heating/cooling rate of 1°C/min (0.8 g sample).

Rheology. The viscoelastic properties of copolymer solutions and their temperature dependence were studied with a controlled stress rheometer (Haake RS150) using a cone/plate geometry. The temperature was adjusted by a high power Peltier system that provided fast and precise control of the temperature during heating and cooling stages (2°C/min). All the experiments were performed at a constant frequency: $f = 1$ Hz.

SANS. Small angle neutron scattering experiments were performed on polymer solutions prepared in D_2O at Laboratoire Léon Brillouin (Saclay - France) on spectrometer PACE (λ = 12 Å; D = 4.7m). Following the usual data treatment procedure (see reference {11}), the absolute intensities I(q) were obtained and plotted versus the scattering vector q.

Results and Discussion

Phase behavior of PNIPA telomers

The solubility of PNIPA in aqueous media is known to be temperature dependent and the dehydration phenomenon that occurs upon heating is an endothermic process that can be followed by DSC. A typical thermogram is given in **Figure 1a** for a PNIPA-A solution at pH 3 ($C_P = 1$ wt%). At low pH, when acrylic acid units are uncharged, the coil-globule transition of PNIPA-A (ΔH = 4.5 kJ per mol of NIPA) and the overall association process starts at T_{ass} = 34°C in good agreement with enthalpies and temperatures reported in the literature {12–13}. This temperature typically corresponds to the cloud point of the solution. In order to facilitate the analysis of the whole phase separation process, the cumulated transition enthalpy (ΔH in kJ per mol of NIPA) has been calculated by integrating the endotherms (**Figure 1**). This representation clearly displays the strong

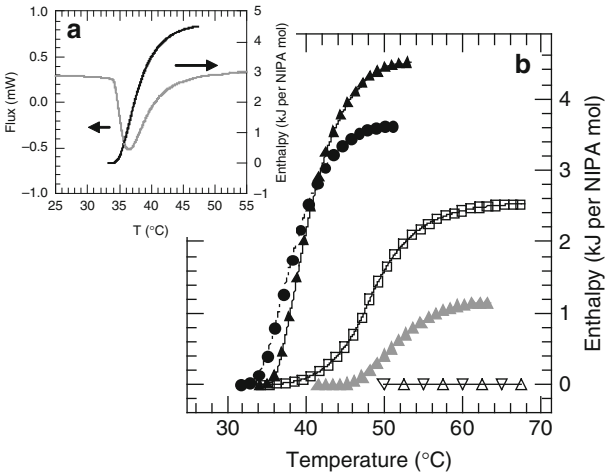

Fig. 1 a) Thermogram and b) transition enthalpy of aqueous solutions of PNIPA derivatives :PNIPA-A ($C_P = 1$ wt%) / pH = 3 ▲; pH = 5 ▲; pH = 7 △ PNIPA-M ($C_P = 1$ wt%) / pH = 7 ▽ PNIPA-A + PNIPA-M (C_P = 1+1 wt%) / pH = 7 □ PAM-g-PNIPA-A ($C_P = 2$ wt%) / pH = 3 ●.

impact of pH and ionic charges on the phase separation process. As a matter of fact, the transition enthalpy progressively decreases with increasing pH (or increasing degree of ionisation) while the beginning of the association (T_{ass}) is progressively shifted towards higher temperatures. At pH 7, when all carboxylic groups are charged, the polymer chain no longer phase separate and the solution remains homogeneous in the whole range of temperature investigated. The same holds for PNIPA-M at pH 7, when all the tertiary amines are protonated; a phase separation being observed under non ionic form at higher pH. The interesting feature is that while each copolymer, PNIPA-A and PNIPA-M, are individually soluble at pH 7 at all temperatures, their stoichiometric mixture clearly displays a LCST type behavior that corresponds to the formation of an inter-polyelectrolyte complex (IPC) between carboxylate and ammonium groups. Due to the low content of ionizable groups in PNIPA chains, the IPC cannot be formed at low temperature but only at higher temperature with the dehydration of NIPA units.

Structure and viscoelastic properties of polymer assemblies

When PNIPA-A are covalently grafted as side chains on the PAM backbone, the phase transition with temperature is almost the same (**Figure 1b**) except that the phase separation of PNIPA-A side-chains is now confined at a local scale. At pH 3 for instance, a semi-dilute solution of PAM-g-PNIPA-A remains optically clear even at 60°C, while the transition is readily observed by DSC. Neutron scattering is in that case

one the most suitable methods to investigate the structure of self-assemblies at the nanoscale. SANS spectra are given in **Figure 2a** for PAM-g-PNIPA-A solutions ($C_p = 8$ wt%) at various pH and at high temperature (T = 60°C). Whereas the solution does not show any structure at pH 7, with a very flat scattering intensity in the whole q range, the scattering curves clearly display the formation of organised assemblies at lower pH with a correlation peak which maximum increases with decreasing ionization. In order to get quantitative information from SANS data, we first consider that above their critical temperature, PNIPA-A side-chains self-assemble into dry spherical polydisperse micelles. These micelles are embedded in a sea of PAM chains that make bridges and loops around the cores (**Figure 2b**) and their form factor can be described by:

$$F(q) = \int_{R-5\sigma}^{R+5\sigma} f(q,r)\omega(r)\mathrm{d}r$$

where $f(q,r)$ is the form factor of a sphere of radius r and $\omega(r)$ the Gaussian size distribution given with R the average radius of the micelles and σ the standard deviation.

Secondly, we assume that micellar aggregates repulse each other with a hard sphere potential of radius R_{HS} (**Figure 2b**). The structure factor for hard spheres is given by the following expression based on the Percus-Yevick approach:

$$S(q) = \left[1 + \frac{24\phi_{\mathrm{HS}} G(2qR_{HS})}{2qR_{HS}}\right]^{-1}$$

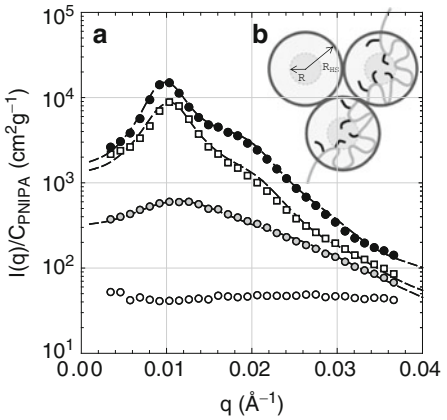

Fig. 2 **a)** Normalized scattering intensity of PAM-g-PNIPA-A solutions at T = 60°C in various environment: • ($C_P = 8.4$ wt% / pH = 3), • ($C_P = 8.4$ wt% / pH = 5), ○ ($C_P = 8.4$ wt% / pH = 7) □ ($C_P = 8.4$ wt% + $C_{PNIPA\text{-}M} = 3.3$ wt% / pH = 7). The model that best fit the experimental data are represented by dashed lines. **b)** Micellar model: schematic representation of graft copolymer assemblies at high temperature with R the radius of PNIPA-A micelles and R_{HS} the radius of hard sphere repulsions between micelles.

where $G(2qR_{HS})$ is a trigonometric function depending on q, R_{HS} and ϕ_{HS}, the volume fraction of hard spheres (see reference {14} for further details).

Finally, the absolute scattering intensity of PNIPA-A micelles embedded in a continuous medium of PAM solution, can be expressed by the following equation:

$$I(q) = [N_m](\Delta\rho)^2 F(q)S(q)$$

where $[N_m]$ is the concentration of micelles, which is directly related to ϕ_{HS} and indirectly to the aggregation number (N_{ag}) and $\Delta\rho$ is the contrast of scattering length density.

Taking into account the experimental data (polymer concentration and PNIPA volume fraction in the copolymer), the best fit of scattering curves corresponds to a single analytical solution for R, R_{HS} and f_G, the fraction of PNIPA side-chains which are embedded into the micelles (the polydispersity being not critical). This model applied to SANS data in **Figure 2** emphasizes that the increase of ionic repulsions between PNIPA-A side-chains leads to a strong weakening of the association process with the formation of smaller aggregates (from R = 129Å and $N_{ag} = 310$ at pH 3 to R = 75Å and $N_{ag} = 60$ at pH 5) and decreasing amounts of responsive side-chains embedded into these domains (from 75 % at pH 3 to 15 % at pH 5). This result is also in good agreement with the decrease of enthalpy already observed with PNIPA-A in similar pH conditions (see **Figure 1**). While the graft copolymer is not able to self-assemble at 60°C and pH 7, it should be noticed that the introduction of a stoichiometric amount of oppositely charged PNIPA-M can trigger the formation of PNIPA microdomains in a very similar way to the one described at pH 3. In these conditions, PNIPA-A side-chains and free PNIPA-M chains readily form mixed aggregates able to drive the formation of a thermoresponsive network.

In **Figure 3**, the complex viscosity of polymer formulations prepared at different pH, is plotted as a function of temperature. At Cp = 8 wt%, the polymer solutions are well beyond the overlap concentration and in this semi-dilute regime, the interchain assembling between PNIPA stickers can lead to the formation of a transient network. This is the case at pH 3 where a strong increase of viscosity is observed between 30 and 40°C, in relation with the formation of the associating network (sol/gel transition). Above 40°C, physical crosslinks are formed and the gentle rise of viscosity is mainly attributed to an increase of the life-time of the associations with temperature. This behavior, which has been well described with homoPNIPA stickers {13}, is here strongly pH-dependent. As expected from the behavior of PNIPA-A precursor, the temperature of association as well as the complex viscosity, which is related to the connectivity of the transient network, are strongly impacted by the degree of ionization. At 60°C, the viscosity falls over 3 decades

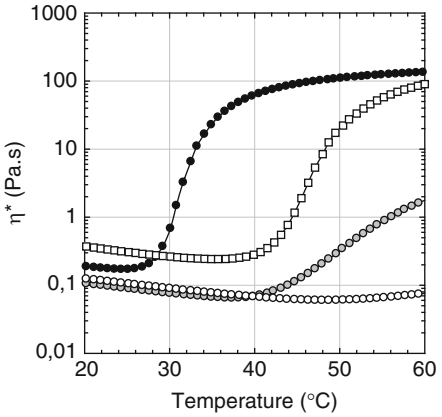

Fig. 3 Temperature dependence of the complex viscosity (η*) of PAM-g-PNIPA-A solutions ($C_P = 8$ wt%) at various conditions: • pH = 3, • pH = 5, ○ pH = 7□ pH = 7 + PNIPA-M (2.7 wt%).

between pH 3 and pH 7, but the addition of a stoichiometric amount of PNIPA-M (relative to PNIPA-A side-chains) restores the structure and the properties of the associating network.

Conclusion

By coupling the LCST properties of PNIPA with electrostatic interactions, we have shown that it was possible to finely tune the association properties in aqueous solutions. Such behavior has been exemplified with the macroscopic phase separation of PNIPA derivatives and with the self-assembling of copolymers grafted with the same responsive side-chains. This work also contributes to demonstrate that inter-polyelectrolyte complex can be formed under temperature control. These responsive interactions between complementary chains represent a very interesting tool which could be used to develop specific binding between various entities, either in bulk or at interfaces.

Acknowledgments The authors want to thank Dr. Guylaine Ducouret (PPMD, ESPCI-Paris) for her experienced advices on performing rheological measurements on associating polymers and Dr. Annie Brûlet (LLB, CEA-Saclay) for her helpful guidance in neutron scattering experiments.

References

1. Responsive Gels: Volume Transitions, Adv. Polymer Sci., 109 and 110 (1993).
2. H.G. Schild, Prog. Polym. Sci., 17, 163 (1992).
3. Y. Osada, S. B. Ross-Murphy, cientific American, 82 (1993).
4. X. Wang, C. Wu, Macromolecules, 32, 4299 (1999).
5. R. Pelton, Adv. Colloid Interface Sci., 85, 1 (2000).
6. X.-Z. Zhang, D.-Q. Wu, C.-C. Chu, Biomaterials, 25, 3793 (2004).
7. G. H. Chen, A. S. Hoffman, Nature, 373, 49 (1995).
8. G. Bokias, V. V. Vasilevskaya, I. Iliopoulos, D. Hourdet, A. R. Khokhlov, Macromolecules, 33, 9757 (2000).
9. Y. Q. Zhang, T. Tanaka, M. Shibayama, Nature, 360, 142 (1992).
10. M. Shibayama, F. Ikkai, S. Inamoto, S. Nomura, C. C. Han, J. Chem. Phys., 105, 4358 (1996).
11. L. Petit, C. Karakasyan, N. Pantoustier, D. Hourdet, Polymer, 48, 7098 (2007).
12. H. G. Schild, D. A. Tirrell, Phys. Chem., 94, 4352 (1990).
13. L. Petit, L. Bouteiller, A. Brûlet, F. Lafuma, D. Hourdet, Langmuir, 23, 147 (2007).
14. D. Hourdet, J. Gadgil, K. Podhajecka, M. V. Badiger, A. Brûlet, P. P. Wadgaonkar, Macromolecules, 38, 8512 (2005).

Progr Colloid Polym Sci (2010) 137:23–28
DOI: 10.1007/978-3-642-13461-6_6

Nano-sized TiO_2 Synthesis in Triton X-100 Reverse Micelles

H. Banu Yener, Selin Şarkaya, and Şerife. Ş Helvacı

Abstract To synthesize nano-sized TiO_2, two different methods, namely thermal hydrolysis (TH) and reverse micelles as the nano reactors in the thermal hydrolysis method (RM-TH) were used, and their effects on the shape, crystal structure, and size of the TiO_2 particles produced were investigated. In the RM-TH method, reverse micelles prepared by Triton X-100 / Cyclohexane / Aqueous $TiCl_4$ solution was used as a template since the hydrolysis reaction took place in the aqueous core of the reverse micelle that led to a controllable synthesis of TiO_2 particles. The XRD patterns of the as-prepared TiO_2 particles produced by both methods indicated that their crystal structure was rutile. In the TH method, particles were highly agglomerated resulting in a pinecone-like structure: The pinecone-like structure contained several rods with a diameter of 50 nm which were formed by conical bundles of fine rods growing radially from the center with a diameter of 6 nm and length ranged between 400 and 1000 nm. On the other hand, more uniform sphere-like nanoclusters consisting of radially growing nanorods from the center with a diameter of 6 nm and length of 200 nm were produced in the RM-TH method due to the template feature of reverse micelles. Mechanisms of nucleation and crystal growth were proposed for both production methods.

Keywords TiO_2 • Thermal hydrolysis • Reverse micelles • Rutile • Polyethylene glycol tert-octylphenyl ether (Triton X-100) • Growth mechanism

Ş.Ş Helvacı (✉) and H.B. Yener
Ege University, Faculty of Engineering, Chemical Engineering Department 35100 Bornova Izmir, Turkey
e-mail: serife.helvaci@ege.edu.tr, huriye.banu.yener@ege.edu.tr

Introduction

Syntheses of nano-sized metal oxides still need to be elucidated because of the difficulties in the control of their size, morphology, and crystal structure. The unique physical, chemical and optical properties of the nano particles depend on production methods and reaction conditions during synthesis. Since the variations in the properties of the nano particles highly affect their performance in the application fields, several production methods and reaction conditions were investigated to synthesize particles with the desired properties. TiO_2 nano particles with effective optoelectronic, electronic and catalytic properties have been widely used as pigments for paints, filler of plastics and papers [1], sensing materials [2], photocatalyst for environmental purifications [3], for the reduction of CO_2 [4-5], photovoltaic cells [6], antireflection [7], self-cleaning [8], and antibacterial-coatings [9].

TiO_2 particles can be produced by gas phase (chloride method, chemical vapor condensation and laser pyrolysis) [10], liquid phase (sol-gel, microemulsions, hydrothermal synthesis and TH) [10-14], template based [15], and solid-liquid phase (anodic oxidation of titania flakes) [16] methods. All of the methods require different reaction conditions such as high temperature, special equipment or vigorous stirring, and result in the formation of particles that are highly agglomerated, in different shapes, size and crystal structure or amorphous. In this study, on the basis of these conditions and results mentioned, a new method was developed by using reverse micelles as nano reactors in the TH method so as to be able to synthesize TiO_2 nano particles with a specific size, shape, and physicochemical properties. Effectiveness of the new method on the production of TiO_2 nano particles with desired properties was elucidated by comparing TiO_2 nano particles synthesized by both methods. Possible formation and growth mechanisms based on the experimental results were proposed for both TH and RM-TH production methods.

© Springer-Verlag Berlin Heidelberg 2010

Experimental

Materials

Titanium tetrachloride ($TiCl_4$, > 99%, Merck), hydrochloric acid (38 wt% HCl, J. T. Baker), non-ionic surfactant-polyethylene glycol tert-octylphenyl ether (Triton X-100, n =9-10, for molecular biology, Merck), and cyclohexane (> 99.5%, Merck) were used without further purifications, and double distilled water was used in all experiments.

Phase Diagram

The partial phase diagram of the ternary system of Triton X-100 / Cyclohexane / Aqueous $TiCl_4$ solution was performed at 25°C to determine the transparent region of the reverse micelles. Reverse micelles were prepared by dissolving Triton X-100 in cyclohexane in different weight ratios. Aqueous solution of reactants was prepared by dissolving $TiCl_4$ in a 3M aqueous HCl solution under magnetic stirring. Then, the aqueous solution of the reactant was added drop by drop to the reverse micelle solution with continuous stirring. The changes in the optically clear appearances and in the viscosities of the reverse micelles with the addition of the aqueous solution of the reactant were used as an indication of the phase transition from reverse micelles to another phase. Thus, the maximum amount of aqueous $TiCl_4$ solution loaded was determined by visual observation of the transparency and apparent viscosity of the reverse micelle system. The size distribution of the reverse micelles before and after the loading of the aqueous solution of the reactant was measured by dynamic light scattering.

Synthesis of TiO_2 Nanoparticles

Nano sized TiO_2 particles were prepared using two different methods, TH and RH-TH. Although there was no template in the TH method, the reverse micelles formed in the cyclohexane was loaded by the aqueous solution of reactant and used as a template in the RM-TH method.

Thermal Hydrolysis Method (TH)

In the TH method, TiO_2 nano particles were synthesized by the hydrolysis of $TiCl_4$ at 95°C and normal atmospheric pressure under reflux and at a constant stirring rate. The 0.5 M $TiCl_4$ dissolved in 3 M aqueous HCl solution was used as the reactant with a molar ratio of $TiCl_4 : H_2O = 1 : 100$. After a reaction period of 3 h, white precipitate was separated from the supernatant, rinsed with distilled water several times to remove the impurities from the surface of the particles and then dried at 60°C for further analysis.

Reverse Micelles- Thermal Hydrolysis Method (RE -TH)

The synthesis of TiO_2 particles was conducted in Triton X-100 reverse micelles formed in cyclohexane with a Triton X-100 weight percent of 50%. The aqueous solution of $TiCl_4$ at the same concentration as in the case of the TH method was loaded into the Triton X-100 reverse micelles by considering the transparency of the reverse micelles determined in the phase diagram studies. The reaction was performed in the reverse micelles at 95°C and a normal atmospheric pressure under reflux and at a constant stirring rate. The reaction conditions were kept constant throughout the reaction period of 3 h. At the end of the reaction, a stable colloidal suspension was formed and water was added to the suspension to settle the synthesized particles by withdrawing the surfactant molecules from the surface of the particles. The settled particles were then separated and washed with distilled water repeatedly to remove the surfactant molecules completely. The resultant particles were dried at 60°C for characterization.

Characterization Methods

The size distribution of the reverse micelles loaded by the aqueous solution of reactant was measured by the Dynamic Light Scattering Method using the Zetasizer Nano S (DLS, Malvern, equipped with a He-Ne laser and fixed angle 173°) before and after the reaction. The crystal structure was identified by X-ray powder diffraction (XRD, Philips X'pert Pro-45W, 40mA with CuKα radiation $\lambda = 0.1541$ nm) and the size of the primary particles were estimated from the XRD data by using the Debye-Sherrer equation. The morphologies of the products were determined by Scanning electron microscope (SEM, Philips (FEI), XL30-SFEG).

Results and Discussion

The reactant $TiCl_4$ quickly hydrolyzes in water or air at normal conditions and results in the formation of orthotitanic acid ($Ti(OH)_4$). However, in the presence of acid the hydrolysis reaction slows down, $Ti(OH)_3^+$ ions are formed and

formation of the TiO_2 particles in a definite crystal structure is favored. Due to this feature of the reactant $TiCl_4$, an aqueous $TiCl_4$ solution was prepared in an aqueous HCl solution instead of H_2O to decrease the rate of reaction of the hydrolysis in this study.

Previous studies conducted for the particle production by TH indicated that this method provides production of nano particles with a definite crystal structure without any calcination process [17-19]. However, the particles synthesized by the TH method were highly agglomerated due to the absence of the surfactants that hinder the agglomeration of the particles in the reaction medium. In order to eliminate this unfavorable part of the method, reverse micelles, in which the reaction takes place in the aqueous core of the reverse micelles surrounded by surfactant molecules, is generally used to prevent agglomeration of the particles. On the other hand, particles produced in reverse micelles at 25°C are amorphous in both shape and crystal structure and need calcination at high temperatures to improve the shape and crystal structure of the particles. Calcination at high temperatures results in agglomeration of the particles which is an undesirable situation. To produce TiO_2 nano particles with a specific crystal structure and homogeneous size distribution without calcination, a new synthesis technique was developed by using the beneficial parts of TH and reverse micelles.

In the RM-TH method, since the reaction took place in the reverse micelles, a proper ternary system that would be used as a nano reactor was selected by performing phase diagram studies and dynamic light scattering measurements. Results of the partial phase diagram study of the ternary system of Triton X-100 / Cyclohexane / Aqueous $TiCl_4$ solution is given in Fig. 1 in which the area under the dots represents the single phase (reverse micelle) region. The point marked by A on the phase diagram in Fig. 1 was selected as the nano reactor system by considering the stability and aqueous reactant solution loading capacities of the reverse micelles as criterion. The weight ratio of the Triton X-100 in the selected ternary system was 48 % with a mean reverse micelle size of 13 nm from the dynamic light scattering measurements after the loading of the reactant solution. The upper regions were not mapped in the phase diagram because the reaction was conducted in the reverse micelle region.

XRD patterns of the particles produced by TH and RM-TH methods are illustrated in Fig. 2. XRD patterns of both production techniques signified characteristic peaks corresponding to (110), (101), (111), (211), (002) and (301) crystal planes, which are in good agreement with the JCPDS (No. 77-0441) analogous to rutile phase with lattice constants a = 4.601 and c = 2.964. It has been previously reported that rutile titania can grow from TiO_6 octahedra and that an increase in the acidity of the reaction medium increases the catalytic effect of acid on the phase transition and accelerates the arrangement of the octahedra through edge sharing resulting in the rutile phase [20]. As a consequence, titania particles were synthesized in a rutile crystal structure in a highly acidic reaction medium at 95°C without calcination using the two production methods. The crystalline size of the particles was calculated by the Debye-Scherrer equation using the XRD data and is listed in Table 1.

SEM images of the particles produced by the two different methods are given in Fig. 3. The products obtained by the TH method were highly agglomerated, had a heterogeneous size distribution (Fig. 3-a1) and the pinecone-like structure consisted of short aggregating nanorods (Fig. 3-a2). The

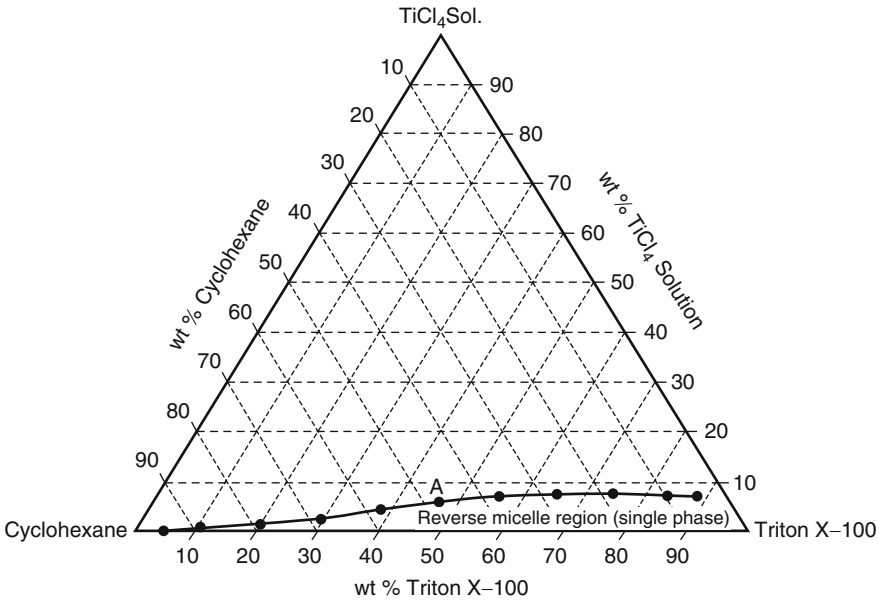

Fig. 1 The Partial phase diagram of the ternary system of Triton X-100 / Cyclohexane / Aqueous $TiCl_4$

nanorods forming the pinecone-like structure had a diameter of 6 nm and their lengths ranged between 400 nm and 1000 nm. The heterogeneously distributed nanorods formed bundles with a diameter of 50 nm. The average size of the pinecone-like structure was approximately 600 nm. SEM images of the product particles synthesized by the RM-TH method showed that the aggregates had a more homogeneous size distribution (Fig. 3-b1) and were in a flower-like structure with a mean size of 400 nm (Fig. 3-b2). The flower-like structure had nanorods that radially grow from the center. The diameter and length of the nanorods were 6 nm and 200 nm, respectively. The growth mechanism of the particles which was similar in both production methods can be clarified by the SEM images at higher magnifications given in Fig. 3-c. The particles normally looked like a sphere with a smooth surface as in Fig. 3-c1. However, higher magnifications showed that these spherical particles consists of radially growing nanorods from the center (Figs. 3-c2, c3).

Figure 4 illustrates the proposed growth mechanism of the particles produced by the two different methods. The growth process consisted of the formation of the nuclei and growth of the crystals. In both methods, after the formation of the nucleus TiO_2, Ti^{4+} ions in the reaction medium connected to the active sides of the nucleus in all directions. Due to the anisotropic growth habit of the TiO_2, the growth occurred preferentially in a radial direction. In case of the TH, since both formation of the nucleus and connection of Ti^{4+} ions took place in the aqueous bulk reactant solution, the large amount of Ti^{4+} ions in the reaction medium resulted in an asymmetrical distribution on the surface of the nucleus. In addition, the particle interactions were highly favored since there were no surfactant molecules in the reaction medium. Consequently, pinecone-like structures with a non-uniform morphology and size distribution were formed (Fig. 4-a). On the other hand, in the RM-TH method, the size of the nucleus was restricted to the size of the reverse micelles (Fig. 4-b) since hydrolysis of the $TiCl_4$ took place in the aqueous core of the reverse micelles. The exchange of the core material during agitation caused attachment of Ti^{4+} ions on the nucleus surface. The surfactant molecules that surrounded the growing crystals in all directions restricted the attachments of Ti^{4+} ions on the nucleus surface and prevented the interaction between the particles. Nevertheless, the size of the synthesized nano particles ($\sim$ 400 nm) by the RM-TH method was larger than the size of the reverse micelles (13 nm) measured by dynamic light scattering since the size of the reverse micelles was especially effective on the size of the nucleus at the nucleation stage. Thus, the particles synthesized by the RM-TH method were more uniform in morphology and size distribution.

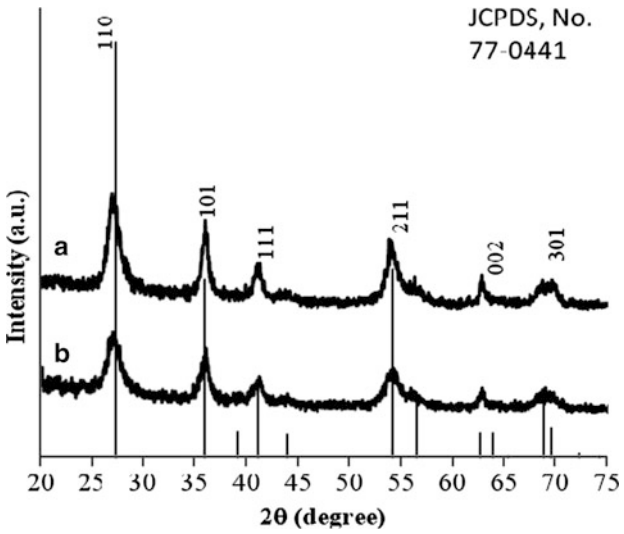

Fig. 2 The XRD patterns for particles synthesized by (a) TH, (b) RM-TH methods

Conclusion

TiO_2 nano particles in pinecone-like and flower-like structures were produced by TH and RM-TH methods, respectively. Both methods provided formation of the particles in a pure rutile crystal structure at 95°C without the calcination process. In the RM-TH method, the size of the Triton X-100 reverse micelles restricted the size of the secondary particles (aggregates) and prevented the interactions among the aggregates. Thus, the aggregates synthesized by the RM-TH method were more uniform in both shape and size distribution. On the other hand, a large number of the nucleus formed in the aqueous bulk reactant solution in the TH method resulted in the production of a lot of highly agglomerated secondary particles due to the interaction among the aggregates with heterogeneous size distribution. All of the above results indicated that the RM-TH method in which Triton X-100 reverse micelles were used as a template is the most effective in the production of particles of controlled size and

Table 1 The morphologies and crystal structures of the particles synthesized by TH and RM-TH methods

Production Method	Crystal Structure	Crystalline size (nm)*	Secondary particles				Clusters	
			Morphology	d (nm)	L (nm)	Aspect ratio (L/d)	Morphology	d (nm)
TH	Rutile	6.9	nanorod	6	400-1000	67-166	Pinecone-like	$\sim$ 600
RM-TH	Rutile	7.3	nanorod	6	200	33	Flower-like	$\sim$ 400

*Crystalline size was calculated with Debye-Scherrer equation using XRD data

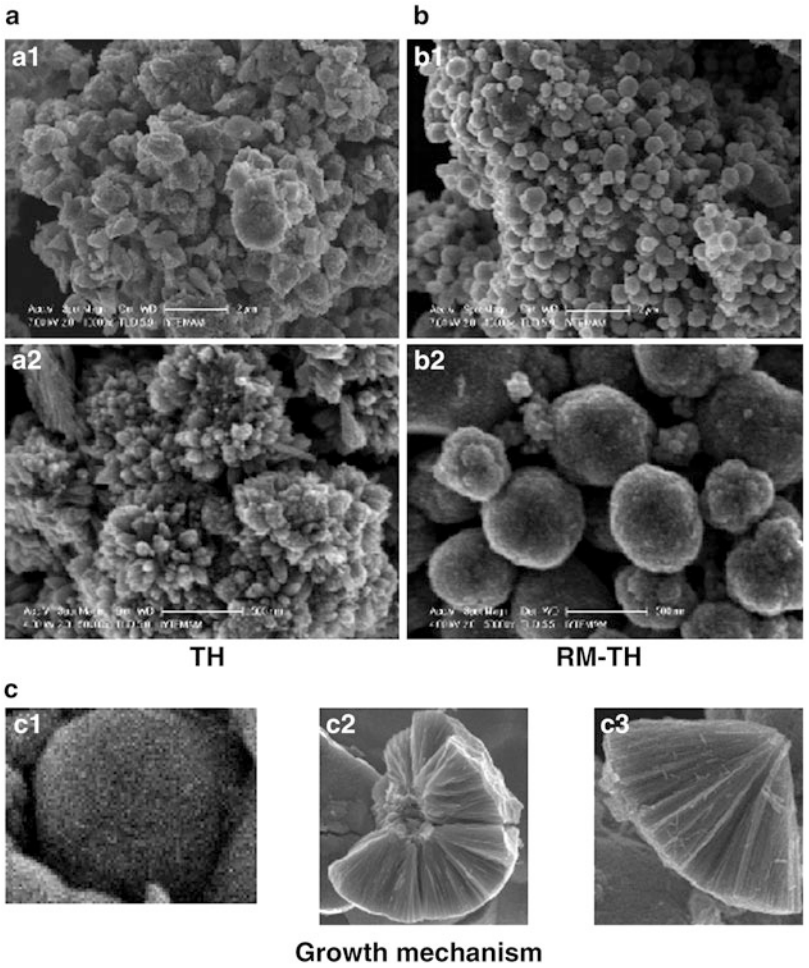

Fig. 3 SEM images of the produced particles

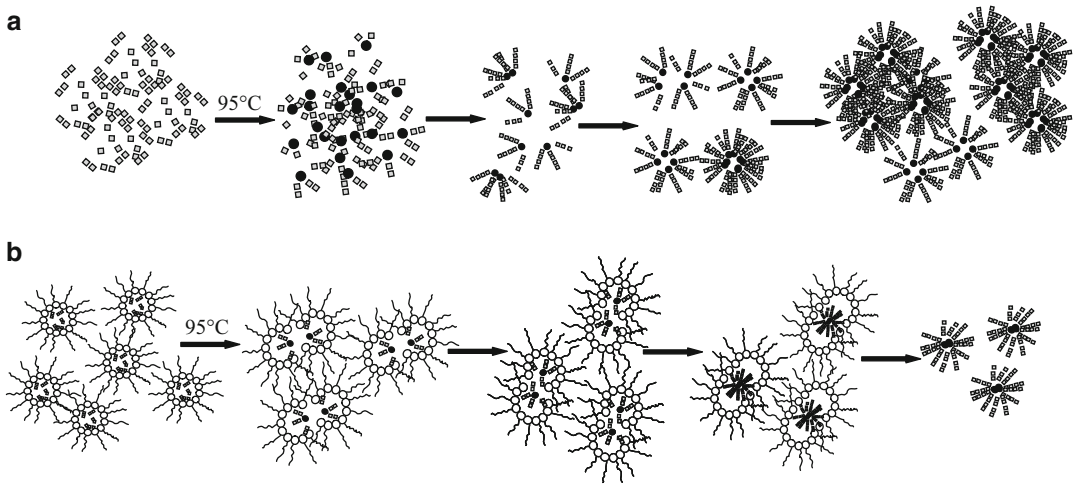

Fig. 4 The schematic diagram of the proposed growth mechanism of the particles produced by (a) TH, (b) RM-TH methods

morphology. A growth mechanism was proposed based on the experimental results and will be supported by considering the effects of the reaction conditions in future studies.

Acknowledgements This project is supported by The Scientific and Technological Research Council of Turkey (TUBITAK) through Project 104M255 and Ege University Scientific Research Foundation through Project 07-MUH-036.

References

1. Nelson K, Deng Y (2008) Journal of Colloid and Interface Science 319:130
2. Sotter E, Vilanova X, Llobet E, Vasiliev A, Correig X (2007) Sensors and Actuators B 127:567
3. Stathatos E, Tsiourvas D, Lianos P (1999) Colloids and Surfaces A: Physicochemical and Engineering Aspects 149:49
4. Liu S, Zhao Z, Wang Z (2007) Photochemical and Photobiological Sciences 6: 695
5. Wu JCS, Lin HM, Lai CL (2005) Applied Catalysis A: General 296: 194
6. Watanabe T, Hayashi H, Imai H (2006) Solar Energy Materials and Solar Cells 90:640
7. Vicente GS, Morales A, Gutierrez MT (2002) Thin Solid Films 403–404: 335
8. Allain E, Besson S, Durand C, Moreau M, Gacoin T (2007) Advanced Functional Materials 17: 549
9. Evans P, Sheel DW (2007) Surface and Coatings Technology 201: 9319
10. Tavakoli A, Sohrabi M, Kargari A (2007) Chem. Pap. 61 (3):151
11. Li X, Li T, Wu C, Zhang Z (2007) Journal of Nanoparticle Research 9 :1081
12. Deorsola F A, Vallauri D (2009) Powder Technology 190 :304
13. Lu C-H, Wen M-C (2008) Journal of Alloys and Compounds 448:153
14. Li H, Duan X, Liu G, Jia X, Liu X (2008) Materials Letters 62:4035
15. Grosso D, Boissiere C, Nicole L (2006) J. Sol-Gel Sci. Techn. 40:141
16. Zhang G, Huang H, Zhang Y, Chan HLW, Zhou L (2007) Electrochemistry Communications 9:2854
17. Helvacı ŞŞ, Yener HB, Çakır V, Şarkaya Ş (2008) 5th Chemical Engineering Conference for Collaborative Research in Eastern Mediterranean (EMCC-5) Italy
18. Li Y, Liu J, Jia Z (2006) Materials Letters 60:1753
19. Chu R, Yan J, Lian S, Wang Y, Yan F, Chen D (2004) Solid State Communications 130:789
20. Rajesh B, Sasirekha N R, Chen Y-W (2008) Material Research Bulletin 43: 682

Progr Colloid Polym Sci (2010) 137:29–33
DOI: 10.1007/978-3-642-13461-6_7

Percolation and Jamming in Random Heterogeneous Materials with Competing Length Scales

Andriy V. Kyrylyuk, Alan Wouterse, and Albert P. Philipse

Abstract Dense packings of particles of different size and shape are simulated by the mechanical contraction method (MCM). The effect of particle shape and particle size disparity on the packing density and micro-structure of two-component composite materials with competing length scales is investigated. We propose a simple analytical model to calculate the maximum packing fraction of such a mixture, which considers two co-existing random networks of large and small particles. The model predicts a non-monotonic behavior of the total packing fraction as a function of the mixture composition with the absolute maximum in packing fraction when the two sub-systems of large and small particles simultaneously jam. The mechanical contraction simulations corroborate this finding and also provide additional results for arbitrary particle size disparity. The simulated granular materials composed of frictionless spherical and rod-like particles also exhibit a non-monotonic dependence of the onset of rigidity percolation or jamming transition on the rod elongation.

Keywords Random packing • Rigidity percolation • Jamming • Composite materials • Granular mixtures

Introduction

Amorphous structures consisting of particles which have different size and shape are ubiquitous in nature and technology [1,2]. The micro-structure of many random heterogeneous materials such as granular matter, powders, fiber and carbon nanotube reinforced polymer composites, amorphous solids, and porous media is determined by the underlying percolation network of densely packed particles [1–6]. A particulate system becomes mechanically stable at the loosest stable packing, called random loose packing (RLP), that defines the onset of the rigidity percolation [1]. In the case of frictionless particles the RLP coincides with the onset of random close packing (RCP) or jamming transition, which is governed by geometry of the particles. Monodisperse frictionless spheres jam at the relatively well-defined volume fraction, often referred to as packing fraction, $\phi_{RCP} \approx 0.64$. Polydisperse and non-spherical particles show a more intriguing but less understood packing behavior. Mixing polydisperse particles introduces competing length scales in the system. Packing of non-spherical particles is qualitatively different from that of spheres due to additional rotational degrees of freedom [7–9].

Here, we study random dense packing of two-component a-thermal, granular mixtures composed of either spherical particles or spheres and rods (spherocylinders) upon isostatic compaction. The two components of these composite materials have different sizes introducing two competing length scales, which result in two co-existing networks of particles. As a result of packing of the two particulate subsystems the packing fraction is a non-monotonic function of the mixture composition, i.e. of the relative volume fraction of one component. We present a simple analytical model for random packing of differently-sized particles as well as results from the mechanical contraction method (MCM) computer simulations. The MCM simulations of rod-sphere mixtures show the effect of particle size and shape on the micro-structure and the packing density of the binary mixture. The packing density of a densely packed bed of rods and spheres has a density maximum for a specific rod aspect ratio, independently of the lateral rod dimension, i.e. its diameter.

A.V. Kyrylyuk (✉)
Van 't Hoff Laboratory for Physical and Colloid Chemistry, Debye Institute for NanoMaterials Science,
Utrecht University, Padualaan 8,
3584 CH Utrecht, The Netherlands
e-mail: a.kyrylyuk@gmail.com

© Springer-Verlag Berlin Heidelberg 2010

Simulation method: mechanical contraction

The aim of the MCM is to produce an amorphous particulate structure by making a direct simulation of rapid densification, leading to metastable, structurally arrested states rather than thermodynamically stable phases [8]. The details of the method can be found elsewhere [8–10]. In short, a dilute initial random configuration of non-overlapping particles is prepared in a cubic box with periodic boundary conditions. The size of the system is iteratively decreased by isotropic contraction and all particle positions are uniformly scaled. When particles start overlapping, the overlap is removed by moving and, if necessary, rotating the particles. The final configuration of non-overlapping particles is obtained when upon iso-static compression it is no longer possible to remove the overlap with a reasonable amount of computational effort.

Results and Discussion

A. Jamming of binary sphere mixtures

The micro-structure of binary sphere mixtures is expressed in terms of the mixture composition or the relative volume fraction of large spheres $x_l = \phi_l/\phi$, where ϕ_l is the packing fraction of large spheres and ϕ the total packing fraction. Jammed packings of small and large spherical particles of different size ratio D_l/D_s with D_l and D_s being the diameter of the large and small spheres, respectively, are shown in figure 1.

The total packing fraction ϕ vs. the mixture composition x_l is presented in figure 2. The packing fraction has a characteristic triangular profile with maximum volume fraction around $x_l \sim 0.7 - 0.75$ for a large particle size ratio, which shifts towards smaller x_l for small size disparities. The triangular profiles of the packing curves are not symmetric and steeper for the systems dominated in the larger spheres. This result is in agreement with the results of other computer simulations and experiments [11–14]. The lowest packing fraction $\phi^{RCP} = 0.633$, which is independent of the sphere

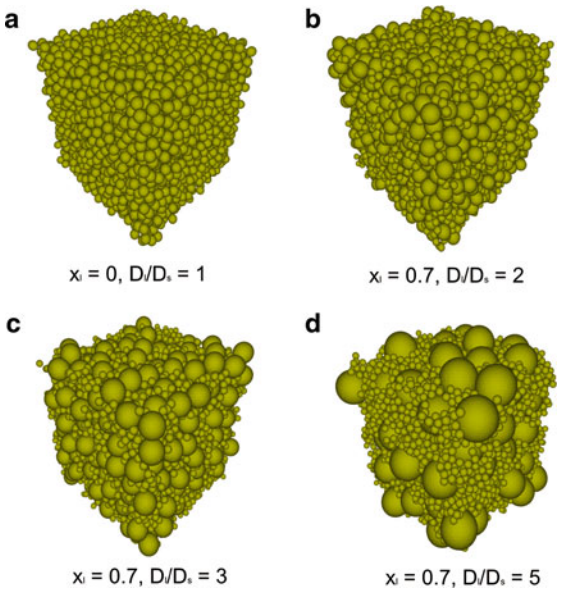

Fig. 1 Random dense packing of binary mixtures of spheres with different size ratio D_l/D_s and relative volume fraction of one component x_l

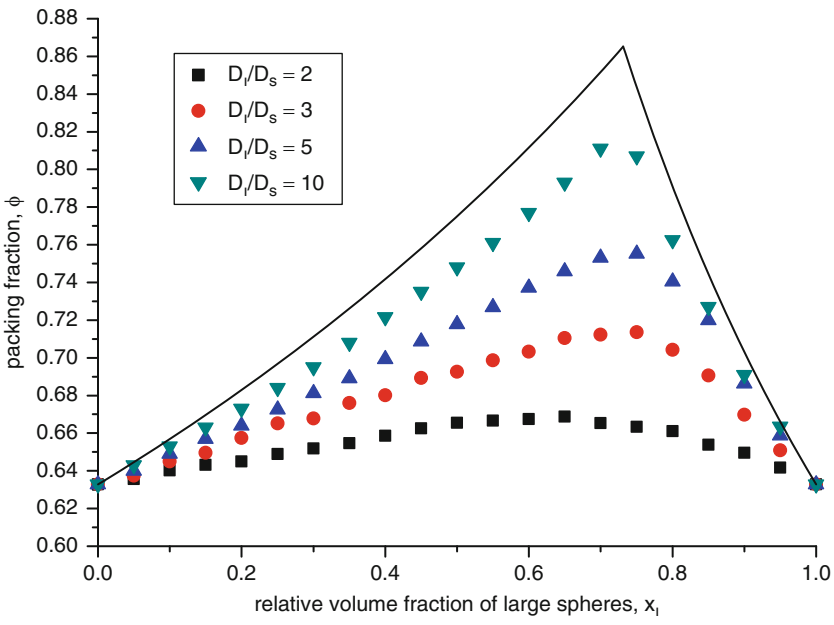

Fig. 2 The total packing fraction of binary sphere mixtures as a function of the relative volume fraction of large spheres for different size ratio of large and small spheres. The two solid lines represent the upper limit for the packing density of a binary mixture of spheres with very large size disparity, $D_l \gg D_s$, when the smaller (larger) spheres do not frustrate the jamming network of the larger (smaller) ones. The intersection of these two lines forms a cusp, which corresponds to the maximum packing density when the two sub-systems of large and small spheres jam simultaneously

size, is obtained for jammed monodisperse spheres. The non-monotonic behavior of the packing density is a result of the interplay of two competing length scales in the system.

B. A model for random packing of particles with large size disparity

In the case when one type of particle in the binary system is much larger than the other one it is easy to establish a simple model for packing of such a binary mixture. Since the particles are much different in size, the packing of each sub-system does not disturb or frustrate the packing of the other one. In other words, the length scales, which correspond to each sub-system, are so much different that they can be decoupled. The upper limit for the packing density of a binary mixture of a given composition can be found when one sub-system jams and the other one packs in the available free volume.

The total volume fraction of jammed larger particles and smaller particles that pack between the larger ones can be written as

$$\phi = \phi_l^{RCP} + \phi_s, \tag{1}$$

where ϕ_l^{RCP} is the jamming density of the large particles and ϕ_s the volume fraction occupied by the small particles. Since the relative volume fraction of large particles is $\phi_l = \phi x_l$, the total volume fraction is

$$\phi = \phi_l^{RCP}/x_l. \tag{2}$$

The total volume fraction of jammed smaller particles and loosely packed larger particles equals

$$\phi = \phi_l + (1 - \phi_l)\phi_s^{RCP}, \tag{3}$$

where ϕ_s^{RCP} is the jamming density of the small particles and ϕ_l the volume fraction occupied by the large particles. In this case the total volume fraction has the form

$$\phi = \frac{\phi_s^{RCP}}{1 - x_l(1 - \phi_s^{RCP})}. \tag{4}$$

The expressions given by eqs. (2) and (4) are plotted in figure 2. The corresponding two curves, which give the upper limit for a dense packing of a binary sphere mixture, intersect and from a cusp at

$$x_l^{\max} = \frac{1/\phi_s^{RCP}}{1/\phi_l^{RCP} + (1/\phi_s^{RCP} - 1)}, \tag{5}$$

$$\phi^{\max} = \phi_s^{RCP} + \phi_l^{RCP}(1 - \phi_s^{RCP}). \tag{6}$$

The cusp corresponds to the situation when both sub-systems jam, resulting in the absolute maximum packing density for a binary mixture. In principle, the proposed model is valid for arbitrarily shaped particles as far as the size of one component is much larger than that of the second one. For binary sphere mixtures the packing densities $\phi_l^{RCP} = \phi_s^{RCP} = \phi^{RCP} = 0.633$ so that $x_l^{\max} = 1/(2 - \phi^{RCP}) = 0.731$ and $\phi^{\max} = \phi^{RCP}(2 - \phi^{RCP}) = 0.865$.

We remark here that some theories of random packings of binary mixtures of hard spheres violate the upper bound given by eqs. (2) and (4) since they neglect the contribution of rattlers (particles having less than the four contacts) to the total packing density [15, 16]. This issue is further discussed in a forthcoming paper [17].

C. Jamming of rod-sphere mixtures

The MCM computer simulations produce dense packings of spherical and non-spherical particles that exhibit no positional or orientational ordering in the system (see figure 3). Nevertheless, the packings of aspherical particles have additional features compared to packings of spheres due to the additional rotational degrees of freedom.

The total packing fraction of a binary mixture of randomly close packed spheres and spherocylinders as a function of the rod aspect ratio for the relative volume fraction of the

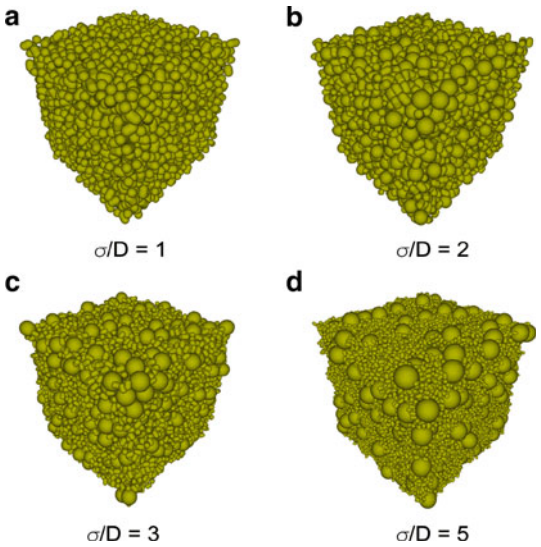

Fig. 3 Graphical rendering of several rod-sphere mixture packings for different sphere-to-rod diameter ratios, σ/D. The rod aspect ratio is $L/D = 0.5$ and the relative volume fraction of the rods (spherocylinders) $x = 0.5$

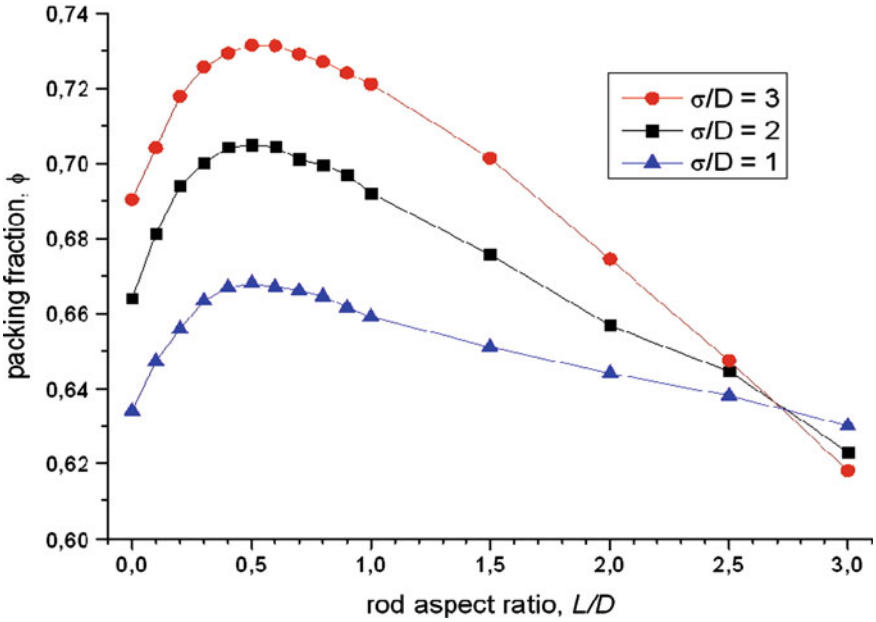

Fig. 4 The total packing fraction ϕ of a rod-sphere mixture as a function of the rod aspect ratio L/D, presented for three different sphere-to-rod diameter ratios σ/D. The relative volume fraction of the rods is $x = 0.5$

rods $x = 0.5$ is shown in figure 4. The rods and spheres have different diameters D and σ, respectively. The total packing fraction is a non-monotonic function of the rod aspect ratio L/D, where L is the length of the cylindrical part of a spherocylinder. In our previous work we already observed the appearance of the density maximum in rod-sphere mixtures consisting of the particles of the same diameter [9]. The origin of the maximum is the interplay between the size and shape effects that leads to the translation-rotation coupling.

From figure 4 we can see that the density maximum is independent of the sphere-to-rod diameter ratio and occurs at the same rod aspect ratio around $L/D = 0.5$, demonstrating a universality in packing of slightly elongated rods. The total packing fraction of spheres and nearly spherical rods ($0 < L/D < 2.7$) increases with increasing the sphere-to-rod diameter ratio, similar to the packing behavior of binary sphere mixtures. However, the trend is opposite for highly elongated rods in a mixture ($L/D > 2.7$) due to the domination of the excluded volume effect. Interestingly, all packing curves in figure 4 intersect at one point at $L/D \sim 2.7$; the corresponding packing density equals to that of monodisperse spheres, an issue that certainly requires a further investigation.

Conclusions

We have studied the random dense packing of two-component systems of particles of different size and shape. The simulated jammed packings of binary sphere mixtures exhibit a characteristic triangular profile of the packing curves with a packing density maximum, which is a result of the interplay between the two competing length scales. We predict the appearance of the cusp in the packing curve in the case of large particle size disparity. The cusp corresponds to the situation when both sub-systems of big and small particles jam, resulting in the absolute maximum packing density for a binary mixture. The binary rod-sphere mixtures show an intriguing universal packing behavior – the position of the packing density maximum, which appears due to the translation-rotation coupling, is the same for any mixture composition and sphere-to-rod diameter ratio. Also, the packing curves intersect at one universal point of the rod elongation $L/D \sim 2.7$ so that at this point all rod-sphere mixtures of different mixture compositions and sphere-to-rod diameter ratio have the same packing fraction, which equals to that of the monodisperse spheres.

Acknowledgments This work was sponsored by Senter Novem (Dutch Ministry of Economic Affairs) and Shell Global Solutions International B.V (Amsterdam, The Netherlands).

References

1. Torquato S (2002) Random Heterogeneous Materials, Springer, New York.
2. Aste T, Weaire D (2000) The Pursuit of Perfect Packing, Institute of Physics, Bristol.
3. Katz HS, Milevski JV (1978) Handbook of Fillers and Reinforcements for Plastics, Van Nostrand Reinhold, New York.
4. Kyrylyuk AV, van der Schoot P (2008) Proc Natl Acad Sci USA 105:8221.
5. Hermant MC, Klumperman B, Kyrylyuk AV, van der Schoot P, Koning CE (2009) Soft Matter 5:878.

6. Grossiord N, Kivit PJJ, Loos J, Meuldijk J, Kyrylyuk AV, van der Schoot P, Koning CE (2008) Polymer 49:2866.
7. Donev A, Cisse I, Sachs D, Variano EA, Stillinger FH, Connelly R, Torquato S, Chaikin PM (2004) Science 303:990.
8. Williams SR, Philipse AP (2003) Phys Rev E 67:051301.
9. Kyrylyuk AV, Wouterse A, Philipse AP (2009) AIP Conf Proc 1145:211.
10. Wouterse A, Williams SR, Philipse AP (2007) J Phys Condens Matter 19:406215.
11. Thies-Weesie DME, Philipse AP (1994) J Colloid Int Sci 162:470.
12. He D, Ekere NN, Cai L (1999) Phys Rev E 60:7098.
13. Yu AB, Standish N (1988) Powder Technol 55:171.
14. Farr RS, Groot RD (2009) J Chem Phys 131:244104.
15. Biazzo I, Caltagirone F, Parisi G, Zamponi F (2009) Phys Rev Lett 102:195701.
16. Clusel M, Corwin EI, Siemens AON, Brujic J (2009) Nature 460:611.
17. Biazzo I, Caltagirone F, Parisi G, Zamponi F (2010) J Chem Phys, submitted.

Progr Colloid Polym Sci (2010) 137:35–39
DOI: 10.1007/978-3-642-13461-6_8

Fabrication of Magnetic Clusters and Rods using Electrostatic Co-assembly

M. Yan, L. Chevry, and J.-F. Berret

Abstract Using a novel protocol for mixing oppositely charged colloids and macromolecules, magnetic clusters and rods are fabricated using 10 nm-iron oxide nanoparticles and polymers. Here, we show that as the dispersions undergo the so-called *desalting transition*, spherical clusters in the range 100 nm – 1 μm form spontaneously upon dialysis or dilution. With a magnetic field applied during the dialysis, a one-dimensional growth of the aggregates is initiated, resulting in the formation of 1 – 100 μm rods of average diameter 200 nm. In this paper, we demonstrate that the nanostructured rods have inherited the properties of the iron oxide particles, namely to be superparamagnetic. We also discuss the dependence of the magnetic properties as a function of the nanoparticle diameter.

Keywords Magnetic nanoparticles • Nanorods • Desalting transition • Electrostatic co-assembly

Introduction

The electrostatic complexation between oppositely charged macromolecules and colloids in aqueous solutions has attracted much attention during the last years because it is an efficient way to control the association at the nanometer scale. Since the pioneering work by Bungenberg de Jong on gelatin and arabic gum [1], the complexation has been investigated on various systems, comprising synthetic [2] and biological [3–5] polymers, multivalent counterions [6], surfactant micelles [7,8,9], organic and inorganic nanoparticles [10,7,11–13,14]. Additional control of the co-assembly process was achieved by using polyelectrolyte-neutral diblock copolymers instead of homopolyelectrolytes [15,16]. With copolymers, the complexation was monitored by the molecular weights of the two blocks and resulted in the spontaneous formation of core-shell colloids. This approach provided excellent results. It was shown to be particularly appropriate for the fabrication of cerium or iron oxide clusters in the 20 – 50 nm range [17,18]. This approach also disclosed a critical issue, that is usually not discussed in the literature. The size and morphology of the co-assemblies were found to depend on the mixing process between the initial particle and polymer dispersions [19]. In order to solve this issue, a novel mixing protocol for bringing oppositely charged species together was elaborated [20]. This protocol was inspired from molecular biology techniques developed for the *in vitro* reconstitutions of chromatin [21]. It consisted first in the screening of the electrostatic interactions by bringing the dispersions to high ionic strength (1 M of inorganic salt), and in a second step in the removal of the salt by dialysis or by dilution. In this paper, we have applied this method for the fabrication of spherical and rodlike clusters of superparamagnetic iron oxide nanoparticles. Here we focus on the effects of the desalting rate on the size of the spherical clusters. We also demonstrate that the nanostructured rods have inherited the superparamagnetic properties of the particles. The findings include four batches of nanoparticles characterized by different sizes and dispersities.

Experimental Section

The iron oxide nanoparticles were synthesized by alkaline co-precipitation of iron(II) and iron(III) salts and oxidation of the magnetite (Fe_3O_4) into maghemite (γ-Fe_2O_3) particles [22]. At the end of the process, the particles were positively charged, resulting in strong electrostatic repulsions between particles and enhanced colloidal stability. The size distribution was determined from transmission

J.-F. Berret (✉)
Matière et Systèmes Complexes, UMR 7057 CNRS Université Denis Diderot Paris-VII, Bâtiment Condorcet,
10 rue Alice Domon et Léonie Duquet, 75205 Paris, France
e-mail: jean-francois.berret@univ-paris-diderot.fr

© Springer-Verlag Berlin Heidelberg 2010

electron microscopy (TEM) measurements and could be represented by a log-normal function, with median diameter D_0 and polydispersity s. Fig. 1a displays a TEM image of the 9.3 nm particles showing a rather monodisperse population of nanocrystals and Fig. 1b illustrates the log-normal distribution, with polydispersity s = 0.18. Further characterizations of the dispersions using vibrating sample magnetometry and light scattering were performed and we refer to Refs. [23,24] for a full account of the results. In order to improve their colloidal stability in complex biological solvents [24], the cationic particles were coated by poly (acrylic acid) with molecular weight 2000 g mol^{-1} using the precipitation–redispersion process [13]. The thickness of the PAA_{2K} brush tethered on the particle surfaces was estimated at 3 ± 1 nm by dynamical light scattering. The anionically charged NPs have been co-assembled with a cationic–neutral diblock copolymers, referred to as poly (trimethylammonium ethylacrylate)-*b*-poly (acrylamide), and noted $PTEA_{11K}$-*b*-PAM_{30K} [25]. Here, the indices denote the molecular weight of the different blocks. In aqueous solutions at neutral pH, the chains were found to be disperse and in the state of unimers. Dynamic light scattering revealed an hydrodynamic diameter D_H = 11 nm and size exclusion chromatography a polydispersity index M_w/M_n = 1.6 [9].

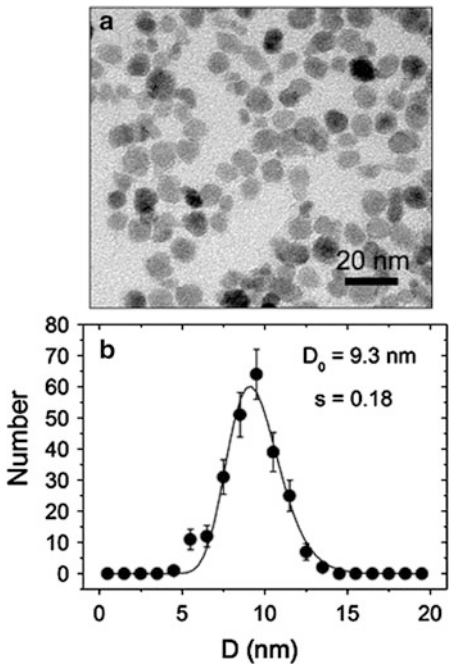

Fig. 1 (a) Iron oxide superparamagnetic nanoparticles as observed by transmission electron microscopy (TEM). (b) Size distribution derived from TEM. The continuous line resulted from best fit calculations using a log-normal distribution, with D_0 = 9.3 nm and s = 0.18. The diameter is slightly larger than that determined by magnetometry (D_0 = 8.3 nm).

Fig. 2 describes the dialysis protocol that controlled the nanoparticles co-assembly [26]. The strategy involved in a first step the preparation of two separate 1 M NH_4Cl solutions containing respectively the anionic iron oxide particles and the cationic neutral $PTEA_{11K}$-b-PAM_{30K} diblock copolymers. Typical γ-Fe_2O_3 concentrations were 0.1 wt. %, with a polymer-to-nanoparticle volume ratio of 0.5. Both solutions were then mixed with each other and in a second step, the ionic strength of the mixture was progressively diminished by dialysis or dilution. In the dilution process, deionized water was added to mixtures of PAA_{2K}-coated nanoparticles and $PTEA_{11K}$-*b*-PAM_{30K} copolymer stepwise. In this case, no magnetic field was applied. In a recent report, we demonstrate that the key parameter that controls the kinetics of formation of electrostatic clusters is the rate dI_S/dt at which the salt is removed from the solution, where I_S denotes the ionic strength. Doing so it was possible to vary dI_S/dt from 10^{-5} to 1 M s^{-1}. Dialysis was performed against deionized water using a Slide-a-Lyzer® cassette (Thermo Scientific). In these conditions, the whole process reached a stationary and final state within 50 – 100 minutes. The dialysis was carried under two different conditions, with or without magnetic field. The drawing in Fig. 2 represents the case where the magnetic field (0.1 T) was applied. As shown below, the role of the field was to induce the growth of the aggregates in one direction and to favor the formation of the rods. The dialysis experiment between the initial and final ionic strengths was characterized by an average rate of ionic strength change $dI_S/dt \sim 10^{-3}$ - 10^{-4} M s^{-1}. The aggregates

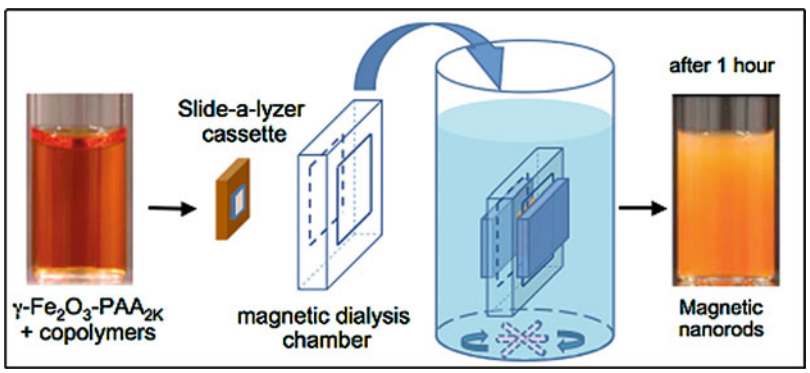

Fig. 2 Schematic representation of the protocol that controlled the nanoparticle co-assembly. Without magnetic field, co-assembly yielded spherical clusters, whereas with magnetic field of 0.1 T nanostructured rods in micron range could be fabricated.

found by dialysis or dilution were further characterized by dynamic light scattering and transmission optical microscopy, using devices described in an earlier report [20].

Results and Discussion

Desalting transition: In Ref. [19], it was found that with decreasing ionic strength, electrostatically screened dispersions of oppositely charged polymers and nanoparticles underwent an abrupt transition between an unassociated and a clustered state [19]. The transition was dubbed *desalting transition* because it occurred as the excess inorganic salt was removed from the sample. In this former work, the particles put under scrutiny were 7 nm nanoceria, and the polymers were the same $PTEA_{11K}$-*b*-PAM_{30K} as those used here. Moreover, it was shown that the critical ionic strength I_S^c (= 0.42 M) at which the desalting transition took place did not depend on the formulation conditions (such as the concentration or the mixing ratio), nor on the desalting rate dI_S/dt. In the present paper, we extended this approach to PAA_{2K}-coated iron oxide nanoparticles. In Fig. 3, the desalting transition was monitored on a broad range of desalting rates, lying between 10^{-5} and 1 M s^{-1}. There, each data point represents the hydrodynamic diameter obtained from a dispersion that underwent the desalting transition. For fast dilution ($dI_S/dt \sim 1$ M s^{-1}), the aggregates remained in the 100 nm range. Note that the D_H-values in this regime coincide well with those found by direct mixing, suggesting that in terms of kinetics of complexation, the mixing of oppositely charged species is equivalent to a quench [19]. With decreasing dI_S/dt, D_H increased and displayed an asymptotic scaling law of the form $D_H \sim dI_S/dt^{-1/3}$. A power law with exponent -1/3 is interesting because it indicates that at infinitely slow dilution, the size of the clusters would diverge, the dispersion exhibiting then a macroscopic phase separation. The inset of Fig. 3 displays a TEM image of nanoparticle aggregates obtained by dialysis. The aggregates of average diameter 180 nm were described as latex-type or composite colloids with a high load of magnetic particles. Assuming a volume fraction of 0.25 inside the large spheres [18], we have estimated that a 200 nm aggregate was built from $\sim$ 6000 particles. Such aggregates were also found to exhibit a remarkable colloidal stability, much probably due to the presence of a neutral poly(acrylamide) brush surrounding the clusters. The data in Fig. 4 are in accordance with those obtained on anionically coated nanoceria [19], showing *in fine* that this protocol can be applied to different nanoparticle systems.

Rod reorientations under 90°-flip of the magnetic field: In this part, we focus on the results of dialysis experiments performed under the application of a constant magnetic field of 0.1 T (Fig. 2). With a magnetic field applied to the dispersions, a desalting transition identical to that discussed previously for the cluster formation was observed at the critical ionic strength I_S^c = 0.42 M [20]. At the end of the dialysis, once the ionic strength in the cassette reached its equilibrium value around $I_S = 5\times10^{-3}$ M, the magnetic field was removed and the dispersion was investigated by optical transmission microscopy. Fig. 4 shows a phase-contrast image obtained with magnification ×40 of randomly oriented and elongated structures with typical sizes in the micrometer range. The γ-Fe_2O_3 batch utilized here was made from

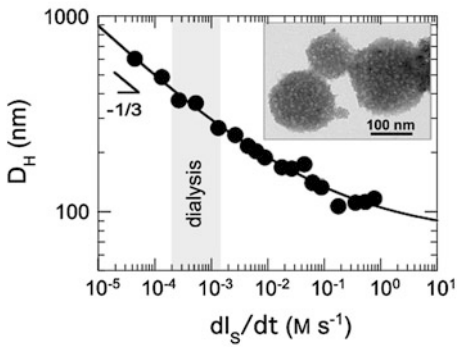

Fig. 3 Variation of the cluster hydrodynamic diameters D_H as a function of the desalting rate dI_S/dt for slow and rapid dilutions. At low dI_S/dt-values, D_H displayed an asymptotic scaling law of the form $D_H \sim (dI_S/dt)^{-1/3}$. Inset : TEM images of spherical aggregates obtained by dialysis. The diameter size of the aggregates was estimated at 180 nm.

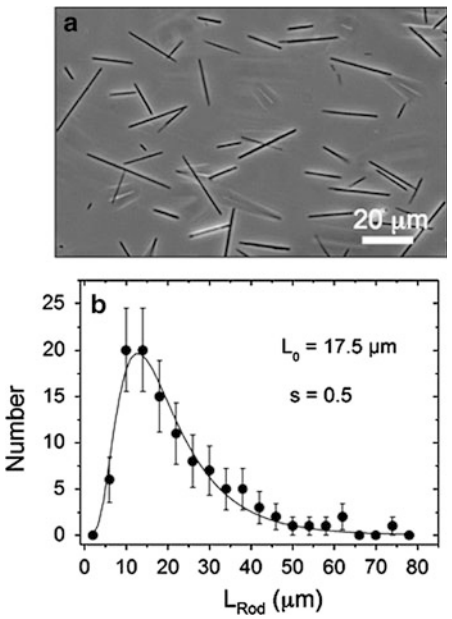

Fig. 4 (a) Phase-contrast optical microscopy images (40×) of a dispersion of nanostructured rods made from 8.3 nm γ-Fe_2O_3 particles. (b) Experimental and fitted length distribution of the rods displayed in Fig. 4a. The continuous line was obtained from best fit calculations using a log-normal distribution.

8.3 nm particles at concentration c = 0.1 wt. % and polymer-to-nanoparticle volume ratio 0.5. The structures in Fig. 4a were identified as nanostructured rods comprising scores of γ-Fe_2O_3 nanoparticles linked together by the cationic polymer "glue". Typical diameters for the rods were found around 200 nm [20]. An image analysis allowed to derive the length distribution of the rods. For this specific sample, it was found to be well accounted for by a log-normal function, with median length $L_0 = 17.5 \pm 0.9$ μm and a polydispersity s = 0.50 (Fig. 4b).

In the present work, we investigated the dependence of the magnetic properties of the rods with respect to the diameter of the particles. In a previous work [20], emphasis was put on a unique batch (diameter 7.1 nm) whereas here, particles ranging from 6.7 to 10.7 nm were studied. For that, we performed quantitative measurements of the rod kinetics associated with 90°-reorientations. In such experiments, θ(t) denotes the angle between the major axis of a rod and magnetic excitation H. At the application of the field at 90° with respect to the initial conditions, the nanorods rotated in the plane of observation around their center of gravity. The magnitude of the applied field ranged from 0 to 20 mT, *i.e.* much less than the intensity required to grow the rods (0.1 T). The reorientational dynamics resulted from the balance between the magnetic torque and the hydrodynamic drag, yielding an expression of the form [20]:

$$\mathrm{tg}\,\theta(t) = \mathrm{tg}\,\theta_0 \exp(-kt) \qquad (1)$$

In Eq. 1, θ_0 was the initial position of the rods prior to the application of the field ($\theta_0 \sim 90°$) and k the decay rate of the reorientation. k depends on the geometrical parameters of the rods, such as the length L_{Rod} and the diameter D_{Rod}, and on the strength of the applied field, as [20]:

$$k = \frac{\chi^2}{(2+\chi)} \frac{\mu_0 g(L_{Rod}/D_{Rod})}{2\eta} D_{Rod}^2 \left(\frac{H}{L_{Rod}}\right)^2 \qquad (2)$$

Here, χ denotes the magnetic susceptibility of the rods, μ_0 the permeability of vacuum, η the solvent viscosity (0.89×10^{-3} Pa s) and $g(L_{Rod}/D_{Rod})$ a slowly varying function of the aspect ratio. The quadratic H-dependence of the decay rate is a signature of the superparamagnetic character of these aggregates. Figs. 5 display the variations of k as a function of the ratio H/L_{Rod} for rods made from 4 different iron oxide batches. The particle diameters investigated were $D_0 = 6.7$ nm (Fig. 5a), $D_0 = 7.1$ nm (Fig. 5b), $D_0 = 8.3$ nm (Fig. 5c) and $D_0 = 10.7$ nm (Fig. 5d). In the 4 plots, $(H/L_{Rod})^2$-dependences were found in excellent agreement with the predictions of Eq. 2. Note that the data for the 7.1 nm were in quantitative agreement with those reported in Ref. [20]. The value of the prefactor in Eq. 2 allowed us to estimate the magnetic susceptibility χ as a function of the particle diameter. To this end, the diameter of the rods was assumed to be particle independent, and it was fixed at $D_{Rod} = 200$ nm for the 4 samples. χ was found to be respectively 2.5 ± 0.5, 1.6 ± 0.3, 5.6 ± 0.8 and 0.9 ± 0.2. Recent calculations of the susceptibility on concentrated dispersions taking into account the magnetic inter-particle interactions have shown that χ should increase typically as $\chi(D) \sim D_0^3$ [27]. The change in the particle diameters from 6.7 to 10.7 nm should have resulted in a fourfold increase of the susceptibility. This result was not observed in the present work. This discrepancy could stem from the assumption made for the rod diameter. The diameter appears as a quadratic dependence in Eq. 2, and small variations on D_{Rod} from one sample to the other may impact considerably the estimations for χ. These findings finally suggest that the 90°-reorientation kinetic measurements should be performed in parallel with an accurate determination of the rod diameters by TEM.

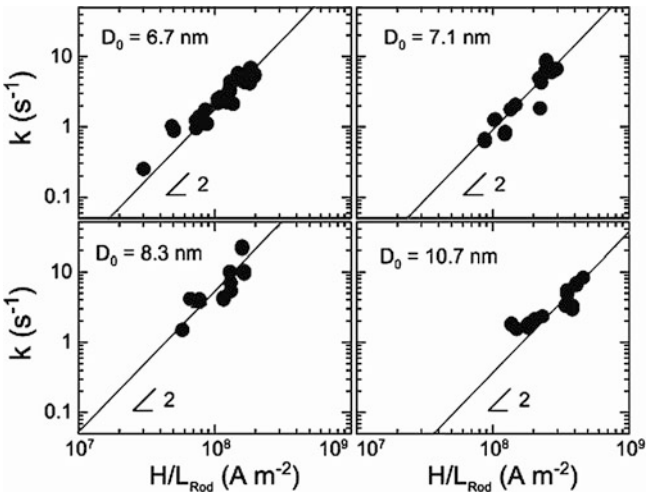

Fig. 5 Variation of the parameter k as a function of the ratio H/L_{Rod} for rods made from particle of diameters 6.7 nm, 8.3 nm, 7.1 nm and 10.7 nm. k is the slope of the exponential decay, H the external magnetic excitation applied to the rod and L_{Rod} its length. The straight line was computed according to Eq. 2, in agreement with a quadratic dependence $(H/L_{Rod})^2$.

Conclusion

In this communication, we have shown that the electrostatic interactions between oppositely charged magnetic nanoparticles and polymers can be controlled by tuning the ionic strength of the dispersion. With decreasing I_S, the electrostatically screened polymers and nanoparticles undergo an abrupt transition between an unassociated and a clus-

tered state. By tuning the desalting kinetics dI_S/dt from 1 to 10^{-5} M s^{-1}, the size of the magnetic clusters was varied from 100 nm to $\sim$ 1 μm. Under the application of a magnetic field, nanostructured rods with lengths in micrometer range were fabricated. We demonstrate here that the rods have inherited the properties of the nanoparticles, namely to be superparamagnetic. This was shown for particles with sizes ranging from 6.7 to 10.7 nm by investigating the 90°-reorientation kinetics of rods. It was found that the decay rate varied as $(H/L_{Rod})^2$, in good agreement with theoretical predictions. The present approach of magnetic nanoparticle co-assembly should open new perspectives for the fabrication of nanodevices such as tips, tweezers and actuators applicable in biophysics and biomedicine.

Acknowledgement We thank Jérôme Fresnais, Olivier Sandre and Régine Perzynski for fruitful discussions. The Laboratoire Physico-chimie des Electrolytes, Colloïdes et Sciences Analytiques (PECSA, Université Pierre et Marie Curie, Paris, France) is acknowledged for providing us with the nanoparticles and for the access to the TEM facilities. This research was supported by the Agence Nationale de la Recherche under the contract BLAN07-3_206866, by the European Community through the project : "NANO3T—Biofunctionalized Metal and Magnetic Nanoparticles for Targeted Tumor Therapy", project number 214137 (FP7-NMP-2007-SMALL-1) and by the Région Ile-de-France (DIM project on Health, Environnement and Toxicology).

References

1. Bungenberg-de-Jong MG (1949) in: H.R. Kruyt (Ed.) Elsevier New York 335
2. Laugel N, Betscha C, Winterhalter M, Voegel J-C, Schaaf P, Ball V (2006) J. Phys. Chem. B 110:19443
3. Raspaud E, Olvera-de-la-Cruz M, Sikorav J-L, Livolant F (1998) Biophys. J. 74:381
4. Jeong JH, Kim SW, Park TG (2003) Bioconjugate Chem. 14:473
5. Weinbreck F, de Vries R, Schrooyen P, de Kruif CG (2003) Biomacromolecules 4:293
6. Olvera-de-la-Cruz M, Belloni L, Delsanti M, Dalbiez JP, Spalla O, Drifford M (1995) J. Chem. Phys 103:5781
7. Bronich TK, Cherry T, Vinogradov S, Eisenberg A, Kabanov VA, Kabanov AV (1998) Langmuir 14:6101
8. Zhou S, Yeh F, Burger C, Chu B (1999) J. Phys. Chem. B 103:2107
9. Berret J-F (2005) J. Chem. Phys. 123:164703
10. Biggs S, Scales PJ, Leong Y-K, Healy TW (1995) J. Chem. Soc. Faraday Trans. 91:2921
11. Schneider G, Decher G (2004) Nano Lett. 4:1833
12. Si S, Kotal A, Mandal TK, Giri S, Nakamura H, Kohara T (2004) Chem. Mater. 16:3489
13. Sehgal A, Lalatonne Y, Berret J-F, Morvan M (2005) Langmuir 21:9359
14. Thünemann AF, Schütt D, Kaufner L, Pison U, Möhwald H (2006) Langmuir 22:2351
15. Cölfen H (2001) Macromol. Rapid Commun. 22:219
16. Voets IK, de Keizer A, Cohen Stuart MA (2009) Advances in Colloid and Interface Science 147-148:300
17. Berret J-F, Sehgal A, Morvan M, Sandre O, Vacher A, Airiau M (2006) J. Colloid Interface Sci. 303:315
18. Fresnais J, Berret J-F, Qi L, Chapel J-P, Castaing J-C, Sandre O, Frka-Petesic B, Perzynski R, Oberdisse J, Cousin F (2008) Phys. Rev. E 78:040401
19. Fresnais J, Lavelle C, Berret JF (2009) The Journal of Physical Chemistry C 113:16371
20. Fresnais J, Berret J-F, Frka-Petesic B, Sandre O, Perzynski R (2008) Adv. Mater. 20:3877
21. van Holde KE (1989) Chromatin Springer-Verlag New York
22. Massart R, Dubois E, Cabuil V, Hasmonay E (1995) J. Magn. Magn. Mat. 149:1
23. Berret J-F, Sandre O, Mauger A (2007) Langmuir 23:2993
24. Chanteau B, Fresnais J, Berret JF (2009) Langmuir 25:9064
25. Jacquin M, Muller P, Talingting-Pabalan R, Cottet H, Berret J-F, Futterer T, Theodoly O (2007) J. Colloid Interface Sci. 316:897
26. Fresnais J, Berret J-F, Qi L, Chapel J-P, Castaing J-C, Co-Assembly Method And Co-Assembled Structures Made Thereby, USA, 2008.
27. Gazeau F, Boue F, Dubois E, Perzynski R (2003) Journal of Physics: Condensed Matter 15:S1305

Progr Colloid Polym Sci (2010) 137:41–45
DOI: 10.1007/978-3-642-13461-6_9

Bacterial Attachment Response on Titanium Surfaces with Nanometric Topographic Features

Vi Khanh Truong[1], James Wang[2], Rimma Lapovok[3], Yuri Estrin[3,4], Francois Malherbe[1], Christopher Berndt[2], Russell Crawford[1], and Elena Ivanova[1]

Abstract The bacterial attachment response on titanium surfaces with various degrees of nano-roughness in the range of 14 nm to 0.6 nm has been investigated. Titanium surfaces were fabricated from commercial purity grade 2 (as-received) titanium, titanium modified by equal channel angular pressing (modified titanium) and titanium thin film of 12 nm and 150 nm obtained using a magnetron sputtering system. The chemical composition, wettability and surface architecture of Ti surfaces were characterised using X-ray photoelectron spectroscopy, contact angle measurements and atomic force microscopy. Two human pathogenic bacteria, *Staphylococcus aureus* CIP 68.5 and *Pseudomonas aeruginosa* ATCC 9025 were found to respond differently to each of the tested surfaces. The results indicate that bacteria can differentiate between surfaces with the fine (less than 1 nm) change of topographic characteristics, the number of retained cells differing by a factor of up to 2.

Keywords Titanium surfaces • Equal channel angular pressing (ECAP) • Titanium thin films • Bacterial adhesion • *Staphylococcus aureus* • *Pseudomonas aeruginosa* • Nanotopography

E. Ivanova (✉)
[1]Faculty of Life and Social Sciences,
Swinburne University of Technology,
Po Box 218, Hawthorn, Victoria, 3122, Australia
e-mail: eivanova@swin.edu.au
[2]IRIS, Swinburne University of Technology,
Po Box 218, Hawthorn, Victoria, 3122, Australia
[3]ARC Centre of Excellence for Design in Light Metals,
Department of Materials Engineering, Monash University,
Clayton, Victoria, 3800, Australia
[4]CSIRO Division of Process Science and Engineering,
Clayton South, Victoria, 3169, Australia

Introduction

High biocompatibility, low toxicity and high corrosion resistance of titanium has warranted its common use in dental implants, cardiac valves, maxiofacial surgery and vascular stents [1, 2]. However, implant-related infection has been of concern due to the loss of device function and the need for implant-removal surgery [3-5]. Implant related infections caused by human pathogenic bacteria that form biofilms on the implant surfaces are difficult to treat due to reduced susceptibility to antimicrobial agents of the biofilm bacteria compared to planktonic bacteria of the same species [6, 7]. Biofilm removal from indwelling devices is also an issue of concern. An estimate by the Centre for Disease Control and Prevention (CDC) indicated that 65% of human bacterial infections involve biofilm formation [8]. For example, Troodle et al., showed biofilm formation by *S. aureus, E. coli* and *P. aeruginosa* on all samples collected from catheters removed from patients [9]. *S. aureus* strains in particular are reported to be significant contributors to infections associated with orthopedic implants [8]. Hence, investigation of the topographic characteristics of titanium surfaces that may affect the retention of human pathogenic bacteria is an important step in the efforts to reduce bacterial infection. In this study, titanium surfaces with varying nano-roughness (R_a) of 14 nm, 12 nm, 0.9 nm and 0.6 nm were fabricated in order to test the response of *S. aureus* and *P. aeruginosa*.

Methods

Titanium surface preparation

Commercially pure ASTM Grade-2 titanium was used to fabricate bulk samples of 'as-received' titanium surfaces. In addition, billets from this material, 10 mm in diameter

© Springer-Verlag Berlin Heidelberg 2010

and 35 mm in length, were subjected to 8 passes of a severe plastic deformation process known as equal channel angular pressing (ECAP) at 350°C to produce an ultrafine grain structure of Ti in the bulk of the material, as described previously [10, 11]. The ultrafine grain structure of the bulk gave rise to a modified surface morphology of Ti.

In a separate process, titanium thin films of 12 nm and 150 nm thickness (henceforth referred to as 12 or 150 nm films) were prepared on the pre-cleaned plain microscope slide substrata (Biolab Scientific Ltd) using a Kurt J Lesker CMS -18 magnetron sputtering thin film deposition system in direct current mode at an argon gas pressure of 4 m Torr and a power of 150 kW. The preparatory steps of Ti thin films were described elsewhere [12].

Titanium thin film surface characterization

The contact angles of different solvents on titanium disks made from the following four materials: 'as received' Ti, modified Ti, 12 nm film and 150 nm film were measured using the sessile drop method [13]. Three solvents, MilliQ water, formamide (Sigma) and diidomethane (Sigma) were used. An FTA1000 (First Ten Ångstroms Inc.) instrument was used to measure the contact angles at room temperature (ca 23°C) in air. An average of at least five measurements was taken for each solvent and each titanium surface. Each measurement of a particular contact angle was recorded in 50 images in 2 seconds with a Pelco Model PCHM 575-4 camera, and the contact angle was determined based on images analyzed using the FTA Windows Mode 4 software. The average contact angle for each of the three solvents on each surface was used to calculate the surface free energy and its components, based on the Lewis acid/base method [13].

A scanning probe microscope (SPM) (Solver P7LS, NT-MDT) was used to obtain images of the surface morphology and to quantitatively measure and analyze the surface roughness of Ti surfaces at nanometer scale. Analysis of surface topography was performed as described in our earlier publications [11, 12].

The composition of the titanium surfaces was determined by X-ray photoelectron spectroscopic analysis using a Kratos Axis Ultra DLD spectrometer (Kratos Analytical Ltd, U.K.). The energy scale of the instrument was calibrated by measuring the Au 4f7/2 (E_b = 84.0 eV), Ag 3d5/2 (E_b = 368.3 eV), and Cu 2p3/2 (E_b = 932.7 eV) binding energies for pure metal foils. Spectra were recorded while irradiating the samples with a monochromated Al Kα source (hν = 1486.6 eV) operating at 150W. The area tested was approximately 300 μm × 700 μm.

Bacterial strains

The bacteria used in this study were *Staphylococcus aureus* CIP 68.5 and *Pseudomonas aeruginosa* ATCC 9025. Bacterial strains were obtained from American Type Culture Collection (ATCC, USA) and Culture Collection of the Institute Pasteur (CIP, France). Bacterial strain stocks were prepared in 20% glycerol nutrient broth (Merck) and stored at −80°C. Both strains were cultured on nutrient agar (Oxoid) and nutrient broth (Oxoid) at room temperature (ca. 22°C).

Cellular surface charge measurements

Bacterial cell surface hydrophobicity was evaluated from contact angle measurements on lawns of bacteria using the sessile drop method as described elsewhere [14]. In brief, bacterial cells in a buffer (OD(600) = 0.3) were deposited on cellulose acetate membrane filters (Sartorius, 0.2 μm). The wet filters were air dried at ambient temperature (ca. 22°C) for approximately 30 - 40 minutes to attain a "plateau state".

Zeta potential data for both strains were obtained by measuring the electrophoretic mobility (EPM) using a standard protocol described elsewhere [15]. The EPM was measured as a function of ionic strength by microelectrophoresis using the Zeta Potential Analyser (ZetaPALS, Brookhaven Instruments Corp, Holtsville, NY). The bacterial cell suspension was freshly prepared before the measurement. All measurements were executed in triplicate and for each sample the final EPM quoted represented an average over 5 successive ZetaPALS readings, each of which consisted of 14 cycles per run. All data were processed using software that employed the Smoluchowski equation [15, 16].

Bacterial growth and sample preparation

Prior to each experiment, a fresh bacterial suspension was prepared for each of the strains grown overnight in 100 mL of nutrient broth (Oxoid) (in 0.5 L Erlenmeyer flasks) at 37 °C with shaking (120 rpm). Sample preparation was performed as previously described [11, 12]. In brief, an aliquot of 5 mL of bacterial suspension was added in a sterile Petri dish with samples. These were incubated for 18 h at room temperature (ca. 22°C). Sterile nutrient broth (5 mL) was used as a negative control. Samples were handled under sterile conditions until just prior to imaging.

In all scanning electron microscopy experiments, titanium surfaces with adsorbed bacteria were initially sputter-coated

with 20 nm gold thin films using a Dynavac CS300. High-resolution images of titanium thin films with the retained bacterial cells were taken using a FESEM (ZEISS SUPRA 40VP) at 3 kV at 1,000×, 5,000× and 20,000× magnification. Images at 1,000× and 5,000× magnification were used to calculate the number of bacteria adhering to the titanium surfaces; the results were statistically analysed.

Results and Discussion

Titanium surface characterization

The results of the elemental analysis of the titanium surfaces confirmed that the most abundant elements on the surfaces of all titanium samples (up to 87 at. %) were titanium and oxygen. The XPS survey spectrum demonstrated some carbon contamination on the titanium surface, which is typical for adventitious, unavoidable hydrocarbon contamination adsorbing spontaneously from ambient air onto the surface [17–19].

The modified titanium surfaces of bulk titanium were found to be more hydrophilic than the as-received samples, with water contact angles θ_W of approximately 63°, whilst the as-received titanium surfaces had water contact angles θ_W of approximately 73° (Table 1). The difference in contact angle is regarded as statistically significant (*t*-test: $p = 0.03$ (<0.05)). Ti thin films of 150 nm thickness were found to be moderately hydrophobic (a contact angle of approximately 81°), while 12 nm films were found to be less hydrophobic (contact angles of approximately 76 - 75°). The difference in contact angles is regarded as statistically significant (*t*-test: $p = 0.03$ (<0.05)). All titanium surfaces exhibited electron donor components rather than electron acceptor components indicating that negative charges were formed on a titanium surface due to the presence of a TiO_2 layer [19]. The value of the total surface free energy for the 150 nm films were found to be slightly lower than that for the 12 nm films (Table 1). However, statistical analysis showed that no statistically significant difference existed between the total surface free energies of these films (*t*-test: $p < 0.05$).

Three parameters used for conventional surface topography characterisation, namely the average roughness (R_a), the root mean square roughness (R_q) and the maximum roughness (R_{max}), on the 10 µm × 10 µm scanning areas were analysed (Table 2). The results revealed that ECAP-modified titanium surfaces were nano-smooth, with R_a and R_q of approximately 12 nm and 15 nm, respectively, versus $R_a = 15$ nm and $R_q = 18$ nm for the as-received titanium surfaces. This difference between as-received and ECAP titanium surfaces was shown not to be statistically significant ($t = 0.067$ and 0.075 for R_a and R_q, respectively, $p > 0.05$). However, a significant difference in surface topography between as-received and modified titanium surfaces was confirmed for R_{max} on both scanning areas ($t = 0.047$, $p < 0.05$).

Titanium thin film surfaces appeared to be homogeneous; the average roughness was much smaller than for the surfaces of bulk Ti. Thus, the 150 nm thick film exhibited R_a as low as 0.6 nm. A similar trend was also seen for the maximum peak height (R_{max}). A statistical analysis of the R_{max} data showed no significant difference in the maximum height for the 12 nm and 150 nm films ($t = 0.22$, $p > 0.05$).

It is also noted that a lower surface roughness of the films translated to a higher surface hydrophobicity (Table 1 and 2). This phenomenon has been referred to as roughness-induced hydrophobicity [21].

Bacterial attachment patterns on Ti surfaces

The responses of the two species of bacteria investigated indicate that - to some degree - they were able to differentiate between the titanium surfaces of different morphology

Table 2 AFM surface roughness analysis of Ti surfaces

Ti surfaces	Average Roughness (nm) R_a	RMS Roughness (nm) R_q	Maximum height (nm) R_{max}
As-received	14.0 ± 1.3	18.1 ± 1.9	164.0 ± 30.8
Modified	12.2 ± 1.8	14.9 ± 1.5	19.6 ± 29.9
12 nm	0.90 ± 0.01	1.20 ± 0.01	15.9 ± 2.5
150 nm	0.60 ± 0.02	0.90 ± 0.04	13.3 ± 2.0

Table 1 Comparative evaluation of physico-chemical characteristics of titanium surfaces

	Contact angles (degrees)			Surface free energy components (mJ/m^2)				
	θ_W*	θ_F	θ_D	γ^{LW}**	γ^{AB}	γ^+	γ^-	γ_{TOT}
As-received	73 ± 2	39 ± 2	48 ± 5	40.0	4.3	0.7	6.8	44.3
Modified	63 ± 5	39 ± 2	45 ± 5	40.2	5.0	0.4	16.5	45.2
12 nm	75 ± 1	48 ± 4	38 ± 1	44.3	40.4	3.9	0.6	6.0
150 nm	81 ± 1	52 ± 4	40 ± 1	42.3	39.7	2.7	0.6	2.8

*θ_W, θ_F and θ_D: water, formamide and diidomethane contact angles respectively.
** Surface free energies components: Lifshitz-van der Waals (γ^{LW}), acid/base (γ^{AB}), electron acceptor (γ^+) and electron donor (γ^-) components; and total surface free energy (γ_{TOT})

and nano-roughness (R_a) varying from 14 nm to 0.6 nm (Figures 1-2). Table 3 shows the increase of the number of attached cells of *P. aeruginosa* and *S. aureus* with the decrease of roughness from as-received (bulk) Ti to 150 nm Ti thin film. Figure 2 shows the results of SEM analysis, which clearly demonstrate that the number of *P. aeruginosa* and *S. aureus* cells attached onto the titanium surface follows the roughness decrease from the highest level for as-received bulk Ti down to the 150 nm Ti film. As was the case with *S. aureus*, *P. aeruginosa* cells also showed a preference for attachment to nano-smoother surfaces (cf. Table 3 and Figure 2), although *P. aeruginosa* appeared to be a poor coloniser of the titanium surfaces. It should be noted that *P. aeruginosa* cells were found to be moderately hydrophilic ($\theta = 43°$) and *S. aureus* cells exhibited more hydrophobic characteristics ($\theta = 72°$). The hydrophobic nature of *S. aureus* cells can be attributed to the presence of highly negatively charged and hydrophobic teichoic and lipoteichoic acid sites, which are some of the main constituents of *S. aureus* cell walls [22]. The measured cellular surface charges of *P. aeruginosa* and *S. aureus* were -14.4 ± 0.7 mV and -35.2 ± 1.0 mV, respectively. Our data are in agreement with earlier studies, which reported that although more electronegative cells were expected to be more hydrophilic, due to the presence of EPS/lipopolysaccharides on the surface, some bacterial cells could still exhibit hydrophobic characteristics. These owe mainly to variations in surface polarity or an electric charge associated with the constant motion of the outer surface proteins [15, 16, 23-26]. Indeed, it was found that bacterial cell surface wettability also influenced the ability of the bacteria to attach to the surface. Being hydrophobic, *S. aureus* cells were more inclined to attach to hydrophobic titanium surfaces than *P. aeruginosa*.

Previously published observations have shown that the topography of micro-rough titanium surfaces influenced the attachment and growth of *P. fluorescens* and *S. aureus* [5, 27]. Known as contact guidance, cell growth along the trenches in long rows was observed, whereas the cells attached unevenly to smooth surfaces [5, 28]. Some studies reported that bacteria display no preference for adhering to surface scratches or grooves and regarded surface roughness as a 'minor factor' [29, 30]. A study [7] showed no significant trend in the adherence of *S. epidermidis* to titanium with the surface roughness (R_a) ranging from 0.44 nm to 1.25 nm. By contrast, our investigations reported here demonstrate unequivocally that the nano-scale topography of Ti surfaces does influence the bacterial attachment response [11, 12, 14]. The role of other factors, such as texture, grain boundary area, thickness of a TiO_2 layer on the Ti surface, etc., which may be different depending on the

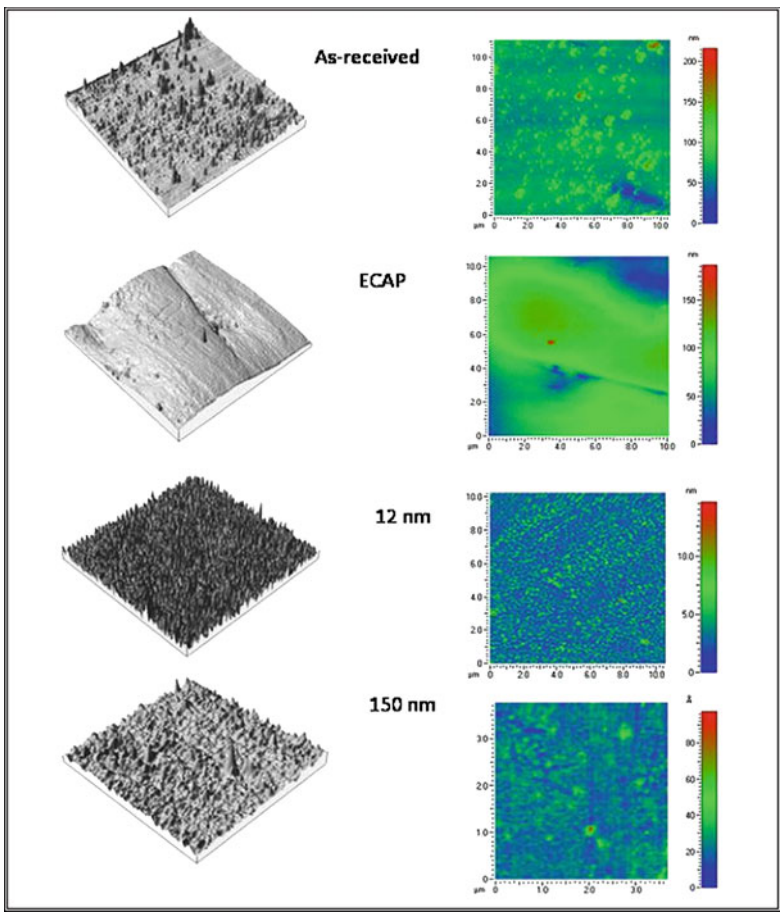

Fig. 1 Typical 3D and 2D AFM images of as-received, ECAP-modified, 12 nm and 150 nm Ti surfaces from 10 μm × 10 μm scanned areas.

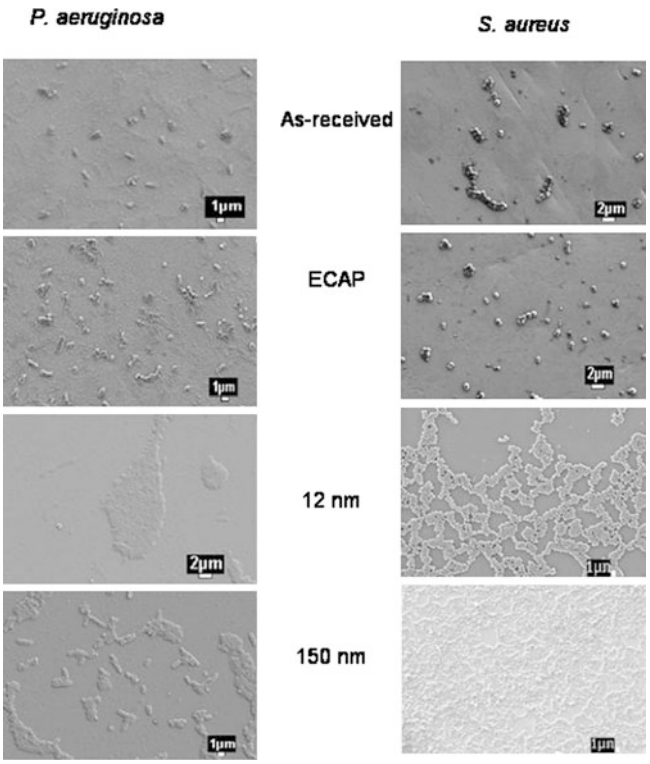

Fig. 2 Typical SEM images of *P. aeruginosa* and *S. aureus* attachment patterns on as-received, ECAP-modified, 12 nm and 150 nm thicknesses titanium surfaces after 18 h incubation.

Table 3 Bacterial cell surface characteristics and numbers of retained cells on titanium surfaces

Bacterial strain	Retained cells[a] $\times 10^5$ [number of cells per mm^2]			
	As-received	Modified	12 nm	150 nm
P. aeruginosa	0.20 ± 0.02	0.50 ± 0.05	1.0 ± 0.2	1.8 ± 0.4
S. aureus	0.50 ± 0.05	0.70 ± 0.07	6.0 ± 1.1	12.0 ± 1.7

[a]Cell densities have estimated errors of approximately 15-20% due to local variability in the surface coverage.

technique used to produce the specimens, will be the subject of further studies.

Conclusion

Two methods – equal channel angular pressing and magnetron sputtering - were employed to fabricate titanium surfaces with different topography characterized by the roughness (R_a) varying from 14 nm to 0.6 nm. The attachment patterns of *P. aeruginosa* and *S. aureus* indicated clearly that both bacterial species responded differently to the variation of 0.3 nm – 0.5 nm change in average surface roughness (R_a). The results provide further insights in the effect of surface topography on bacterial attachment of two medically important pathogens. These findings may have implications in the surface design of medical implants

Acknowledgments This study was supported in part by Australian Research Council (ARC) and Advanced Manufacturing CRC. VKT is a recipient of Postgraduate Swinburne University Postgraduate Research Award. YE would like to acknowledge support through World Class University project of National Research Foundation of Korea funded by the Ministry of Education, Science and Technology (R31-2008-000-10075-0).

References

1. K.A. Whitehead, J. Verran, (2007) Int. Biodeterior. Biodegrad. 60: 74-80.
2. Y.L. Jeyachandran, B. Karunagaran, S.K. Narayandass, D. Mangalaraj, T.E. Jenkins, P.J. Martin, (2006) Mater. Sci. Eng. A 431: 277-284.
3. M.C. Hudson, W.K. Ramp, K.P. Frankenburg, (1999) FEMS Microbiol. Lett. 173: 279-284.
4. Y.L. Ong, A. Razatos, G. Georgiou, M.M. Sharma, (1999) Langmuir 15: 2719-2725.
5. C. Diaz, M.C. Cortizo, P.L. Schilardi, S.G.G. de Saravia, M.A.F.L. de Mele, (2007) Mater. Res. 10: 11-14.
6. R.M. Donlan, (2001) Clin. Infect. Dis. 33: 1387-1392.
7. Y.H. An, R.J. Friedman, R.A. Draughn, E.A. Smith, J.H. Nicholson, J.F. John, (1995) J. Microbiol. Methods 24: 29-40.
8. G.J. Tortora, B.R. Funke, C.L. Case, Microbiology: An Introduction, 8th ed., Pearson Education Inc, Benjamin Cummings, San Francisco, 2004.
9. L. Troidle, F. Finkelstein, (2006) Ann. Clin. Microbiol. Antimicrob. 5: 1-7.
10. Y. Estrin, C. Kasper, S. Diederichs, R. Lapovok, (2009) J Biomed Mater Res - Part A 90A: 1239-1242.
11. E.P. Ivanova, V.K. Truong, J. Wang, C.C. Berndt, T.R. Jones, I.I. Yusuf, I. Peake, H.W. Schmidt, C. Fluke, D. Barnes, R.J. Crawford, (2010) Langmuir 26: 1973-1982
12. D. Oner, T.J. McCarthy, (2000) Langmuir 16: 7777-7782.
13. V.K. Truong, S. Rundell, R. Lapovok, Y. Estrin, J.Y. Wang, C.C. Berndt, D.G. Barnes, C.J. Fluke, R.J. Crawford, E.P. Ivanova, (2009) Appl. Microbiol. Biotech. 83: 925-937.
14. N. Mitik-Dineva, J. Wang, R.C. Mocanasu, P.R. Stoddart, R.J. Crawford, E.P. Ivanova, (2008) Biotech. J. 3: 536-544.
15. A.J. de Kerchove, M. Elimelech, (2005) Langmuir 21: 6462-6472.
16. K.E. Eboigbodin, J.R.A. Newton, A.F. Routh, C.A. Biggs, (2005) Langmuir 21: 12315-12319.
17. K. Cai, M. Muller, J. Bossert, A. Rechtenbach, K.D. Jandt, (2005) Applied Surface Science 250: 252-267.
18. I. Bertóti, M. Mohai, J. Sullivan, S. Saied, (1995) Appl. Surface Science 84: 357-371.
19. X. Liu, P.K. Chu, C. Ding, (2004) Mater. Sci. Eng. R: Reports 47: 49-121.
20. D. Öner, T.J. McCarthy, (2000) Langmuir 16: 7777-7782.
21. M. Gross, S.E. Cramton, F. Gotz, A. Peschel, (2001) Infect. Immun. 69: 3423-3426.
22. B. Li, B.E. Logan, (2004) Colloids Surf B: Biointerfaces 36: 81-90.
23. V. Vadillo-Rodriguez, H.J. Busscher, W. Norde, J. Vries, H.C. van der Mei, (2004) J Colloid Interface Sci 278: 251-254.
24. L.G. Harris, S. Tosatti, M. Wieland, M. Textor, R.G. Richards, (2004) Biomaterials 25: 4135-4148.
25. T.R. Scheuerman, A.K. Camper, M.A. Hamilton, (1998) J. Colloid Interface Sci. 208: 23-33.
26. R. Bos, H.C. Van Der Mei, H.J. Busscher, (1999) FEMS Microbiol. Rev. 23: 179-229.
27. N. Mitik-Dineva, J. Wang, V.K. Truong, P. Stoddart, F. Malherbe, R.J. Crawford, E.P. Ivanova, (2009) Curr. Microbiol. 58: 268-273.

Progr Colloid Polym Sci (2010) 137:47–52
DOI: 10.1007/978-3-642-13461-6_10

Synthesis of Carbide Compounds Derived from Colloidal Oxide and Carbohydrate

X. Deschanels[1], M. El Ghazzal[1], C. Delchet[1], D. Herault[2], V. Magnin[1], A. Grandjean[1], R. Podor[1], G. Cerveau[2], T. Zemb[1], and R. Corriu[2]

Abstract Silicon carbide (SiC) and zirconium carbide (ZrC) powders were synthesized by the carbothermal reduction reaction of carbon and the corresponding metal oxide silica or zirconia respectively. The physical and chemical properties of the final products were studied according to the nature of precursors used: colloidal or micrometric powders for the oxides, sucrose, mannitol or sorbitol for the reducing agent. After mixing and freeze drying of these components, the powder was heated at temperatures ranging from 1300 and 1550°C under flowing argon to obtain the carbides. Depending on the nature of the precursors (colloidal or micrometric) an increase of more than one order in the magnitude of the surface area was observed. The highest surface area ($300 m^2/g$) was measured on a ZrC+C compound type elaborated from a colloidal precursor. The use of colloids in carbothermal reaction could be a route to control pore size in mesoporous carbides or supported porous carbon materials.

Keywords Carbide • Carbothermal reduction • Colloidal route • Carbohydrate

Introduction

Carbides constitute a class of materials that exhibit the characteristics of ceramic compounds such as high hardness, high melting point, high strength, good wear and good corrosion stability [1]. These properties allow them to be a good candidate for many technological applications in the field of advanced ceramic industry (cutting tools application, wear resistance. . . .). Recently, two new applications have emerged: metallic carbide compounds are developed in the field of catalysis because of the availability of metal carbide with high surface areas [2]. Another interesting property of ceramics concerns the high thermal conductivity of such carbides. The thermal conductivity of carbide compounds is well above that of oxide compounds which are the current reference fuels in nuclear industry [3]. Accordingly, actinide carbides and SiC, ZrC have respectively been considered as potential material for the fuel or the structural materials in the core of the nuclear reactors [4–6]. This last point is being widely discussed in the framework of the Generation-IV international project [7].

Several approaches have been used to synthesize carbides [1]. Direct methods consist of the reaction of the oxide or the metal oxide with solid carbon at high temperature (∼ 2000°C). These methods lead to compounds with low surface area. In contrast, other synthesis routes involving reaction between a liquid or gaseous phase are used to obtain compounds with high surface area. The direct methods are generally used to elaborate the compounds studied in this work (SiC, ZrC). The main drawback of these routes is the use of high temperature (>2000°C) which leads to coarse-grained powders with particle size higher than 1 micron. One possibility to overcome this problem is to reduce the size of starting products from micrometric to nanometric scale [8]. Recently, several authors [5–6, 9–13] have used this route to obtain carbide. In this work, a process similar to that described by Martin [9] has been used. It consists in the carbothermal reduction of the oxide (colloidal or micrometric) by carbon obtained after the pyrolysis of a carbohydrate. This technique provides the ability to intimately mix the reagents and to encapsulate the oxide in a carbon matrix. The characteristics of the final products (surface area, crystallite size) were studied according to the size and the nature of the precursors. The main goal of this work was to investigate the relation between initial surface contact between carbohydrate and silica/zirconia to final interfacial area of the porous material obtained (Fig. 1).

[1]X. Deschanels (✉)
Institut de Chimie Séparative de Marcoule, UMR 5257,
BP 17171, 30207 Bagnols-sur-Cèze, France
e-mail: xavier.deschanels@cea.fr
[2]Institut Charles Gerhardt, UMR 5253,
Université de Montpellier 2, 34095 Montpellier, France

© Springer-Verlag Berlin Heidelberg 2010

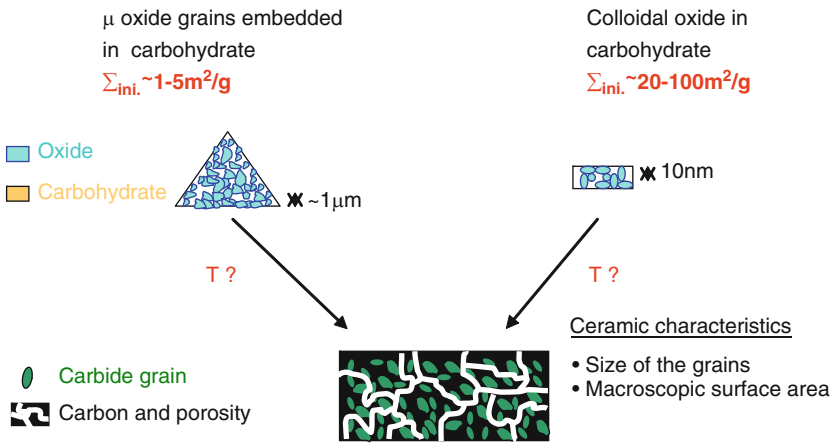

Fig. 1 Schematic representation of the goal of this study

Experimental Procedure

The carbothermal reduction of a metal oxide can be described as depicted in equation (1):

$$MO_2(S) + 3C(s) \rightarrow MC(s) + 2CO(g) \quad (1)$$

Various precursors were used to elaborate the carbides. A colloidal suspension of zirconia was graciously provided by the company IMCD (IMCD France, Saint-Denis La Plaine). These colloids have a particle size ranging from 5–10nm and are stabilized by acetate ions. A micrometric zirconia powder was purchased from Sigma-Aldrich. The grains of this powder have a characteristic dimension of approximatively 5–10 micrometers. These various zirconia powders have been used to compare the influence of particle size. Fumed silica is amorphous silica; it has a chain-like particle morphology composed of submicron-sized spheres (7 nanometers), which are highly branched (nominal size 0.1–0.2 microns). Its surface area is close to $360m^2/g$. Concerning the reducing agent, several carbohydrates (sucrose, mannitol, sorbitol) were used.

The method used for the synthesis of the sample is shown in figure 2. In a first stage, the oxide particles are mixed together with a quantity of carbohydrate solution corresponding to the target final stoichiometry. This suspension guarantees homogeneous dispersive mixing in a simple way. The amount of carbohydrate is adjusted in a proportion ranging between 1 and 8 times the quantity needed by the reaction (1) to obtain a complete conversion of the parent compounds. The C/M ratio quantifies the deviation from stoichiometry, i.e C/M=1 means the reagents are mixed together in the proportion of the reaction (1). In a second stage, the suspension is freeze dried to obtain a powder. The powders are then compacted into pellets (diameter 10–15 mm) under a pressure of about 200MPa to obtain a better confinement of the parent oxide by the surrounding carbohydrate. The pellets are heat treated at temperature ranging from 1100°C to 1550°C under flowing argon. The temperature and the ratio C/M are adjusted to obtain a maximum yield for reaction (1). The same protocol is followed for the transformation of silica and zirconia in their respective carbides.

Results and Discussion

Synthesis of carbide

Thermogravimetric analysis were performed on the sucrose + oxide precursor for the C/Zr = 2 and C/Si = 1.2 ratio corresponding to the minimum values of the C/M ratio to obtain the carbides (Fig. 3). The general shape of the curves is similar for all the precursors based on sucrose+oxide mixtures. For temperatures below 800°C the weight loss is attributed to the decomposition of sucrose into carbon. Above 1300°C, a second weight loss is observed. It can be interpreted as a consequence of oxide carboreduction reaction. For both silica and zirconia compounds, the mass of the final product is stabilized at T = 1550°C, indicating that the carbothermal reduction is complete. Above 1300°C the weight loss is more important for the silica precursor in comparison to zirconia because of the formation of gaseous SiO. It has been suggested that under reducing conditions, the mechanism of the silica carbothermal reduction leads to the formation of the gaseous SiO species [10]. Thus, the carbothermal reduction of silica can be described as follow:

$$SiO_2(s) + C(s) \rightarrow SiO(g) + CO(g) \quad (2)$$

$$SiO(g) + 2C(s) \rightarrow SiC(s) + CO(g) \quad (3)$$

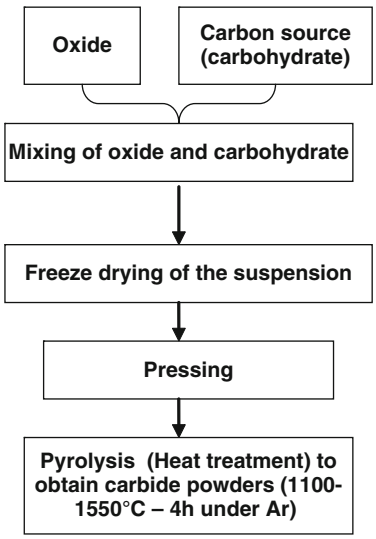

Fig. 2 Flow chart for synthesis of carbide from solution–based precursors

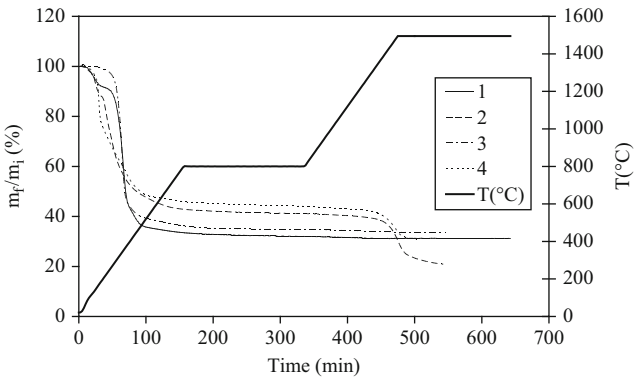

Fig. 3 Thermogravimetric analyses under argon flowing of various precursors: 1-sorbitol+fumed silica (C/Si=1.2); 2-sucrose+fumed silica (C/Si=1.2); 3-manitol+fumed silica (C/Si=1.2); 4-sucrose+zirconia (C/Zr=2)

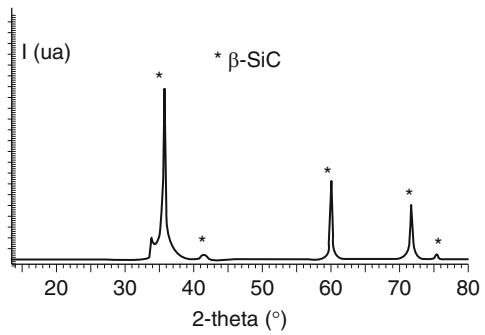

Fig. 4 X-ray diffraction pattern for heat-treated (1550°C-h) sample prepared from fumed silica+sucrose (C/Si=1)

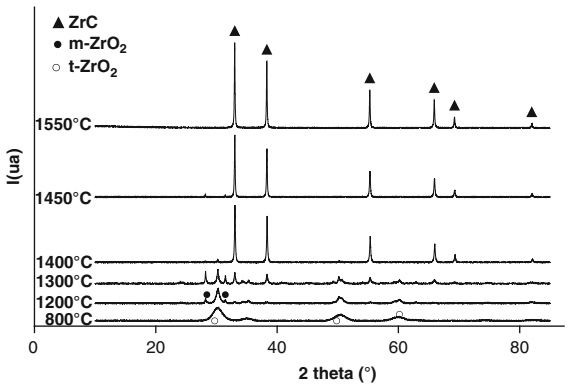

Fig. 5 X-ray diffraction patterns for heat-treated (800°C–1550°C, 4h) samples prepared from zirconia colloid+sucrose (C/Zr=2)

According to thermodynamic calculations, the temperature at which the reaction is initiated strongly depends on pressure and atmosphere composition (oxygen and CO fugacity).

The XRD pattern shows β-SiC phase with a peak shoulder (2-theta=34°) which may be due to the presence of α-SiC or stacking faults (Fig. 4). The conversion of the precursors into ZrC versus temperature is reported on figure 5 and corresponding data are gathered on table 1. These results confirm that the transformation of zirconia into ZrC occurs above 1300°C. Between 800 and 1300°C, monoclinic and tetragonal zirconia phases are detected. The tetragonal zirconia is usually observed during the crystallization of colloidal zirconia [14]. This phase is transformed into monoclinic zirconia during the temperature increase.

The oxide conversion rate is also characterized by the remaining oxygen content in ZrC or SiC final products. Results reported on table 1 indicate a sharp decrease of this parameter between 1300°C and 1400°C and a stabilization for temperature higher than 1300°C. Jointly, the carbon content is also stabilized at a value close to 19wt.%, indicating the presence of residual carbon into the final product. However, X-Ray diffraction does not allow the detection of carbon in these samples. The carbon is probably amorphous in the final product. Finally, SEM observations performed on this sample (Fig. 6 and Fig. 7) indicate that this residual carbon acts as a binder between the carbide grains and causes the formation of hard aggregates with a micrometer size. These aggregates are composed of nanometric crystallites. The temperature reaction is not affected by the size of the precursor (micrometer or nanometer) (Table 1).

The thermogravimetric curves obtained on fumed silica mixed with different carbohydrates (mannitol, sorbitol, sucrose) (C/SiO_2 ratio = 1.2) are reported on figure 3. When temperature remains below 800°C, the weight losses recorded for mannitol and sorbitol containing precursors are higher than the ones measured for sucrose. This can be attributed to the evaporation of these carbohydrates when they reach their boiling point (296°C and 295°C for sorbitol and mannitol

Table 1 Phase detected by X-rays diffraction, elementary analysis of carbon and oxygen of the obtained powders depending on the temperature of the pyrolysis of zirconia+sucrose precursors (m-ZrO_2:monoclinic ZrO_2; t- ZrO_2:tetragonal ZrO_2)

Heat treatment	X-Rays (Phases detected)	O wt.%	C wt.%
Sucrose + ZrO_2colloidal C/Zr=2			
800°C	m-ZrO_2	21.9	n.d.
1200°C – 4h	m-ZrO_2+ t-ZrO_2	18.9	26.1
1300°C – 4h	m-ZrO_2+ t-ZrO_2 + ZrC	16	23.4
1400°C – 4h	m-ZrO_2+ t-ZrO_2 + ZrC	6.4	18
1500°C – 4h	m-ZrO_2+ ZrC	5.2	16.4
1550°C – 4h	ZrC	5.12	19.1
Sucrose + ZrO_2micrometric C/Zr=2			
1550°C – 4h	ZrC	4.81	11.62

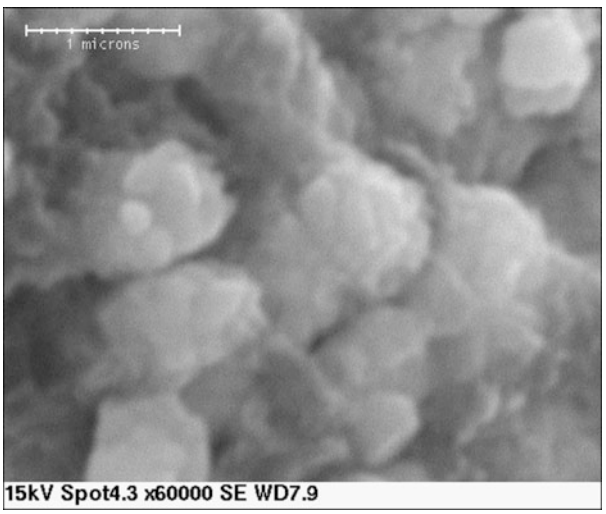

Fig. 6 SEM micrograph of β-SiC+C powders synthesized at 1550°C-4h (C/M=8)

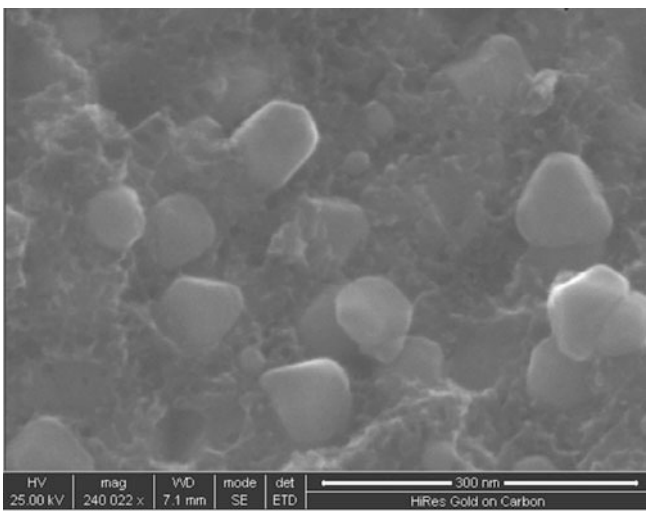

Fig. 7 SEM micrograph of ZrC+C powders synthesized at 1550°C-4h (C/M=8)

respectively). Conversely, sucrose is decomposed into carbon and volatile compounds, and the remaining carbon reacts with the oxide at the temperature of the carbothermal reaction. This explains why sucrose is more efficient than manitol or sorbitol for the carbothermal reduction process.

Influence of the C/M ratio

This parameter was studied to assess the influence of the oxide particles encapsulation by a carbon network on the carbothermal reduction temperature. Corriu [8] has observed a decrease in the temperature of the carboreduction of TiO_2 and ZrO_2 embedded into a carbon matrix resulting from the pyrolysis of a polymer. He explains this result by the fact that the ceramic is prepared by a kinetic route. This method is completely different from the classic route which consists in the direct mixing of carbon with the oxide before heat treatment. In this case the sample is under thermodynamic control. Taking into account the results reported in the section "Synthesis of carbides", these tests have only been performed on the "sucrose + oxides" precursor. Surprisingly, no change was observed in the temperature of the carbothermal reaction according to this parameter in our experiments. Similarly, no change was observed on the carbothermal reduction temperature according to the nature of the precursors (colloidal, micrometric powders). However, whatever the initial surface of contact, the temperature of the reduction of silica remains much below the temperature required in the Acheson process [15] (T=2000°C). This difference could be explained by a change in process parameters that modify the temperature at which reactions (2) and (3) are initiated; and therefore the formation of SiO gas.

Characterization

A strong increase in the specific surface area (BET) of the final products prepared from carbohydrate + nano-sized oxide (colloidal ZrO_2, fumed SiO_2) has been observed depending on the C/M ratio (Fig. 8). No significant change was observed for powders obtained from micrometric zirconia. This result is the most important difference between the two precursors (nano-sized and micrometric). The highest specific surface area that was measured for the compound ZrC+C (C/Zr ratio = 4) is equal to 300m^2/g. Beyond this C/Zr ratio value, the specific surface area does not increase any more. In comparison, the specific surface area increase determined for the powders synthesized from silica fumed+sucrose mixture is less intense according to the C/Si ratio. The highest value measured is equal to 150m^2/g, corresponding to a C/Si=12 ratio. A hysteresis was observed on the adsorption-desorption isotherm of the

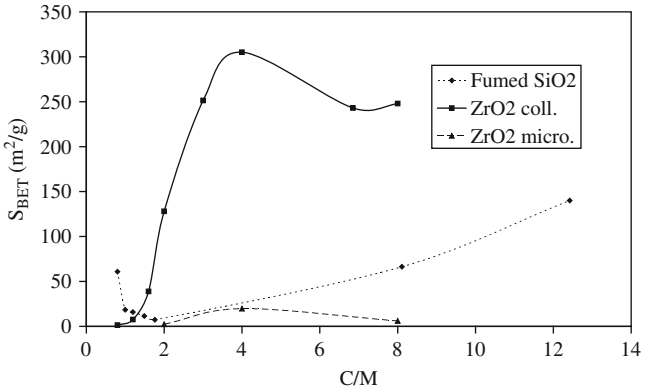

Fig. 8 Specific surface area (BET) of carbides elaborated from various precursors versus the ratio C/M (processing conditions 1550°C-4h under Ar)

Table 2 Phase detected by X-rays diffraction, crystallites size, elementary analysis of carbon and oxygen of the powders elaborated at 155°C-4h under flowing Ar, depending on the ratio C/M for various precursors (m-ZrO_2:monoclinic ZrO_2)

Precursors	C/M	X-rays (Phases detected)	Crystallite size (nm)	O wt. %	C wt. %
Sucrose +ZrO_2 colloidal 5-10 nm	0.8	ZrC+m-ZrO_2	143	n.d.	n.d.
	1.2	ZrC+m-ZrO_2	162	7.25	7.9
	1.6	ZrC+m-ZrO_2	145	4.3	12
	2	ZrC	106	5.1	19.1
	3	ZrC	66	n.d.	n.d.
	4	ZrC	55	4.8	38.1
	6.8	ZrC	n.d.	4	n.d.
	8	ZrC	41	3.5	57.1
Sucrose+ZrO_2 micrometric	2	ZrC	150	4.8	11.6
	4	ZrC	115	6.1	32.6
	6	ZrC	103	2.9	37.8
Sucrose + fumed SiO_2	0.8	SiC+SiO_2	n.d.	n.d.	n.d.
	1	SiC+SiO_2	n.d.	n.d.	n.d.
	1.2	SiC	n.d.	1.77	29.4
	1.5	SiC	n.d.	n.d.	n.d.
	1.8	SiC	n.d.	n.d.	n.d.
	2	SiC	n.d.	n.d.	n.d.
	8	SiC	n.d.	0.35	79.2
	12	SiC	n.d.	0.42	n.d.

sample elaborated from a "colloidal zirconia + sucrose" mixture. That means that these samples present mesoporosity. The mesoporosity is mainly localized in the "residual carbon" phase since the hysteresis is more pronounced when the C/Zr ratio increases. Moreover, the surface morphology characterisation of the powders by SEM indicates the presence of porosity on the "residual carbon" phase (Fig. 7). The size of the mesopores ranges from 30 to 40 Å. On the contrary, mesoporosity was not observed in the samples prepared from "sucrose + fumed silica" mixtures. This difference between these two nano-sized precursors could be related to formation of gaseous SiO compound during the carbothermal reduction of silica. Indeed, SiO can react with the residual carbon and thereby can induce the clogging of the mesoporosity. The crystallite sizes determined from XRD (Table 2) decrease according to the C/Zr ratio increase. This result is consistent with the SEM observations. This variation could be due to the increase of the initial distance between the oxide particles in the precursor medium, which limits the growth of the carbide grains during the carbothermal process.

Conclusion

The feasibility of carbide powders synthesis from oxide (colloidal or micrometric precursors) and sucrose mixtures is confirmed. This processing route does not yield to the formation of carbides when using manitol or sorbitol carbohydrates as carbon precursors, due to the evaporation of these carbohydrates below the carbothermal reaction temperature. No change was observed in the temperature of the carbothermal reaction when varying the precursor grain size (micrometric, nanometric) or the quantity of carbohydrate surrounding the oxide grains. The increase of the ratio between the amount of carbohydrate and oxide (C/M) induces a strong increase on the surface area of the carbide powders elaborated from the nanometric precursors. The initial contact surface between oxide and carbohydrate is in the range 1–5 m^2/g for a micrometric precursor powder, and 20-100 m^2/g for a nanoscale precursor grains, whereas the macroscopic surface areas of the obtained zirconium carbides are <20 and about 300 m^2/g respectively.

Mesoporosity was observed in ZrC+C compounds for C/Zr ratio > 2. The porosity is mainly located in the "residual carbon" phase resulting from the pyrolysis of the carbohydrate. This synthesis route could be interesting to elaborate in one pot new supported porous carbon materials.

References

1. Oyama ST (1996) Introduction to the chemistry of transition metal carbides and nitrides. In: Chapman & Hall (eds) The chemistry of transition metal carbides and nitrides, Eds, p. 1
2. Oyama ST (1992) Catalysis Today 15 :179
3. Gomes S, David L et al. (2008) Eur Phys J Special Topics 153:87
4. Juenke EF (1964) Report GEMP-267
5. Dollé M, Gosset D, Bogicevic C et al. (2007) J Eur Cer Soc 27:2061

6. Sacks MD, Wang CA et al. (2004) J Mater Sci 39:6057
7. http://www.gen-4.org/
8. Corriu RJP (2000) Angew Chem Int Ed 39:1376
9. Martin HP, Müller E, Knoll Y, Strienitz R, Schuster G (1995) J Mater Sci Lett 14:620
10. Martin H-P, Ecke R, Müller E (1998) J Eur Cer Soc 18:1737
11. Wei GC, Kennedy CR, Harris LA (1984) Ceram Bull 63-8:1054
12. Julbe A, Larbot A, Guizard C, Cot L, Charpin J, Bergez P (1990) Mat Res Bull 25:601
13. Kevorkijan VM, Komac M, Kolar D (1992) J Mat Sci 27:2705
14. Guo G-Y, ChenY (2006) Appl Phys A 84:431
15. Wei GC (1983) J Am Cer Soc 66-7:C111

Progr Colloid Polym Sci (2010) 137:53–59
DOI: 10.1007/978-3-642-13461-6_11

Poly(*n*-butylcyanoacrylate) Submicron Particles Loaded with Ciprofloxacin for Potential Treatment of Bacterial Infections

Georgi Yordanov[1], Nikola Abrashev[2], and Ceco Dushkin[1]

Abstract Poly(*n*-butylcyanoacrylate) submicron colloidal particles loaded with the antibiotic ciprofloxacin are prepared by emulsion polymerization and characterized by scanning electron microscopy, dynamic light scattering, nuclear magnetic resonance and gel-permeation chromatography. The entrapment efficiency for ciprofloxacin in the polymer particles is investigated as a function of the monomer and drug concentrations in the polymerization medium. The kinetics of ciprofloxacin release from the polymer particles is found to depend on the pH of the release medium. Studies by gel-permeation chromatography indicate for a possible drug-polymer association. The antibacterial activity of the obtained formulation is tested on a clinical isolate of *Escherichia coli* bacterium and is found to be similar to that of the free drug.

Keywords poly(*n*-butylcyanoacrylate) • colloids • submicron particles • ciprofloxacin • drug release • *Escherichia coli*

Introduction

The development of various methods for targeted delivery of antibiotics to infected cells and foci of bacterial infection represents a hot topic in drug delivery research. The use of colloidal submicron particles as drug carriers [1-4] is an alternative approach to the classical antibacterial therapy. It consists of association of the drug to a submicron particle carrier, thereby hiding and protecting the antibiotic molecule from degradation, and its delivery to inaccessible target cells in a controlled manner, which may be beneficial for the treatment of intracellular infections [5, 6]. In this regard, poly (alkylcyanoacrylate) (PACA) submicron particles meet ideally the requirements for antibiotic-carrier systems due to a number of advantageous properties such as biocompatibility, biodegradability, and low toxicity [7-15]. The entrapment of antibiotics in PACA submicron particles has been found to increase significantly the drug therapeutic efficiency against intracellular pathogens [8-10].

On the other hand, ciprofloxacin (CIP) is a fluoroquinolone antibiotic with a broad activity against a variety of clinically relevant microorganisms. It is used for the treatment of urinary tract infections, gastrointestinal infections, sexually transmitted infections, as well as infections of the skin and bones [16]. Promising formulations have been previously prepared by the association of CIP with human-serum-albumin colloidal particles [17], poly(D,L-lactide-*co*-glycolide) submicron particles [18-20], as well as submicron particles of poly(isobutylcyanoacrylate) (PIBCA) [21-23] and poly(ethylbutylcyanoacrylate) (PEBCA) [24].

Here we report on the preparation, physicochemical characterization and the antibacterial activity of ciprofloxacin-loaded poly(*n*-butylcyanoacrylate) (PBCA) submicron particles intended for the treatment of bacterial infections. We demonstrate the successful entrapment of CIP in PBCA submicron particles by emulsion polymerization using the surfactant PEG-PEO-PEG amphiphilic triblock copolymer (Pluronic F68). Previous studies on the entrapment of CIP in PIBCA particles are based on dispersion polymerization using the colloidal stabilizer dextran 70 [21,22]. The dispersion polymerization of alkylcyanoacrylates proceeds in a different way than the emulsion polymerization (see the discussion section). On the other hand, the previously reported studies on the entrapment of CIP in PEBCA submicron particles have found it being possible only in the presence of acetone (30 %, v/v) in the polymerization medium [24]. These results indicate that small changes in the formulation may lead to a

G. Yordanov (✉)
[1]Laboratory of Nanoparticle Science and Technology, Department of General and Inorganic Chemistry, Faculty of Chemistry, Sofia University 'St. Kliment Ohridski', 1 "James Bourchier" Blvd., 1164, Sofia, Bulgaria
e-mail: chem_gbg@yahoo.com
[2]Microbiological Laboratory, Multiprofile Hospital for Active Treatment 'Dr. Nikola Vasiliev', 1 "17-th January" Sqr., 2500 Kyustendil, Bulgaria

© Springer-Verlag Berlin Heidelberg 2010

different behavior, depending on the type of monomer used. The synthesis of CIP-loaded PBCA submicron particles reported here is acetone-free, which is more advantageous for potential pharmaceutical applications; nevertheless the *n*-butylcyanoacrylate monomer is approved for human use as surgical glue [25]. We characterize the obtained formulation by scanning electron microscopy, dynamic light scattering, nuclear magnetic resonance, and gel-permeation chromatography. The effects of monomer and drug concentrations in the polymerization medium on the entrapment efficiency for CIP are investigated. The effect of pH on the drug release kinetics and particle erosion is studied. Antibacterial susceptibility tests of the obtained formulation against a clinical isolate of *Escherichia coli* bacterium are performed. It is found that the entrapped drug is of nearly the same efficiency as the free one, which opens the way of its application bearing in mind the other advantages of polymer submicron particles.

Experimental Procedures

Materials and reagents. The *n*-butylcyanoacrylate (BCA) monomer was from Special Polymers Ltd (Bulgaria). Ciprofloxacin (CIP) lactate was from KRKA (Slovenia). Phosphate-buffered saline (PBS; various pH values were adjusted by 1 M HCl), citric acid (anhydrous), sodium hydroxide (puriss. p.a., >99 %), hydrochloric acid (37 %), and Pluronic F68 were from Sigma. Glucose (10 %, w/w) was from Actavis (Bulgaria).

Preparation of ciprofloxacin-loaded submicron particles. The polymerization medium was prepared by dissolving Pluronic F68 (20 mg) and citric acid (20 mg) in glucose solution (5 ml 10 %, w/w); then ciprofloxacin (1-3 mg/ml) was added and diluted with distilled water to 10 ml. The *n*-butylcyanoacrylate monomer (50-200 μl) was added dropwise to the polymerization medium upon vigorous stirring (∼600 rpm rotation speed). After polymerization (for 3 hours), the pH of the obtained colloidal dispersion was adjusted at 5.6 by the addition of 1 M NaOH (0.2 ml). Pure PBCA particles were prepared as a reference at similar conditions but without addition of CIP. The amount of particles in the as-obtained dispersion was determined by centrifugation (14500 rpm, 30 min) of an aliquot (1 ml) from the dispersion in a pre-weighted Eppendorf tube, followed by washing with distilled water and vacuum drying. The as-obtained drug-loaded particles can be stored at 4°C for at least one month without any observable changes.

Characterization of the submicron particles. The as-obtained submicron particles were imaged by a scanning electron microscope (SEM) JSM-5510 (JEOL). Dynamic light scattering (DLS) system Malvern 4700C (Malvern Instruments, UK) was used to measure the particle size and size distribution (each value was obtained as average of five measurements). Nuclear magnetic resonance (^{1}H-NMR) spectra were taken in acetone-d6 with Bruker Avance II+ 600 spectrometer (spectrometer frequency 600.13 MHz). The molecular weight of polymer was determined by gel-permeation chromatography (GPC) using a GPC system with refractive index (RI Waters M410) and ultra-violet (UV Waters M484) detectors, operating at a wavelength of 254 nm. Styragel columns with nominal pore sizes of 100 and 500 Å were utilized. Tetrahydrofuran (THF) was used as the eluent, with a flow rate of 1 ml/min, at 45°C. The samples were prepared as solutions in THF (3.5 mg/ml). The calibration was carried out with poly(ethylene glycol) (PEG) standards. The CIP-PBCA particles used for the NMR and GPC analyses were purified from the unloaded drug by centrifugation, washed twice with distilled water, and dried under vacuum.

Drug entrapment efficiency. The amount of CIP entrapped in PBCA particles was determined by centrifugation of the as-prepared colloid dispersions (14500 rpm, 20 min) and spectrophotometrical determination of CIP in the supernatant. The measurements are made in 0.01 M PBS (pH 7.4) by a double-beam UV-vis spectrophotometer Evolution 300 (Thermo Scientific) at 334 nm. The entrapment efficiency is defined as the fraction of drug entrapped in the polymer particles with respect to its total amount.

Drug release kinetics and particle erosion. An aliquot (1 ml) of the as-prepared particle dispersions was centrifuged (14500 rpm, 10 min) to remove the non-entrapped drug; the particles were washed with 0.2 % (w/v) aqueous solution of Pluronic F68 (1 ml) and re-dispersed in PBS (1 ml) by ultrasound sonication for 3 min. After that the particles were transferred into 49 ml of the release medium (0.01 M PBS, pH 4.6, 5.6, 6.5 or 7.4). The release buffer contained also 0.2 % (w/v) Pluronic F68 in order to avoid any particle aggregation during the release experiments. The experiments were carried out at 37°C in a closed vessel (to prevent evaporation of the release medium) upon magnetic stirring (300 rpm). The amount of released drug was determined by taking aliquots from the release medium, removing the dispersed particles by centrifugation, and spectrophotometrical measurement of the drug concentration in the obtained supernatant. The particle erosion was evaluated by spectrophotometric measurements of the optical density at 400 nm as previously described [24] (actually, the light scattering by the particles in the dispersion causes a reduction in the light transmission).

Antibacterial susceptibility tests. The antibacterial activities of free ciprofloxacin, CIP-PBCA particles and pure PBCA particles were compared by a dilution susceptibility test in Mueller-Hinton broth (Merck, Germany) on a ciprofloxacin-susceptible strain of *Escherichia coli*. The strain was

a clinical isolate obtained from infected wound, identified and biochemically characterized as indole (+), citrate (−), urease (−), lysine decarboxylase (+) and ornithine decarboxylase (+). The activity of the CIP-PBCA formulation was compared with that of a CIP solution with the same drug concentration. The minimal inhibitory concentration (MIC) was defined as the lowest antibiotic concentration inhibiting bacterial growth (determined by measuring the optical density) after incubation for 18 h at 37°C.

Results and Discussion

The PBCA colloidal particles can be prepared by two different procedures: (i) emulsion polymerization, and (ii) dispersion polymerization. The emulsion polymerization of alkylcyanoacrylates proceeds in a different way in comparison with the classical emulsion polymerization [26-28]. It consists of the dropwise addition of monomer to acidic aqueous solution of a suitable surfactant (such as Pluronic F68). At these conditions the micelles take up monomers resulting in swollen micelles. The hydroxide anions initiate polymerization into the swollen micelles via anionic mechanism. The further growth of particles is a result of monomer transfer from the larger droplets to the initially formed primary particles. During this process, drug molecules can be entrapped between the polymer chains. Furthermore, various non-covalent interactions (such as hydrogen bonds, electrostatic attraction, etc.) may increase the drug association with the polymer. For example, it is well known that PACA colloidal particles adsorb on their surface various cationic drugs [21,23,29].

The difference in the case of dispersion polymerization is that colloidal stabilizers (such as dextrans) are used instead of surfactants. At these conditions, the hydroxide anions initiate the reaction to form PACA oligomers resulting in the formation of the primary polymer particles by precipitation. These initial particles add further monomers and oligomers thus growing in size. The colloidal stabilizer prevents the particle aggregation. Dextran 70 has been previously used as a stabilizer for the preparation of CIP-loaded PEBCA colloids, but the drug entrapment is possible only in the presence of acetone in this case [24]. Our preliminary tests on the preparation of CIP-PBCA particles by dispersion polymerization showed that the utilization of dextran results in relatively unstable colloids, which coagulate soon after their preparation. In contrast, the emulsion polymerization in the presence of Pluronic F68 results in the formation of stable CIP-PBCA colloids, whose characteristics are described below.

The SEM shows that the as-obtained CIP-PBCA particles are spherical in shape of an average size of about 240 nm (Fig. 1a). It is interesting that the pure PBCA particles prepared at similar conditions are much smaller – about 170 nm in diameter (Fig. 1b). The procedure for sample

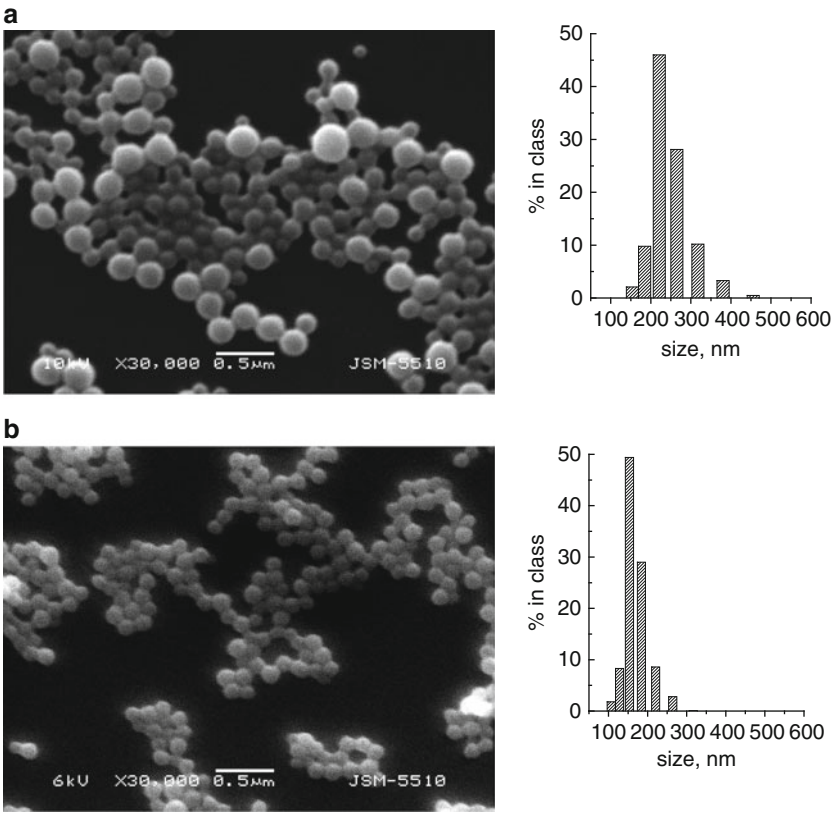

Fig. 1 Representative SEM images (*left*) and the respective size-distributions obtained by DLS (*right*) of CIP-PBCA particles (a) and pure PBCA particles (b). The particles are prepared with *n*-butylcyanoacrylate concentration 10 mg/ml. The CIP concentration is 3 mg/ml in the case of CIP-PBCA particles.

preparation (centrifugation, washing twice with distilled water and drying on a glass substrate under vacuum) results in a partial aggregation of the particles on the glass substrate. However, the DLS analyses demonstrate that there are no particle aggregates in the as-obtained colloidal dispersions. The particle size distribution is monomodal as confirmed by both SEM and DLS.

The reason for different sizes of CIP-PBCA and pure PBCA particles is unclear. May be it is a result of the different molecular weight of polymer (see below), and/or more complex effect of CIP on the emulsion polymerization process. It is important to note that not the entire amount of initial monomer is transformed into PBCA particles. For example, the particle content in the dispersion of pure PBCA (prepared with initial monomer concentration 10 mg/ml) is only 6.9 mg/ml, which means that about 30 % of the initial monomer is not included in the obtained particles. Similarly, the particle content in the respective dispersion of CIP-PBCA is 6.3 mg/ml (the values of particle content are usually scattered with ±10 %). The monomer that is not included into polymer particles may form oligomers with lower molecular weight, which are probably solubilized in the polymerization medium containing the surfactant. Also, a small part of polymer (usually below 5-10 % of the initial monomer) is found deposited on the Teflon-coated stirring bar after the particle preparation.

The successful entrapment of CIP in PBCA particles is confirmed by ^{1}H-NMR spectroscopy. The signals for methylene protons appear in the spectrum of pure PBCA at 1.5 ppm (2H), 1.7 ppm (2H), 2.9 ppm (2H) and 4.3 ppm (2H). The signal at 1.0 ppm (3H) is from methyl protons. Signals from the entrapped CIP molecules appear at 8.74 ppm (1H, s), 7.94 ppm (1H, d, $J = 13.27$ Hz) and 7.72 ppm (1H, d, $J = 7.30$ Hz).

Since the drug is water-soluble and is used below its solubility, a question arises about the mechanism of its loading in the relatively hydrophobic PBCA particles. There are few possible forms of drug association with the polymer. First, the drug may form electrostatic interactions with the surface of the polymer particles. Previous studies demonstrated that CIP could be adsorbed on PEBCA colloids resulting in remarkable reduction of the zeta potential [24]. Similarly, other water-soluble drugs (such as doxorubicin, methotrexate, dactinomycin, etc.) could be adsorbed on the surface of PACA particles [23,29]. Second, CIP could be entrapped in the polymer matrix of the particles in its free base form (neutral molecule), which is less polar than the ionic forms. Indeed, on the basis of ^{19}F-NMR analysis, the CIP loaded in PEBCA has been previously found only in its free base form [24]. Finally, some CIP molecules could be modified by the addition of alkylcyanoacrylate monomers (see below), which may result in increased affinity toward the polymer material.

The polymerization of alkylcyanoacrylates in aqueous media usually proceeds via anionic mechanism (the reaction is initiated by OH^-) [26-28]. Previous investigations indicated that the CIP molecules could initiate zwitterionic polymerization of alkylcyanoacrylates via the amino-group, thus becoming covalently bonded to the polymer backbone [24]. Since the nitrogen from the piperazine amino-group can provide an electron pair, a nucleophilic attack occurs leading to the formation of a covalent bond between the CIP molecule and the *n*-BCA monomer, followed then by the polymerization. We assume that a similar process may take place during the CIP entrapment in PBCA particles, reported here. It is difficult to use the data from ^{1}H-NMR in order to confirm a possible association/interaction between CIP molecules and the polymer. Therefore, we use gel permeation chromatography (GPC) with a dual simultaneous detection (UV and RI) to obtain information about two important characteristics of the CIP-PBCA colloids: the molecular weight of PBCA polymer; and indication of association/interaction between the polymer and the CIP molecules.

The molecular weights obtained in our experiments are typical for PBCA colloids prepared by emulsion polymerization

Table 1 Results from the GPC analysis of polymer from CIP-PBCA and pure PBCA particles. The particles are prepared using c(BCA)=10 mg/ml and c(CIP)=2 mg/ml

Particles	Detection	Max RT, min	Mp	Mw	Mz	Mn	PD
CIP-PBCA	UV-254	22.94	1521	1502	1519	1485	1.01
	RI	23.72	838	862	903	818	1.05
PBCA	UV-254	22.95	1514	1688	2431	1436	1.31
	RI	22.95	1272	2205	2890	1667	1.32

RT – retention time; Mw = weight-average molecular weight; Mn = number-average molecular weight; Mz = Z-average molecular weight; Mp = peak molecular weight; PD=Mw/Mn

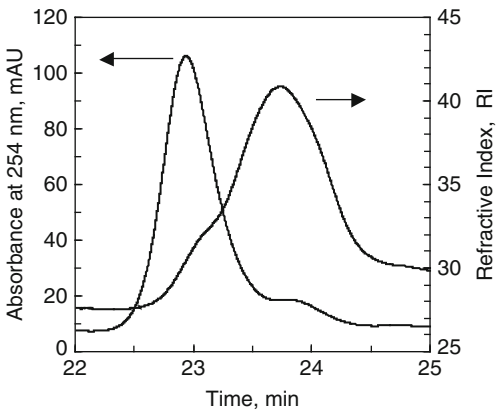

Fig. 2 GPC chromatograms of CIP-loaded PBCA particles dissolved in THF. The chromatograms are recorded with double (UV and RI) simultaneous detection.

[30-34] (Table 1). The GPC chromatograms of CIP-PBCA particles dissolved in THF are shown in Fig. 2. As seen, there are two fractions of oligomeric molecules in the case of CIP-PBCA: (i) a "heavier" fraction, with Mw ~1500, which shows intensive UV-absorption at 254 nm; and (ii) a "lighter" fraction, with Mw ~860, which shows very low UV-absorption. The refractive index (RI) detection indicates that fraction (ii) is the predominant one. The PBCA polymer is not expected to show a significant light absorbance at 254 nm due to the lack of a chromophore group. However, the CIP molecule contains an aromatic ring, which is a UV-chromophore. We suppose that the stronger UV-absorption of fraction (i) corresponds to PBCA associated with CIP molecules, while fraction (ii) contains pure PBCA oligomers. The GPC analysis of pure PBCA, carried out at similar conditions, indicates the formation of longer oligomeric chains (14-mers) with Mw ~2200 (measured by using RI-detector). The higher molecular weight in the case of pure PBCA could be a result of the slightly lower pH (2.52) of the polymerization medium (the polymerization medium, which contains CIP has a pH = 2.86). This is expected to result in the initiation of smaller number of growing polymeric chains (the initiator is OH^-, whose concentration is lower in more acidic pH). Interestingly, the polydispersity index (PD) of the obtained polymer in the case of CIP-PBCA is smaller (1.05) than in the case of pure polymer (1.32). It means that the molecular weight distribution of the polymer in the case of CIP-PBCA is appreciably narrower than that of pure PBCA. Similar difference in the PD-values has been previously observed in the case of CIP-loaded poly(ethylbutylcyanoacrylate) colloids [24].

The effect of initial concentration of CIP in the polymerization medium on the drug entrapment efficiency is shown in Fig. 3a. In these experiments, the concentration of *n*-BCA is kept constant at 10 mg/ml. As seen, higher entrapment efficiency is achieved at lower CIP concentrations (~1 mg/ml). At higher CIP concentrations the entrapment efficiency decreases. The initial *n*-BCA concentration in the polymerization medium (at a constant CIP concentration 2 mg/ml) has a different effect on the drug entrapment in particles, as seen from Fig 3b. Increasing the monomer concentration increases the drug entrapment efficiency. Interestingly, we observed variations in the entrapment efficiency (about ±10 %) depending on the batch of *n*-BCA used. In order to avoid confusion from such batch-to-batch variations, *n*-BCA from the same batch is used for evaluation of the effects shown in Fig. 3. As an optimal formulation we find the CIP-PBCA colloidal particles, prepared at CIP and *n*-BCA concentrations 3 mg/ml and 10 mg/ml, respectively. These particles are used for further studies of the drug release kinetics and antimicrobial activity.

Since submicron particles could target intracellular lysosomal compartments (following phagocytosis by macrophages) [5,6,8-10], it is important to investigate the drug release kinetics at various pH (the pH of blood is about 7.4, but inside lysosomes it is about 4.6). Since, the CIP molecule contains both amino (NH) and carboxylic (COOH) groups, it is a typical zwitterionic drug, which exists in aqueous solutions of CIP in different forms depending on the pH. The pKa values for the COOH and NH_2^+ groups are 5.86 (pKa_1) and 8.24 (pKa_2), respectively [35,36]. By using these values one can calculate the distribution of the different CIP forms (cationic, neutral and anionic) at given pH. At pH < 5 more than 90 % of CIP exists as a cation. At physiological pH (7.4) CIP is in its neutral form (zwitterion and molecule). Calibration curves for spectrophotometric determination of CIP concentration at different pH are built (the UV-vis absorbance spectrum of CIP depends on the pH of solution). Parallel to the drug release experiments, controls of pure PBCA particles dispersed in the release medium for a different time are performed for a baseline reference in the measurements of CIP concentration. The drug release profiles from PBCA nanoparticles at various pH of the release medium are shown in Fig. 4a. The highest release rate is observed at pH 7.4. The release rate is lowest at pH = 5.6. At the same time, the particle erosion is followed indirectly by measurements of the optical density

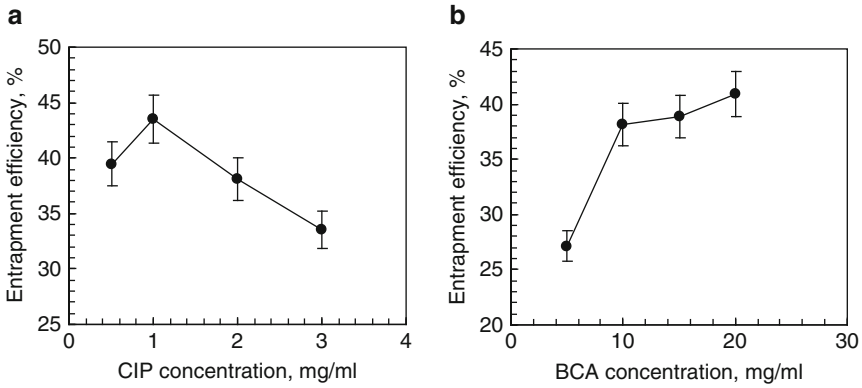

Fig. 3 Drug entrapment efficiency as a functions of (a) CIP concentration (at constant *n*-BCA concentration 10 mg/ml), and (b) *n*-BCA concentration (at constant CIP concentration 2 mg/ml). All experiments are made using *n*-BCA from the same batch.

of the dispersion at 400 nm, which method has been used previously for a similar purpose [24,37-39] (Fig. 4b).

The particle erosion is probably a result of hydrolysis of the ester bonds in the PBCA polymer, as previously shown [37-39]. As seen from Fig. 4, the particle erosion at pH = 5.6 is very slow, which corresponds to a slow drug release. At a lower pH (4.6), the erosion process becomes faster, probably as a result of acid-catalyzed hydrolysis of the polymer. Similarly, a higher pH also leads to increased erosion rate, probably as a result of base-catalyzed hydrolysis. As seen, the increased particle erosion leads to a higher drug release rate. Previous investigations also have confirmed that the particle erosion could enhance the release of entrapped drug molecules [24,29]. It is interesting to note that the release of CIP is not complete - about 30 % of the entrapped CIP could not be released from the polymeric network at all. Similar results have been previously observed for CIP-loaded poly (ethylbutylcyanoacrylate) nanoparticles [24] and are usually explained by a strong interaction/association of the drug molecules with the polymer. Interestingly, the pure PBCA particles are much more stable against erosion at similar conditions (data not shown here). The erosion of pure PBCA becomes significant after 10 hours of stirring in PBS at 37°C and pH=7.4 being insignificant at the other investigated conditions. This could be explained by the relatively higher molecular weight of polymer in the case of pure PBCA in comparison with CIP-PBCA (Table 1). The longer PBCA chains probably hydrolyze much slower leading to a higher stability of the corresponding particles.

The antibacterial activities of "free" CIP, CIP-PBCA (particle formulation) and pure PBCA particles are tested using *in vitro* dilution test against a clinically isolated strain of *Escherichia coli*. The CIP-PBCA particles are tested after their preparation, without removing of the unloaded drug. This particle formulation actually contains unloaded drug and CIP-PBCA particles. The treatment of infections in future *in vivo* experiments is expected to be more effective if both the "free" drug and drug-loaded particles are used in a combination. The amounts of "free" CIP and CIP-particle formulation are adjusted to various equivalent concentrations of the drug in the range of 0.001 to 3.0 μg/ml. Figure 5 shows the *in vitro* antibacterial activity of the "free" CIP and the particle formulation against *Escherichia coli*. The relative bacterial growth was evaluated by measuring of turbidity using optical densimeter and expressed in McFarland units (1 McFarland = 3.0×10^8 CFU/ml). The pure PBCA particles have no detectable effect on the bacterial growth at the investigated concentrations (up to 10 μg/ml). The minimal inhibitory concentrations (MICs) of both formulations of CIP, "free" and particle-formulated, are ~0.011 μg/ml. This is a very important result, indicating that the presence of PBCA polymer does not decrease the antibiotic activity of CIP. Similarly, previously performed *in vitro* studies on the antibacterial activity of CIP-loaded poly(D,L-lactide-*co*-glycolide) submicron particles [20] and CIP-loaded PEBCA colloids [24] have shown a similar activity of the "free" drug and the respective particle-based formulations.

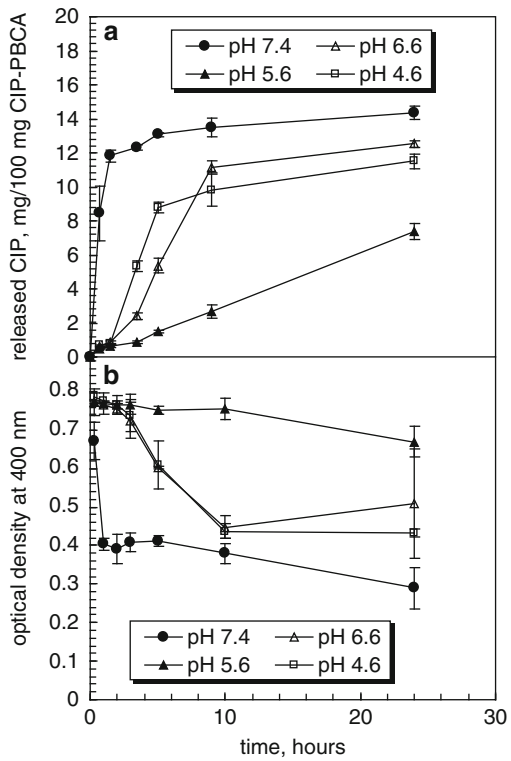

Fig. 4 (a) Release kinetics of CIP from CIP-PBCA nanoparticles at 37 °C in phosphate-buffered saline at different pH (given in the legend); (b) Temporal changes in the optical density of the dispersions of CIP-PBCA particles during the same experiments. The initial CIP-PBCA particles are of an average size of 240 nm and a concentration in the release medium of 0.12 mg/ml.

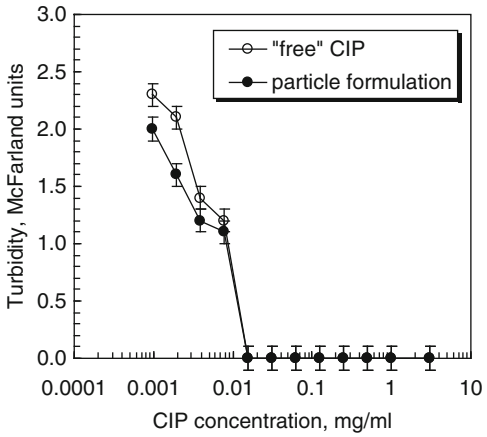

Fig. 5 Antibacterial activity of the "free" CIP and the particle formulation, containing CIP-PBCA submicron particles. The turbidity of growth medium (which is proportional to the bacterial number) is plotted as a function of CIP concentration. No bacterial growth is observed at CIP concentrations above 0.011 μg/ml in both cases.

Conclusions

We prepare pure and ciprofloxacin-loaded PBCA submicron spherical particles by acetone-free emulsion polymerization. The pure PBCA particles are much smaller (∼170 nm) than those loaded with ciprofloxacin (∼240 nm). The ^{1}H-NMR analysis confirms the successful drug entrapment. The drug entrapment efficiency is determined as a function of the drug and monomer concentrations in the polymerization medium and can be as high as 45 %. The GPC analyses shows that the obtained CIP-PBCA particle formulation contains two fractions of molecules with molecular weights Mw∼1500 and ∼860 Da, respectively. It is suggested that the heavier polymer fraction contains bound CIP molecules. In comparison, the molecular weight of polymer in the case of pure PBCA particles is ∼2200 Da. The partial association of CIP with PBCA is confirmed also by the results from drug release studies, which reveal that only ∼70 % of the entrapped CIP is releasable. Furthermore, the drug release rate and particle stability are found to depend strongly on the pH of the release medium. The releasable CIP loaded in PBCA particles is supposed to be in its free base form (neutral molecule), which is less polar than the ionic forms as confirmed in previous studies [24]. The antibacterial susceptibility tests show that the CIP-PBCA formulation are at least as active as the free drug, which indicates that the antibiotic is not deactivated by the polymer. This fact implies that the obtained formulation has a remarkable potential for application in the treatment of bacterial infections.

Acknowledgements G.Y. and C.D. are thankful to COST Action D43 of the European Community.

References

1. Salata OV (2004) J Nanobiotechnology 2: 3.
2. Barratt G (2003) Cell Mol Life Sci 60: 21-37.
3. Brannon-Peppas L, Blanchette JO (2004) Adv Drug Deliver Rev 56: 1649-1659.
4. Briones E, Colino CI, Lanao J (2008) J Controlled Release 125: 210-227.
5. Gulyaev A, Ermekbaeva B, Kivman G, Radchenko T, Sherstov A, Shirinskii V (1998) Pharm Chem J 32: 3.
6. Pinto-Alphandary H, Andremont A, Couvreur P (2000) Int J Antimicrob Ag 13: 155-168.
7. Vauthier C, Dubernet C, Fattal E, Pinto-Alphandary H, Couvreur P (2003) Adv Drug Deliver Rev 55: 519–548.
8. Fattal E, Youssef M, Couvreur P, Andremont A (1989) Antimicrob Agents Chemotherapy 33: 1540-1543.
9. Balland O, Pinto-Alphandary H, Pecquet S, Andremont A, Couvreur P (1994) J Antimicrob Chemother 33: 509–522.
10. Kisich K, Gelperina S, Higgins M, Wilson S, Shipulo E, Oganesyan E, Heifets L (2007) Int J Pharm 345: 154–162.
11. Zhang Q, Liao G, Wei D, Nagai T (1998) Int J Pharm 164: 21–27.
12. Alonso M, Losa C, Calvo P, Vila-Jato J (1991) Int J Pharm 68: 69-76.
13. Gonzalez-Martin G, Figueroa C, Merino I, Osuna A (2000) Eur J Pharm Biopharm 49: 137-142.
14. Fontana G, Licciardi M, Mansueto S, Schillaci D, Giammona G (2001) Biomaterials 22: 2857-2865.
15. Cavallaro G, Fresta M, Giammona G, Puglisi G, Villari A (1994) Int J Pharm 111: 31-41.
16. Appelbaum P, Hunter P (2000) Int J Antimicrob Ag 16: 5–15.
17. Kumar PV, Jain1 NK (2007) AAPS PharmSciTech 8(1): E1-E6.
18. Dillen K, Vandervoort J, Van den Mooter G, Verheyden L, Ludwig A (2004) Int J Pharm 275: 171–187.
19. Dillen K, Vandervoort J, Van den Mooter G, Verheyden L, Ludwig A (2006) Int J Pharm 314: 72–82.
20. Jeong YI, Na HS, Seo DH, Kim DG, Lee HC, Jang MK, Na SK, Roh SH, Kim SI, Nah JW (2008) Int J Pharm 352: 317–323.
21. Fawaz F, Guyot M, Lagueny A, Devissaguet J (1997) Int J Parm 154: 191-203.
22. Fawaz F, Bonini F, Maugein J, Lagueny A (1998) Int J Pharm 168: 255–259.
23. Page-Clisson M, Gibaud S, Pinto-Alphandary H, Weingarten C, Couvreur P (1998) Int J Pharm 166: 117–120.
24. Page-Clisson M, Pinto-Alphandary H, Ourevitch M, Andremont A, Couvreur P (1998) J Control Release 56: 23–32.
25. Oowaki H, Matsuda S, Sakai N, Ohta T, Iwata H, Sadato A, Taki W, Hashimoto N, Ikada Y (2000) Biomaterials 21: 1039–1046.
26. Donnelly E, Johnston D, Pepper D, Dunn D (1977) J Polym Sci Polym Lett Ed 15: 399–405.
27. Behan N, Birkinshaw C (2000) Macromol Rapid Commun 21: 884–886.
28. Behan N, Birkinshaw C, Clarke N (2001) Biomaterials 22: 1335–1344.
29. Couvreur P, Kante B, Roland M, Speiser P (1979) J Pharm Sci 68: 1521-1524.
30. Vansnick L, Couvreur P, Christiaensleyh D, Roland M (1985) Pharm Res 1: 36–41.
31. El-Egakey M, Bentele V, Kreuter J (1983) Int J Pharm 13: 349–352.
32. Lescure F, Zimmer C, Roy D, Couvreur P (1992) J Colloid Interface Sci 154: 77–86.
33. Douglas S, Davis S, Holding S (1985) Br Polym J 17: 339–342.
34. Alonso M, Sanchez A, Torres D, Seijo B (1990) J Microencapsul 7: 517–526.
35. Barron D, Jimenez-Lozano E, Irles A, Barbosa J (2000) J Chromatography A 871: 381–389.
36. Barbosa J, Barron D, Jimenez-Lozano E, Sanz-Nebot V (2001) Anal Chim Acta 437: 309–321.
37. Vezin W, Florence A (1980) J Biomed Mater Res 14: 93-106.
38. Lenaerts V, Couvreur P, Christiaens-Leyh D, Joiris E, Roland M, Rollman B, Speiser P (1984) Biomaterials 5: 65-68.
39. Muller R, Lherm C, Herbort J, Couvreur P (1990) Biomaterials 11: 590-595.

Index